LEHRSTUHL FÜR BIOMEDIZINISCHE PHYSIK
TECHNISCHE UNIVERSITÄT MÜNCHEN

CHARACTERIZATION AND APPLICATION OF HIGH RESOLUTION PHASE-CONTRAST LABORATORY MICRO-CT SETUPS

PIDASSA MALIMDA BIDOLA

DISSERTATION

MARCH 2017

SUPERVISORS:
DR. KLAUS ACHTERHOLD
PROF. DR. FRANZ PFEIFFER

Technische Universität München

TECHNISCHE UNIVERSITÄT MÜNCHEN
Physik Department
Lehrstuhl für Biomedizinische Physik

Characterization and Application of High Resolution Phase-Contrast Laboratory Micro-CT Setups

Pidassa Malimda Bidola

Vollständiger Abdruck der von der Fakultät für Physik der Technischen Universität München zur Erlangung des akademischen Grades eines

Doktors der Naturwissenschaften (Dr. rer. nat.)

genehmigten Dissertation.

Vorsitzender:	Prof. Dr. Martin Zacharias
Prüfer der Dissertation:	1. Prof. Dr. Franz Pfeiffer
	2. Prof. Dr. Jan Wilkens

Die Dissertation wurde am 26.01.2017 bei der Technischen Universität München eingereicht und durch die Fakultät für Physik am 24.02.2017 angenommen.

To my mother.

Abstract

X-ray imaging in laboratories has undergone rapid advances in terms of resolution and imaging techniques. To enable the study of a wide range of specimens prepared in diverse environments, these setups are being designed to achieve superior results both in contrast and resolution. Hence practical knowledge of the performance of the individual components is required to reach their optimal capabilities, and to execute advanced X-ray imaging procedures. This work presents the study of the behaviour of the source and the detector of two advanced X-ray laboratory systems having different designs for several parameters. Based on this, the prerequisites were examined to allow the optimal application of additional imaging procedures other than the conventional X-ray imaging, particularly the single-distance propagation-based X-ray phase-contrast imaging. Ultimately, several investigations were performed to evaluate the experimental conditions for achieving optimal results in practical tomographic applications. Applications of single-distance propagation-based X-ray phase-contrast imaging reported in this thesis will enable laboratory-based commercial systems to provide conclusive results to users.

Zusammenfassung

Röntgenbildgebung in Laboratorien hat rasche Fortschritte in Bezug auf Auflösung und bildgebende Verfahren gemacht. Um das Studium eines breiten Spektrums von Proben zu ermöglichen, die in verschiedenen Umgebungen hergestellt wurden, werden diese Setups entwickelt, um herausragende Ergebnisse sowohl im Kontrast als auch in der Auflösung zu erzielen. Daher ist eine praktische Kenntnis der Leistungsfähigkeit der einzelnen Komponenten erforderlich, um ihre optimalen Fähigkeiten zu erreichen und fortschrittliche Röntgenbildgebungsverfahren durchzuführen. Diese Arbeit stellt die Untersuchung des Verhaltens der Quelle und des Detektors zweier fortgeschrittener Röntgenlaborsysteme verschiedener Designs für mehrere Parameter vor. Daraufhin wurden die Voraussetzungen geprüft, um die optimale Anwendung zusätzlicher bildgebender Verfahren außer der konventionellen Röntgenbildgebung, insbesondere die propagationsbasierte Röntgen-Phasenkontrastbildgebung mit nur einer Propagationslänge, zu ermöglichen. Letztendlich wurden mehrere Untersuchungen durchgeführt, um die experimentellen Bedingungen zur Erzielung optimaler Ergebnisse in praktischen tomographischen Anwendungen zu bewerten. Anwendungen der propagationsbasierten Röntgen-Phasenkontrastbildgebung mit nur einer Propagationslänge, die in dieser Arbeit berichtet werden, versprechen schlüssige Ergebnisse für die Nutzer kommerzieller Laboraufbauten.

Contents

Chapter 1

Introduction

The main motivation of this PhD thesis is approached in the present chapter, addressing the need to study the boundaries of advanced laboratory X-ray micro-computed tomography systems, and to examine the feasibilities of diverse X-ray imaging techniques.

Soon after their discovery [Röntgen, 1895], X-rays aroused a great interest due to their ability to penetrate opaque objects. Originally started in medicine by recording 2D radiographs [Norton, 1896], imaging with X-rays was upgraded much later to three dimensional X-ray tomography and computed tomography (CT) [Craig, 1936, Cormack and Hounsfield, 2011]. This advance was rapidly extended in laboratory facilities to microcomputed tomography (μCT) [Elliott et al., 1981] and was employed in various fields such as exploration of materials [Muller et al., 1994, Rügsegger et al., 1996], thereby creating a variety of users. Hence the advent of laboratory X-ray systems for commercial purposes. These were constantly developed to meet the specific needs required in their respective areas. This work shall cover the study of the performances of commercial laboratory setups by studying their components in detail. Based on the results, several methods for the improvement of contrast and resolution have been investigated. Consequently, we motivate in the following the characterization of two laboratory devices, as well as the application of specific imaging methods that can be routinely used in these devices.

Laboratory X-ray setups are rated according to the quality of images they can provide. In both radiographic and tomographic X-ray imaging in conventional laboratory systems, the reachable resolution throughout imaging is fundamentally influenced by the source and the detector [Zhou et al., 2016, Mertens et al., 2014]. With regards to the source, varying the tube current and voltage is sufficient to modify the dimension, spectrum and intensity of the beam. Combined with the properties of a selected detector, these parameters of the source determine the resolution of images, especially in high-resolution laboratory X-ray imaging facilities. Indeed various setups are being developed on purpose to yield high resolution, and therefore are customarily known as advanced laboratory X-ray systems. However, they can be differentiated in their design, depending on whether the imaging resolution relies on only the geometric magnification of the object's image on the detector or on both the geometric magnification and an additional optical magnification. Optical magnification is made possible by a new type of detector which incorporates a magnifying objective.

With the growing request of users and the variety of samples to explore on laboratory

setups, it is necessary to know the most appropriate settings for a given sample. This is why the characterization of two systems, with and without optical magnification, is needed. For this purpose, we conducted the study of the performances in terms of resolution of two devices: v|tome|x s 240 from General Electric (GE) and ZEISS Xradia 500 Versa by Carl Zeiss (former Xradia Inc.)

Although laboratory systems provide several advantages such as ready accessibility, quick scan times and longitudinal studies, they suffer from lack of contrast for the examination of biological tissues (low-Z materials) or complex composite samples due to the poor absorption contrast of these materials for X-rays. Novel techniques are being explored to extend the capabilities of X-ray imaging in laboratories. The staining of soft tissues prior to their inspection with µCT is an example of how to improve the contrast on biological samples [de Crespigny et al., 2008, Metscher, 2009b]. Also, the dual-energy CT (DECT) is a method to enhance the contrast on dissimilar mediums and has been demonstrated with conventional clinical X-ray imaging systems [Johnson et al., 2007].

The advent of X-ray synchrotron radiation [Willmott, 2011] launched a new imaging era with high brilliance, and qualitative outperformance of conventional laboratory sources. The availability of coherent radiation led to the innovation of new X-ray imaging techniques other than the attenuation-based imaging. Among many other techniques that have been developed at synchrotron facilities, phase-contrast imaging (PCI) has the specificity of providing superior contrast between materials with slightly different densities.

With an increasing popularity of X-ray tomography, laboratory systems are experiencing rapid development, leading nowadays to the transfer of inline or propagation-based phase-contrast imaging [Wilkins et al., 1996], grating-based phase-contrast imaging [Pfeiffer et al., 2006], and even the newly developed speckle-based phase-contrast imaging at setups equipped with bremsstrahlung-based X-ray tubes [Zanette et al., 2014]. So far, the single-distance propagation-based phase-contrast imaging technique has achieved success in some commercially available devices [Eastwood et al., 2014]. Also, interferometric phase-contrast imaging has shown promising results for preclinical studies [Tapfer et al., 2011] in the first industrial prototype by Bruker MicroCT (former SkyScan).

Beyond the understanding of the resolution that can be achieved with advanced laboratory systems, this thesis aims to implement new imaging techniques for contrast enhancement in commercial setups. Therefore, practical applications of these techniques in existing commercial devices is one of the primary goals. Thus, we demonstrated the benefit of combining attenuation-based X-ray imaging with tissue-staining protocols to investigate cancer-diseased lungs with the distant objective of developing new lung cancer therapies. Further, a study of the distribution of lithium in rechargeable batteries through combination of µCT and neutrons diffraction imaging has been shown as an example of the application of these techniques for material science. The energy range available in the source has been used to conduct high resolution dual-energy CT for the quantification of gold content in raw precious stone samples.

After characterization of the devices, the source parameters were found to fullfil all the requirements for single-distance propagation-based phase-contrast imaging (SD PCI). The optimal phase contrast was obtained by choosing appropriate geometric settings for the small source size. Additionally, phase retrieval algorithms were used to increase the contrast. Ultimately, conclusive studies were carried out on representative specimen to validate the pos-

sibility of standardization of the SD PCI and phase retrieval in advanced laboratory X-ray systems.

This thesis is structured as follows. In chapter 2, the fundamentals of attenuation-based X-ray imaging are presented and contrast-enhancement methods based on the principle of this traditional imaging technique are discussed. Key components of laboratory systems and their role in performing X-ray imaging at microscopic scale are illustrated. Chapter 3 is devoted to the theoretical understanding of the interaction of X-ray radiation as electromagnetic waves with matter. A phase shift occurs during this interaction and has given rise to various phase-contrast imaging techniques [Fitzgerald, 2000]. These techniques are briefly reviewed and propagation-based phase-contrast imaging, which is one of the focal points of this thesis, is thoroughly discussed.

Thereafter begins the experimental part of our work with the description and study of the characteristics of the machines in chapters 4 and 5. The functionalities of the system components namely the source and detector are presented and studies demonstrating the feasibility of propagation-based phase-contrast imaging are reported.

Chapters 6 and 7 are devoted to the applications of the investigations performed earlier. Outstanding results from attenuation-based X-ray imaging at medium and high resolution are shown in chapter 6. It should be noted that since two specific commercial devices have been used for all experiments, the observations are benchmarked against these devices. In this context, the application of propagation-based phase contrast, presented in chapter 7, serves as the first demonstration of this technique with ZEISS Xradia 500 Versa. The applications shown in both these chapters can be catalogued in three diverse research areas i.e., entomology, plant physiology and materials science. In conclusion, chapter 8 discusses the contribution of this work to the X-ray imaging especially in advanced laboratory systems and provides some suggestions to consider for improvement or future developments.

Part I

Theoretical background

Chapter 2

Attenuation-based X-ray imaging

This chapter deals with the principles of the conventional X-ray imaging, where the contrast is based on the attenuation of X-rays. The function of each of the components of an imaging system and its contribution to the image quality are presented. First, the system components relevant to this work are presented. Then the principle of X-ray interaction with the matter and the formation of absorption contrast are summarized. Additional interactions other than the absorption are discussed in detail in the following chapter. In the last section of the chapter, the tomographic image reconstruction is discussed.

2.1 X-ray source technologies

2.1.1 Conventional X-ray sources

Conventional X-ray sources, in general, produce a radiation dominated by the "Bremsstrahlung". They work on the principle of electron emission at a cathode, often by thermal excitation, and their acceleration to a fixed anode made of a material with high melting point (ex: molybdenum, tungsten) due to the heat produced throughout the interaction. During this interaction the impinging electrons are mainly deflected in the Coulomb field of the nuclei of the anode atoms, resulting in the so called Bremsstrahlung. In addition to the Bremsstrahlung radiation, the characteristic lines generated from the photoelectric effect due to the inelastic collision of the accelerated electrons with those of the internal orbits of the anode's nuclei complete the spectrum of the X-ray beam. The area of electron interactions with the anode determines the focal spot size of the X-ray tube. According to the diameter of this area, X-ray tubes are attributed a specific name. Microfocus and nanofocus tubes have focal spot sizes smaller than 200 and 1 micrometer (μm), respectively. With the term "conventional" or without any precision, reference is made to tubes with a spot size in a range of hundreds of micrometers to a few millimeters. The physical procedures behind the operation of an X-ray tube is well illustrated in chapter 4 of [Krieger, 2013]. Also, a record of developments in X-ray tubes manufacturing up to now, as well as the operation of each of their components is presented in [Behling, 2015].

2.1.2 Synchrotron radiation sources

The quality of a radiation is primarily judged by the quantity called "brilliance". It is described as the photons intensity released per second in a mm^2 source area, which would diverge within a milli-radian angle. It is defined by considering essentially a range of photon energies (conventionally 0.1 % bandwidth) that contribute to the measured intensity. A well-known non-bremsstrahlung source with high brilliance is the synchrotron. Its radiation comes from the deflection of electrons in insertion devices (IDs) or bending magnets (BDs), when they have been previously accelerated to relativistic speed in a storage ring. Consequently, the flux is several orders higher than that available at laboratory sources. This paragraph is introduced briefly for the reason that some of the results to be presented later are linked to those achieved with synchrotron sources. Nevertheless, Refs. [Behling, 2015, Als-Nielsen and McMorrow, 2011, Willmott, 2011] are suggested for the introduction to some techniques for non-bremsstrahlung X-ray generation.

2.1.3 X-ray sources for microscopy

X-ray tubes provide a divergent cone beam. For X-ray imaging in this geometry, the detectability of features in an object depends on its magnification on a detector placed downstream of the object (see Fig. 2.1). The magnification M is typically defined as the ratio of the source-to-detector (SDD) and source-to-object distances (SOD). At sources with finite dimension such as X-ray tubes, an unsharpness $Ug = S \cdot \frac{\mathrm{ODD}}{\mathrm{SOD}}$, proportional to the source size S, the sample object-to-detector distance (ODD) and inverse proportional to the SOD may occur at the edges of the recorded image on the detector. This is illustrated in Fig. 2.1(b) and (c), with the density distribution in the images (DDI) of a defect, which are shown to sustain severe blurring (unsharpness) as function of the focal spot size.

An image is granted an excellent quality when the unsharpness is minimized, which comes from an ideal small focal spot (Fig. 2.1(a)). Instead of details detectability, the term spatial resolution measurable in length unit is usually mentioned to express the size of the smallest feature that can be comfortably viewed in an image. This relates to the point-spread function (PSF) of the system which represents its performance to resolve any feature in the sample plane. The PSF is identified as a Gaussian with a full-width at half maximum FWHM = $2\sqrt{2\ln 2}\sigma$, where σ is the standard deviation. Thus, the spatial resolution of the cone-beam imaging system can be described by the standard deviation as

$$\sigma_{\mathrm{sys}} = \sqrt{(M-1)^2 M^{-2} {\sigma_{\mathrm{src}}}^2 + M^{-2} {\sigma_{\mathrm{det}}}^2}, \tag{2.1}$$

where the standard deviation of the source σ_{src} and detector σ_{det} are shown to influence, up to a certain amount, the image resolution depending on the magnification. Note that the PSF of the source and detector are regarded as similar to the source size of the focal spot and the detector pixel size, respectively.

With the term microscopy, reference is made to low spatial resolution value, which is achievable at high geometric magnifications (assigned to M in Eq. 2.1) in a conventional divergent geometry. Consequently, Eq. 2.1 would read $\sigma_{\mathrm{sys}} \approx \sigma_{\mathrm{src}}$. In other words, the source size is mostly responsible for the resolution that can be achieved by the imaging system at high magnification. Hence, preferably small spot sizes from few micrometers

down to nanometers (micro- and nanofocus tubes) are required for X-ray microscopy. Two tubes of this kind are discussed in the following: Transmission X-ray tubes and the liquid metal X-ray tubes.

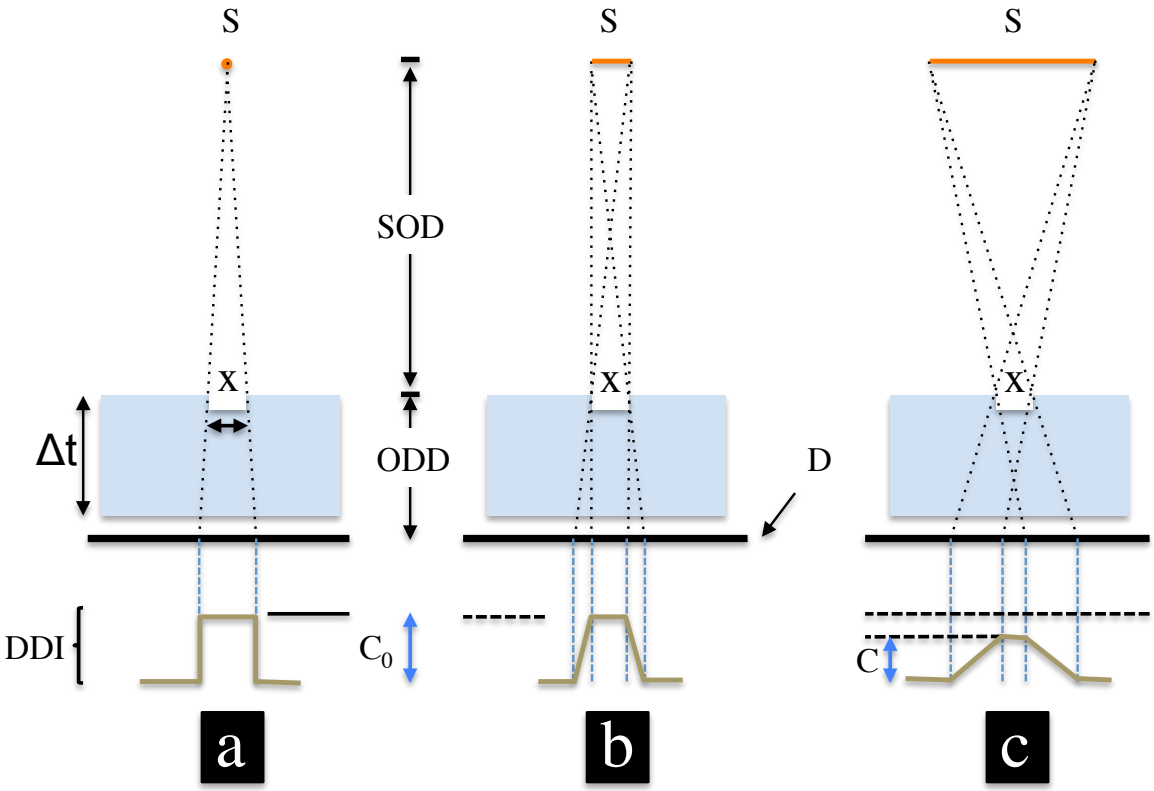

Figure 2.1: Effect of a finite spot size on a small defect of dimension x included in an object. The source S is increased from an ideal point source (a), a medium (b) to a very large source dimension (c). C_0 denotes the original contrast compared to a reduced contrast when the edges of the defect have been blurred due to the unsharpness induced by the large focal spot. The source-to-object and object-to-detector distances are represented by SOD and ODD, respectively. Δt represents the object thickness, D the detector and DDI the density distribution in the image. (Scheme adapted from [Halmshaw, 2012]).

Transmission X-ray tube

Unlike conventional X-ray tubes where the generated photons beam travels in the reflected direction of the impinging bunch of electrons, transmission X-ray tubes are furnished with a flat target of few hundreds of micrometers set perpendicular to the flow of electrons . Once this flow is thoroughly focused on the target, photons are emitted from the relative small focal spot in the forward direction of the impinging electrons. The small source spot achieved at the target determines the effective source size of the X-ray tube, which can drop to hundreds of nanometers. The target film is usually made of tungsten (W) whereas the window is a high permeable material like beryllium (Be), due to its low atomic number Z. For industrial

purposes the thickness of the anode target is in range from ten to several µm [Kutsuzawa, 2002].

To overcome the interfacial exfoliation issue from the thermal expansion of the target film directly attached to the transmission window, Kutsuzawa patented the intervention of an intermediate film of at least one metal element (copper, nickel, iron, etc.) between the window plate and the target film [Kutsuzawa, 2002]. This technology has been sketched in Fig. 2.2. The influence of the thickness of the target layer on the true source size of a transmission tube is demonstrated by X-ray Worx GmbH[1] (Garbsen, Germany). It can be differentiated between open and sealed transmission tubes. The first family enables the exchange of the cathode filament or the target. The second has a permanent vacuum and does not allow the exchange of either the cathode or the anode target. However, X-ray tube manufacturers manage to set some limitations to the power load on the target for a given acceleration voltage, and hence extend the lifespan of the tubes. Besides the advantage

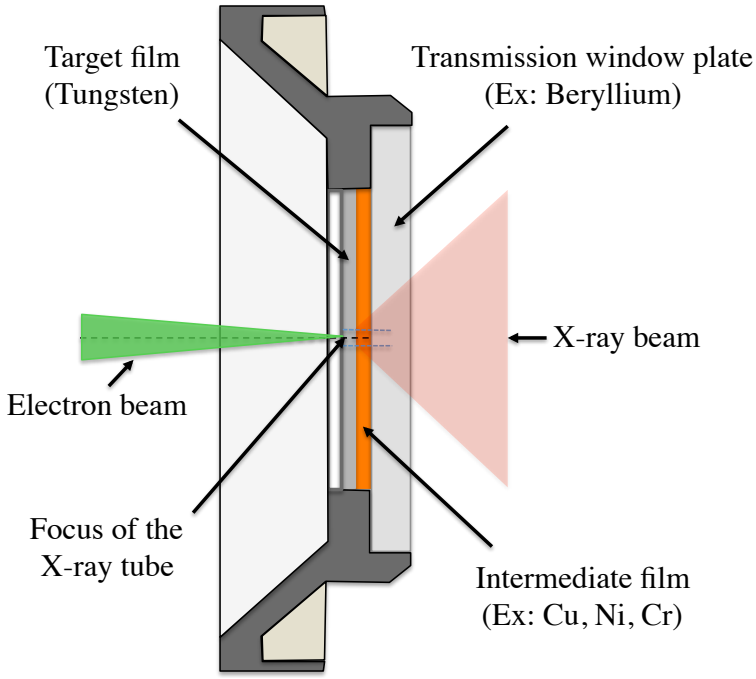

Figure 2.2: Sketch of the window of a transmission X-ray tube. The target film usually made of tungsten and the window plate are separated by an intermediate metal element out of the group of copper, chromium, iron, nickel etc. to prevent interfacial exfoliation. (Scheme adapted from [Kutsuzawa, 2002]).

---

of a small source diameter, the capacity of heat conduction and evacuation at the anode represents a limit to the power that can be applied on the target. This explains the low brilliance attainable at X-ray tubes. An alternative to this drawback is the liquid metal Anode.

[1] http://www.x-ray-worx.com/x-ray-worx/index.php/en/microfocus-x-ray-tubes-overview/microfocus-technology (accessed: 2017-01-18).

2.2 X-ray detection technology

Flat panel detectors These are a type of detectors[2] that belongs to the class of indirect detection detectors, where the X-ray photons are transformed to visible light prior to the conversion into electronic signal. This type of detectors started the era of digitized detection in place of cassettes especially in medical radiography. Due to the large field of view (FOV) and the small spatial resolution they can achieve, they have gained crucial importance in the tomographic imaging of large subjects. In the sequence of conversion of the X-ray photons, they are composed of a converter screen or scintillator screen (e.g., Cesium Iodide (CsI)), directly deposited on a photodiode array and a thin-film transistor to enable efficient coupling. A layer-area of amorphous silicon completes the assembly [Banhart, 2008]. In addition to the large FOV, the excellent conversion capacity have granted flat panel detectors an asset for imaging large objects with fine resolution in medical and other applications.

Lens-coupled detectors As indirect detection system, the incoming X-ray photons are converted via a **converter screen** into visible light that will at the end be converted in electronic signal. In this case, the visible light originated from the scintillator screen is subjected to a **lens coupling** [Koch et al., 1998]. For high spatial resolution imaging, this element plays a determinant role. It can be distinguished between the finite-focused and the infinity-focused systems. The first is made of a fixed tube length, where only the objective determines the resolution of the image. In the infinity-focused system a supplementary lens is introduced and induces a magnification of the systems as a ratio between the objective focal length and the tube lens focal length [Banhart, 2008]. These elements of the detector assembly are crucial for the spatial resolution and are regarded as one of the important characteristics of an imaging system. This might be affected by the processing or shaping of the scintillator and the performance of the objective.

Another characteristic relying on these elements describes their efficiency in the entire process of translating X-ray photons to visible light till the third element of the detector assembly, which is the **charged-coupled device** (CCD). A CCD provides the analogue-to-digital conversion that relates two other important characteristics of a detector: the frame rate and the dynamic range. The frame rate defines the speed of delivery of an image in frames per second (fps) whereas the dynamic range designates the bit depth of the image. With various converter screens, this type of detectors were highly performant for synchrotron application [Stampanoni et al., 2002]. Their design for high resolution imaging, but also the possibility to adapt the scintillator screen for a high yield of visible light make them attractive in imaging with laboratory systems.

2.3 Commercial X-ray systems

X-ray machines manufacturers try to help the client (user) find the answers to the question "what is in your specimen?". This requires to fix specific topics and users that would be addressed while assembling, after extensive planning and testing, a commercial system. The

[2] http://atlas.physics.arizona.edu/%7Ekjohns/downloads/scott/Flat%2520Panel%2520Xray%2520Imaging%252011-11-04.pdf (accessed: 2017-01-18).

components to contribute to the performance of the devices may be accordingly optimized for the targeted purposes. Thus one can refer for example to the range of products and applications granted by Bruker MicroCT[3] (Kontich, Belgium), or Carl Zeiss Microscopy[4] (Pleasanton, CA, USA).The specifications of the devices in this thesis will be discussed in Part II. The present section recalls the motivation of this work which is about exploring what can be done beyond the specifications of a machine made available by a manufacturer.

2.4 Principles of X-ray imaging

2.4.1 X-ray attenuation in matter

Within the effective working energy range of X-ray tubes between 10 keV and a little above 100 keV, the fundamental physical interactions which occur in matter are the photoelectric, Compton (inelastic) and the Rayleigh scattering (elastic). The description of these effects is presented, for example, in Refs. [Hsieh, 2009, Attwood, 2007]. In the following, the X-ray beam will be considered as quantized into photons of energy $E = \hbar\omega$, with $\hbar$ the Planck's constant and ω the radian frequency. Assuming a monochromatic beam of intensity I_0, i.e., comprising of photons of the same energy that pass through a thin medium of uniform density ρ, the outgoing intensity I would be diminished by an exponential term $\exp[-(\mu_{\mathrm{PE}} + \mu_{\mathrm{CE}} + \mu_{\mathrm{R}})\rho\Delta\mathrm{t}]$. The terms μ_{PE}, μ_{CE} and μ_{R} are the mass-dependent attenuation coefficients which accounts for the various interactions aforementioned. This effect is regarded as attenuation of the photon beam within the object due to the attenuation of photons, and known as the Beer-Lambert's law

$$I = I_0 \exp(-\mu\rho\Delta\mathrm{t}), \tag{2.2}$$

where $\Delta\mathrm{t}$ is the thickness of the medium and μ the total mass-dependent attenuation coefficient to be taken as the sum of the effects which occur during the interaction (Photoelectric PE, Compton CE and Rayleigh R). This is related to the atomic density n_a and the global cross-section of the photo-absorption, which can be written as a sum of all the events:

$$\sigma_{\mathrm{tot}} = \sigma_{\mathrm{PE}} + \sigma_{\mathrm{CE}} + \sigma_{\mathrm{R}}. \tag{2.3}$$

The attenuation coefficient $\mu(E, Z)$ depends on the energy and atomic number Z of the material. Therefore, the percentage to which each of these effects contributes to the absorption within a material depends on the Z and on the energy E of the photon beam ([Hsieh, 2009], chapter 1).
The relation between the mass-dependent attenuation coefficient and the complex refractive index of the medium is given by

$$n = 1 - \delta + \mathrm{i}\beta \tag{2.4}$$

Here, δ denotes the decrement and β the absorption term of the complex refractive index. In section 3.2.3, the phase shift of the X-ray beam in matter is presented by considering the photons beam as a plane electromagnetic wave.

[3] http://bruker-microct.com/products/all_products.htm
[4] http://www.zeiss.de/microscopy/de_de/produkte/roentgenmikroskopie.html (accessed: 2017-01-18).

2.4.2 X-ray refraction in matter

With regards to the electromagnetic property of X-rays, the propagation direction of the photon beam follows the pointing or wave vector $\vec{k}$ set perpendicular to both the electric and magnetic fields. Accordingly, X-rays can be reflected at the surface of a medium or refracted in it depending on the approach angle ([Als-Nielsen and McMorrow, 2011, Attwood, 2007, Born and Wolf, 2000], chapter 3). As sketched in Fig. 2.3(a) incident waves from vacuum (n=1) falling with an angle α on the surface of a medium with refractive index n lower than unity are totally reflected if the relation $\alpha > \alpha_c$ fulfils, where α_c is called the *critical angle of incidence*. Otherwise the waves are refracted within the medium and the *Snell's law applies*:

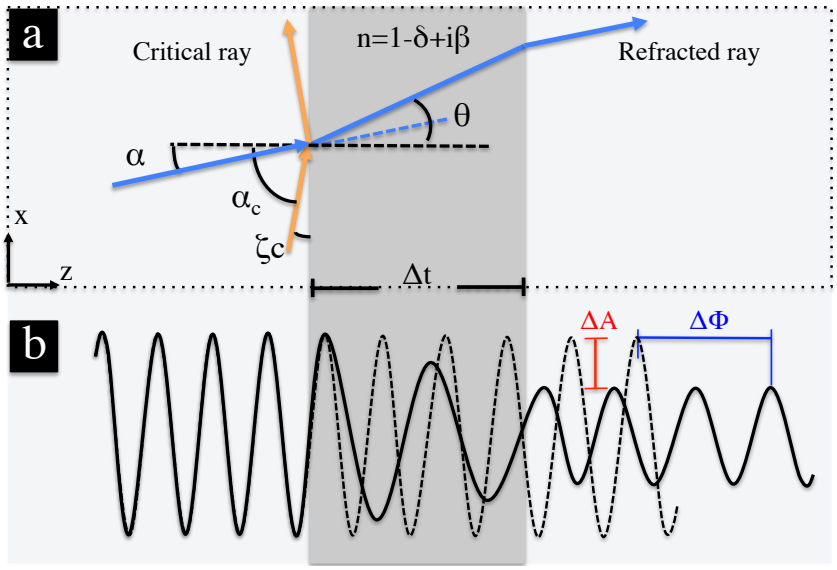

Figure 2.3: Sketch of the X-ray wave interaction with a medium surrounded by air. (a) Scheme of wave vectors indicates the reflection (orange ray) and the refraction (blue ray) that occur according to the impinging angle. (b) Apart from the change in amplitude ΔA between the ideal unperturbed (dashed) ray and the obstructed ray, the phase shift $\Delta\phi$ caused by the refraction in the medium is observable.

$$\sin\theta = \frac{\sin\alpha}{n}, \tag{2.5}$$

which relates α to the refractive angle θ. Assuming low absorption, the term β of n (Eq. 2.4) approaches zero, so that Eq. 2.5 reads

$$\sin\theta = \frac{\sin\alpha}{1-\delta}. \tag{2.6}$$

Thus Eq. 2.6 sets a relation between the complex refractive index of a material and the angle of refraction of an incident wave. It is of interest in the following to show also the relation between the reflection angle and the refractive index. This implies $\alpha > \alpha_c$ and $\theta \rightarrow \frac{\pi}{2}$. Accordingly, $\sin\theta_c = 1$ and $\sin\alpha_c = 1-\delta$ is deduced out of Eq. 2.6. With $\alpha_c = 90° - \zeta_c$,

the latter relation is rewritten using some trigonometric approach as

$$\cos\zeta_c = 1 - \delta. \tag{2.7}$$

2.4.3 Image acquisition and three-dimensional image reconstruction

The term image hitherto employed denotes a radiographic acquisition of an object. Such a picture essentially suffers from the superimposition of structures aligned on the path of penetrating radiation and is simply known as projection. The solution to the limitation of radiographic imaging is the computed tomography, where transverse cuts (tomograms) of an object are reconstructed by acquiring several projections around it. This reconstruction reveals information on each structure contained in the object, hence the naming three-dimensional image reconstruction. In this section the reconstruction process is introduced, which mathematical principle can be drawn from e.g., [Kak and Slaney, 1988, Hsieh, 2009]. The experimental implementation by Cormack and Hounsfield may be found in [Cormack, 1963, Hounsfield, 1973].

Fourier slice theorem

A parallel geometry is considered in the following as sufficient for the understanding of the reconstruction process. Each two-dimensional projection recorded by the detector illustrates an intensity distribution, which relates to a physical value (the coefficient of absorption of the object) according to Eq. 2.2. The object is identified by a two-dimensional function $f(x, y)$ whose projection can be interpreted as a line integral. As projections are recorded in CT at several angles around the object, a cartesian coordinate system (x', y') can be induced, so that for any individual angle θ, the y' axis is parallel to the direction in which the projection is acquired. Thus, a line integral is expressed as

$$p_\theta(x') = \int f(x, y)\, \mathrm{d}y', \tag{2.8}$$

where x' is established as (see Fig. 2.4(a))

$$x' = x\cos\theta + y\sin\theta.$$

May Eq. 2.8 be rewritten via a Dirac function as

$$p_\theta(x') = \int_{-\infty}^{+\infty} \int_{-\infty}^{+\infty} f(x, y)\, \delta(x\cos\theta + y\sin\theta - x')\, \mathrm{d}x\mathrm{d}y, \tag{2.9}$$

then it designates the **Radon transform**. In order to obtain the **Fourier slice theorem**, it is primordially required to define a unidimensional Fourier transform of the Radon transform given by

$$P_\theta(\nu) = \int_{-\infty}^{+\infty} p_\theta(x') \exp(-\mathrm{i}2\pi\nu x')\, \mathrm{d}x'. \tag{2.10}$$

Secondly, it is mandatory to define the bidimensional Fourier transform of the object $f(x, y)$ as

$$F(u, v) = \int_{-\infty}^{+\infty} \int_{-\infty}^{+\infty} f(x, y) \exp[-\mathrm{i}2\pi(ux + vy)] \, \mathrm{d}x\mathrm{d}y, \tag{2.11}$$

where u and v identify the the spatial frequencies assigned to x and y respectively. A relation between the coordinates (θ, ν) and (u, v) is eligible as follows $(u, v) = (\nu\cos\theta, \nu\sin\theta)$ (see Fig. 2.4(b)). From this point, the Fourier slice theorem is settled through the link in Fourier space between the unidimensional Radon transform (Eq. 2.10) and the two-dimensional object (Eq. 2.11), that gives

$$P_\theta(\nu) = F(\nu\cos\theta, \nu\sin\theta). \tag{2.12}$$

In other words, a two-dimensional identity can be obtained in reverse for the one-dimensional Fourier transform $P_\theta(\nu)$ of a line integral at any given acquisition angle θ. It follows the recovery of the object in real space via an inverse Fourier transform as

$$f(x, y) = \int_{-\infty}^{+\infty} \int_{-\infty}^{+\infty} F(u, v)\exp[\mathrm{i}2\pi(ux + vy)] \, \mathrm{d}u\mathrm{d}v. \tag{2.13}$$

Nevertheless, a complete reconstruction of the object requires the interpolation from each point of a line integral to its neighbor, provided that the points stand on a circle of radius u (see Fig. 2.4(b)). Otherwise, artifacts emanate from the reconstruction. Therefore, the **filtered backprojection** is to date the favoured tomographic reconstruction alternative.

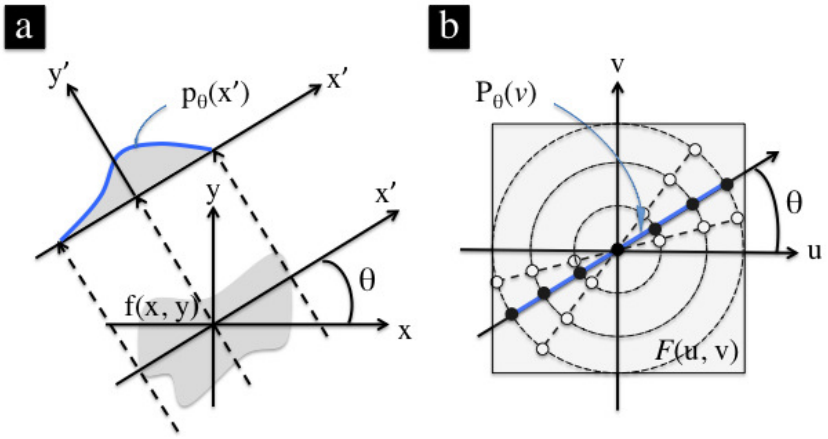

Figure 2.4: Sketch of the Fourier slice theorem. (a) Illustration in a cartesian coordinate system (x', y') of a projection $p_\theta(x')$ acquired at an angle θ from an object function $f(x, y)$. (b) A line defined $P_\theta(\nu)$ as through the two-dimensional Fourier transform $F(u, v)$ of the function $f(x, y)$ corresponds to the one-dimensional Fourier transform of a projection $p_\theta(x')$.

Filtered backprojection

The expression "filtered" states the suppression of high frequencies in the Fourier space before retrieving the object by an inverse Fourier transform. Applying a substitution of

$x' = x\cos\theta + y\sin\theta$ in Eq. 2.13 leads to the reconstruction of the object as follows

$$f(x,y) = \int_0^{\pi} \left[\int_{-\infty}^{+\infty} \underbrace{|\nu|}_{Filter} P_\theta(\nu) \exp(\mathrm{i}2\pi\nu x') \, \mathrm{d}\nu \right] \mathrm{d}\theta. \tag{2.14}$$

2.4.4 Dual-energy computed tomography

The contrast formation in attenuation-based X-ray imaging depends on the energy spectrum, the density of the sample elements and their effective atomic numbers (see section 2.4.1). Therefore, the contrast between the different components of a composite material varies according to the energy being optimal for one or the other component. In sum, for polychromatic spectra, the use of relatively different energy spectra (usually 2) may allow differentiation of at least two elements. It has initially been applied in clinical practice (see e.g., [Johnson et al., 2007, Primak et al., 2007]). This type of imaging relies on the differences of spectra. However, few aspects of dual-energy imaging are being reviewed today by performing for example multidetector CT [Karçaaltincaba and Aktas, 2011]. The first approach is addressed in the following as it is the most feasible procedure in our investigation. Regardless of the standard use of the dual-energy computed tomography (DECT) in clinical practice, it is in principle meaningful in laboratory-based X-ray systems.Tangible application of this imaging technique is shown on a gold ore sample in section 6.3.2.

Method

Dual-energy CT for the selection or differentiation of materials is based on separating their attenuation coefficients. While considering the attenuation coefficient of a two-material compound as a linear combination of photoelectric and Compton coefficient, the overall absorption could be written in the form [Alvarez and Macovski, 1976]

$$\mu(E) = \mu(E)_{\mathrm{p}} + \mu(E)_{\mathrm{c}}. \tag{2.15}$$

At low energies, where the photoelectric effect is most prominent, the absorption coefficient of low Z elements is related to the atomic number as $\mu \approx \rho_{\mathrm{e}} Z^4$. At high energies though, these elements display an absorption that depends uniquely on the electron density $\rho_{\mathrm{e}} Z$ due to the Compton scattering. Accordingly, Eq. 2.15 changes to

$$\mu(E) \approx \rho_{\mathrm{e}} {Z^4}_{\mathrm{tot}} \alpha(E) + \rho_{\mathrm{e}} Z \beta(E). \tag{2.16}$$

Here $\alpha(E)$ and $\beta(E)$ are some arbitrary functions and the term Z_{tot} stands for the effective atomic number of the materials. Provided that both materials have ideally distinct atomic numbers, their differentiation requires two measurements to be acquired respectively at low energy, where only the low Z elements are sensitive to the photoelectric effect and high energy, where high Z elements are more sensitive to the Compton effect.

Chapter 3

Phase-sensitive X-ray imaging

In this chapter another essential effect of the interaction of X-rays with the matter other than the absorption will be discussed. This event is the refraction which is responsible for the occurrence of phase shift within a material. The principle of the formation of phase contrast will be addressed and the notion of phase contrast established by the Fresnel diffraction will be largely detailed, as it needs to be understood before tackling the propagation-based PCI. Notions on imaging regimes in a parallel beam and the scaling to a cone-beam geometry are developed to make clear why holographic PCI can be performed in some laboratory especially commercial systems.

3.1 Phase-sensitive imaging techniques

In practice phase shifts are mostly accessible through a measurable physical quantity. The techniques that are mentioned in the following attempt to recover the phase information but differ from each other according to the instruments used or how the measured quantity is related to the phase. These techniques include:

Crystal interferometry (CI)

It owes its uniqueness to the fact that the phase shift, Φ, is directly measured out of the interference patterns. It has been initiated in hard X-ray regime by [Bonse and Hart, 1965], using three beam splitter crystals. The first splits the beam, the second redirects the splitted beams, whereas the third is used to recombine the waves that have passed through sample and air, respectively. It is a highly sensitive method that demands the collimation of the beam, and hence is available by preference at synchrotron sources.

Crystal analyzer-based imaging (ABI)

It is also known as diffraction-enhanced imaging (DEI). The measured quantity is proportional to the first derivative, $\frac{\partial\Phi(x,y)}{\partial z}$, of the phase. The analyzer crystal is set between the object and the detector in such a manner to reflect X-rays to the detector in only a small angular range meeting the Bragg conditions of the crystal [Goetz et al., 1979, Chapman

et al., 1997]. The equipment needed for this imaging procedure requires monochromatic flux, which can be best satisfied at synchrotron sources.

Grating-based imaging (GBI)

In addition to CI and ABI, they represent the interferometric methods or phase-contrast imaging. In the last case the relation between the phase and the measured quantity remains the same as in ABI. Due to the high coherence that can be delivered at synchrotron sources, this method was initially applied at these sources [Momose et al., 2003, Momose, 2005], and required only two gratings. The first grating – the phase grating, diffracts the X-ray radiation and creates a carpet of periodic interference patterns called Talbot carpet. The second grating is the so called analyzer grating, whose functionality is to enable the measurement of intensity changes linked to the transverse shift caused by the object. By placing an additional third grating (absorbing mask) in front of the source, the coherence of the beam was demonstrated to increase at conventional X-ray tubes [Pfeiffer et al., 2006]. This lead to application of this interferometric method at research laboratory setups [Weitkamp et al., 2005, Pfeiffer et al., 2007]. Reference [Bech, 2009] is suggested for introduction to the GBI.

Propagation-based imaging (PBI)

This technique also referred to as **inline phase-contrast imaging** is a non-interferometric imaging method and relies on the propagation of the waves in free space after interaction with the object. Instead of the wave field, the intensities are measured while the phase information is lost. This is known as the phase problem. Since the intensities are proportional to the second derivative of the phase $\left(\frac{\partial^2\Phi(x,y)}{\partial z^2}\right)$, latter is retrieved with the use of appropriate numerical phase reconstruction procedures. The intensities are literally made of patterns which emanate from the Fresnel diffraction when the sample is illuminated by a spatially coherent source. Thus the method was introduced at synchrotrons until the fulfillment of spatial coherence with microfocus sources [Wilkins et al., 1996].

3.2 X-rays propagation and phase-contrast imaging

This section describes one of the main motivations of this work namely the inline phase-contrast imaging with laboratory X-ray devices. Prior to the experimental investigation in the next chapter it is convenient to discuss here the concept of image formation using the behavior of the X-ray wave field, even though the measurable value is the intensity. Therefore, the X-ray wave field propagation in free space and its modification after the interaction with a specimen of defined thickness Δr and refractive index n is described. Accordingly, the concepts of paraxial and projection approximation are shortly introduced. Given the fact that the presented systems have a divergent X-ray beam, wave field propagation in a cone geometry is presented through the Fresnel scaling theorem to show where possible the equivalence to the propagation of a plane wave.

3.2.1 X-ray waves propagation in free space

The electromagnetic wave propagation in absence of matter is described by the Maxwell's equations (see e.g ref. [Paganin, 2006])

$$\begin{array}{rcl} \nabla \cdot \mathbf{E}(\mathbf{r},t) & = & 0, \\ \nabla \cdot \mathbf{B}(\mathbf{r},t) & = & 0, \\ \nabla \times \mathbf{E}(\mathbf{r},t) & = & -\partial_t \mathbf{B}(\mathbf{r},t), \\ \nabla \times \mathbf{B}(\mathbf{r},t) & = & \epsilon_0 \mu_0 \partial_t \mathbf{E}(\mathbf{r},t). \end{array} \tag{3.1}$$

The evolution of the electric field $\mathbf{E}(\mathbf{r},t)$ and magnetic field $\mathbf{B}(\mathbf{r},t)$ are space and time dependent and governed by the equations enumerated above. At a time t, any point is described with its cartesian coordinates $\mathbf{r} = (x,y,z)$. The electrical permittivity and magnetic permeability of free space are respectively defined by ϵ_0 and μ_0. Equations 3.1 can be transformed into vacuum field equations related individually to $\mathbf{E}(\mathbf{r},t)$ and $\mathbf{B}(\mathbf{r},t)$ [Paganin, 2006]:

$$\begin{array}{rcl} (\epsilon_0 \mu_0 {\partial_t}^2 - \nabla^2)\mathbf{E}(\mathbf{r},t) & = & 0, \\ (\epsilon_0 \mu_0 {\partial_t}^2 - \nabla^2)\mathbf{B}(\mathbf{r},t) & = & 0. \end{array} \tag{3.2}$$

Assuming no polarization effects, the scalar theory applies and the electromagnetic field is then described by a single complex scalar field $\Psi(\mathbf{r},t)$ as

$$(\epsilon_0 \mu_0 {\partial_t}^2 - \nabla^2)\Psi(\mathbf{r},t) = 0. \tag{3.3}$$

A monochromatic plane wave $\Psi_\omega(\mathbf{r},t)$ with angular frequency ω is considered as solution of Eq. 3.3 if $\epsilon_0 \mu_0 = \frac{k^2}{\omega^2}$, where $k = \frac{2\pi}{\lambda}$ is the wave number, and λ the wavelength. In a given volume of free space, the complex scalar function is written as a spectral decomposition into superimposed monochromatic fields [Paganin, 2006]

$$\Psi(\mathbf{r},t) = \frac{1}{\sqrt{2\pi}} \int_0^\infty \psi_\omega(\mathbf{r}) \exp(-i\omega t)\, \mathrm{d}\omega, \tag{3.4}$$

where the time independent term $\phi_\omega(\mathbf{r})$ is the stationary spatial wave function, and $\exp(-i\omega t)$ the harmonic time dependence of each monochromatic component of the field. A substitution of Eq. 3.4 in Eq. 3.3 allows the decomposition to appear in a solvable equation by interchanging the order of integration and differentiation. While the differentiation is performed with respect to the time and the relation $c = \frac{\omega}{k} = \frac{1}{\sqrt{\epsilon_0 \mu_0}}$ is considered, where c is the speed of light, Eq. 3.3 turns to

$$(k^2 + \nabla^2)\psi_\omega(\mathbf{r}) = 0. \tag{3.5}$$

This time-independent equation is known as **Helmholtz equation** and describes the evolution of any stationary wave function that represents a component of the spectral decomposition. Let's examine the propagation of such a component in vacuum from a plane perpendicular to the optical axis at $z = 0$ to another plane at $z > 0$. This elementary plane wave is expressed as $\psi^{\mathbf{PW}}(\mathbf{r}) = \exp(i\mathbf{k}.\mathbf{r})$ and propagates along a wave vector $\mathbf{k} = (k_x, k_y, k_z)$.

If the relation ${k_x}^2 + {k_y}^2 + {k_z}^2 = k^2 = \frac{\omega^2}{c^2}$ is satisfied, the Helmholtz equation (3.5) has $\psi^{(PW)}(\mathbf{r})$ as solution. The solutions to this equation in planes perpendicular to the optical axis $\mathbf{r}_\perp = (x, y)$ take the form

$$\psi^{(\mathrm{PW})}(\mathbf{r}_\perp, z) = \exp\left[\mathrm{i}\mathbf{k}_\perp \cdot \mathbf{r}_\perp\right] \exp\left[\mathrm{i}z\sqrt{k^2 - {k_\perp}^2}\right] \tag{3.6}$$

where the term $\exp\left[\mathrm{i}z\sqrt{k^2 - {k_\perp}^2}\right]$ is the transfer function also known as the free space propagator. In essence, the determination of the wave field $\psi^{(\mathbf{PW})}(\mathbf{r}_\perp, z)$ in a plane at $z > 0$ is given by the multiplication of the wave field $\psi^{(\mathbf{PW})}(\mathbf{r}_\perp, 0)$ at $z = 0$ with the free space propagator. The extension of this method to any input field $\psi(\mathbf{r}_\perp, 0)$ can be decomposed into its spectral components applying a two-dimensional Fourier integral

$$\psi(\mathbf{r}_\perp, 0) = \frac{1}{2\pi} \iint \tilde{\psi}(\mathbf{k}_\perp, 0) \exp\left[\mathrm{i}\mathbf{k}_\perp \cdot \mathbf{r}_\perp\right] \mathrm{d}\mathbf{k}_\perp. \tag{3.7}$$

The two-dimensional transform of $\psi(\mathbf{r}_\perp, 0)$ with respect to x and y is denoted by $\tilde{\psi}(\mathbf{k}_\perp, 0)$. Considering the multiplication by the transfer function, the propagated wave field at a distance z is obtained as

$$\psi(\mathbf{r}_\perp, z) = \frac{1}{2\pi} \iint \tilde{\psi}(\mathbf{k}_\perp, 0) \exp\left[\mathrm{i}z\sqrt{k^2 - {k_\perp}^2}\right] \exp\left[\mathrm{i}\mathbf{k}_\perp \cdot \mathbf{r}_\perp\right] \mathrm{d}\mathbf{k}_\perp. \tag{3.8}$$

By using the notation $\mathcal{F}_\perp$ and ${\mathcal{F}_\perp}^{-1}$ respectively for the Fourier transform and Fourier back transform with respect to the x and y, Eq. 3.8 may be written as

$$\psi(\mathbf{r}_\perp, z) = {\mathcal{F}_\perp}^{-1}\Big[\exp\left(\mathrm{i}z\sqrt{k^2 - {k_\perp}^2}\right)\mathcal{F}_\perp\left[\psi(\mathbf{k}_\perp, 0)\right]\Big]. \tag{3.9}$$

and represents the **free space propagation** of electromagnetic fields in vacuum. Thus, the propagation of an arbitrary wave $\psi(\mathbf{r}_\perp, 0)$ over a distance z is described by the operator

$$\mathcal{D}_z = {\mathcal{F}_\perp}^{-1} \exp\left(\mathrm{i}z\sqrt{k^2 - {k_\perp}^2}\right)\mathcal{F}_\perp. \tag{3.10}$$

3.2.2 Fresnel diffraction

The notion of paraxial approximation is introduced in this section assuming that the wave field form small angles with respect to the optical axis. This may be valid for the divergence of the X-ray beam provided by microfocus tubes, while the illuminated samples are relatively small in size. Such an approximation is well-founded provided that $k^2 \gg {k_\perp}^2$. Hence, the root in the transfer function initially mentioned in Eq. 3.6 can be transformed using the binomial approximation at the second order

$$\sqrt{k^2 - {k_\perp}^2} \simeq k - \frac{{k_\perp}^2}{2k}, \tag{3.11}$$

and substituted in Eq. 3.9 reads

$$\psi(\mathbf{r}_\perp, z) \simeq \exp(\mathrm{i}kz)\mathcal{F}_\perp{}^{-1}\Big[\exp\Big(\frac{-\mathrm{i}zk_\perp{}^2}{2k}\Big)\mathcal{F}_\perp\big[\psi(\mathbf{k}_\perp, 0)\big]\Big]. \tag{3.12}$$

This Equation (3.12) is defined as the **Fresnel diffraction** and describes the propagation of paraxial wave fields in vacuum. Consequently its operator is written as

$$\mathcal{D}_z{}^{\mathcal{F}} = \exp(\mathrm{i}kz)\mathcal{F}_\perp{}^{-1}\exp\Big(\frac{-\mathrm{i}zk_\perp{}^2}{2k}\Big)\mathcal{F}_\perp. \tag{3.13}$$

If Eq. 3.13 would be rewritten in real-space form, the Fresnel propagator may be formulated as [Paganin, 2006, Saleh, 1991]

$$\begin{aligned} h(\mathbf{r}_\perp, z) &= \tfrac{1}{2\pi}\exp(\mathrm{i}kz)\mathcal{F}_\perp{}^{-1}\exp\Big(\tfrac{-\mathrm{i}zk_\perp{}^2}{2k}\Big) \\ &= \tfrac{-\mathrm{i}k\exp(\mathrm{i}kz)}{2\pi z}\exp\Big(\tfrac{\mathrm{i}kr_\perp^2}{2z}\Big), \end{aligned} \tag{3.14}$$

which allows to express Eq. 3.12 by a convolution

$$\psi(\mathbf{r}_\perp, z) = \psi(\mathbf{r}_\perp, 0) \otimes h(\mathbf{r}_\perp, z). \tag{3.15}$$

With both Eq. 3.12 and 3.14 the **Fresnell-Kirchoff** diffraction integral is deduced

$$\psi(\mathbf{r}_\perp, z) \simeq \frac{-\mathrm{i}k\exp(\mathrm{i}kz)}{2\pi z}\iint \psi(\mathbf{r}'_\perp, 0)\exp\Big[\frac{\mathrm{i}k(\mathbf{r}_\perp - \mathbf{r}'_\perp)}{2z}\Big]\,\mathrm{d}\mathbf{r}'_\perp. \tag{3.16}$$

which symbolizes the convolution formulation of Fresnel diffraction. The script $(\mathbf{r}'_\perp, 0)$ indicates each point in the input plane, from where a divergent wave with a complex amplitude $\psi(\mathbf{r}'_\perp, 0)$ originates.

3.2.3 X-ray waves interaction with matter and phase shift

It can be reasonably proceeded from the scalar wave equation function (Eq. 3.3) which in presence of matter reads

$$\Big(\epsilon(\mathbf{r})\mu_0\partial_t{}^2 - \nabla^2\Big)\psi(\mathbf{r}, t) = 0, \tag{3.17}$$

where the refractive index in presence of matter relates to the corresponding permittivity $\epsilon(\mathbf{r})$ as $n(\mathbf{r}) = \sqrt{\frac{\epsilon(\mathbf{r})}{\epsilon_0}}$. Consequently, the wave equation in presence of a medium can be expressed as follows

$$\Big(\frac{n^2(\mathbf{r})}{c^2}\partial_t{}^2 - \nabla^2\Big)\psi(\mathbf{r}, t) = 0. \tag{3.18}$$

For any plane wave solution of this equation, the time-independent inhomogeneous Helmholtz equation is written as

$$\Big(\nabla^2 + n^2(\mathbf{r})k^2\Big)\psi(\mathbf{r}, t) = 0. \tag{3.19}$$

Assuming two parallel planes at boundaries $z = 0$ and $z = z_0$ of a medium (see Fig. 3.1(a)) a plane wave $\psi_{\mathrm{E}}(\mathbf{r})$ impinging on it is disrupted due to the scattering in the object. If the wave $\psi_{\mathrm{S}}(\mathbf{r})$ at z_0 of the form $\psi_{\mathrm{S}}(\mathbf{r}) = A(\mathbf{r})\exp(\mathrm{i}kz)$ obeys the inhomogeneous Helmholtz equation (3.19), whereas $A(\mathbf{r})$ is the complex envelope and $\exp(\mathrm{i}kz)$ the unscattered plane wave, it can be substituted in this equation and gives

$$\left(2\mathrm{i}k\frac{\partial}{\partial z} + \nabla_{\perp}^2 + \left[n^2(\mathbf{r}) - 1\right]\right)A(\mathbf{r}) = 0, \tag{3.20}$$

by neglecting the second derivative in z. Here, $\nabla_{\perp}^2 = \frac{\partial^2}{\partial x^2} + \frac{\partial^2}{\partial y^2}$ is the transverse Laplacian. The projection approximation which is introduced here considers that all changes to the wave field at the surface z_0, due to the phase and amplitude shifts are accumulated along streamlines of the unscattered beam [Paganin, 2006]. With reference to Fig. 3.1(b) this approximation is satisfied if the radius of the first **Fresnel zone** $\sqrt{\lambda z}$ corresponding to the Fresnel diffraction in the object is smaller than the spatial resolution $\Delta\mathbf{r}_{\perp}$ of the imaging system:

$$\sqrt{\lambda\Delta\mathrm{t}} < \Delta\mathbf{r}_{\perp}. \tag{3.21}$$

Hence, at a given resolution of the imaging system, the thickness $\Delta\mathrm{t}$ of the object in the projection approximation should meet the relation $\Delta\mathrm{t} < \frac{\Delta\mathbf{r}_{\perp}^2}{\lambda}$. Provided that Eq. 3.21 is fulfilled and using the first order Taylor approximation in δ and β in the term $\left[1 - n^2(\mathbf{r})\right]$, the Helmholtz equation 3.20 would yield

$$\frac{\partial}{\partial z}A(\mathbf{r}) \simeq -\mathrm{i}k\left[\delta(\mathbf{r}) - \mathrm{i}\beta(\mathbf{r})\right]. \tag{3.22}$$

Considering $\psi(\mathrm{r}_{\perp}, z = 0) = A(\mathrm{r}_{\perp}, 0)$, the wave field in the form $\psi(\mathrm{r}_{\perp}, \Delta\mathrm{t}) = A(\mathrm{r}_{\perp}, \Delta\mathrm{t})\exp(ik\Delta\mathrm{t})$ behind the object of thickness $\Delta\mathrm{t}$ is given by

$$\psi(\mathrm{r}_{\perp}, \Delta\mathrm{t}) \simeq \underbrace{\psi(\mathrm{r}_{\perp}, 0)\exp(\mathrm{i}k\Delta z)}_{\text{vacuum propagation}}\underbrace{\exp[-\mathrm{i}k\delta(\mathbf{r})\Delta\mathrm{t}]}_{\text{phase shift}}\underbrace{\exp[-k\beta(\mathbf{r})\Delta\mathrm{t}]}_{\text{decay}}. \tag{3.23}$$

This equation can properly be expressed as time-dependent (see [Attwood, 2007]). With the definition of the intensity as $I = |\psi|^2$, the attenuation of the photons beam expressed in Eq. 2.2 is by analogy related to the decay of the wave amplitude behind the object, which is displayed by the term with the red highlight in Eq. 3.23. Implying that $\frac{2\pi\beta}{\lambda} = \frac{\mu}{2}$ the absorption coefficient μ relates to the imaginary part of the refractive index as

$$\mu = 2k\beta(\mathbf{r}). \tag{3.24}$$

The photoelectric and Compton scattering are mainly attributed the cause of the decay of the wave amplitude, while the Rayleigh scattering is held liable for the phase shift (Fig. 2.3(a)). Thus the term featured by the blue brace in Eq. 3.23 stands for the phase shift $\Delta\phi$ in the medium, compared to vacuum and reads

$$\Delta\phi = -k\delta(\mathbf{r})\Delta\mathrm{t}, \tag{3.25}$$

By using Eq. 3.24 and 3.25, the expression denoted as optical transmission function $\tau(\mathbf{r}_\perp)$ can be introduced

$$\tau(\mathbf{r}_\perp) \approx \exp\left[\mathrm{i}\phi(\mathbf{r}_\perp) - \frac{\mu(\mathbf{r}_\perp)\Delta\mathrm{t}}{2}\right]$$

so that the disrupted wave field can summarizes to

$$\psi(\mathrm{r}_\perp, \Delta\mathrm{t}) \approx \tau(\mathbf{r}_\perp)\psi(\mathrm{r}_\perp, 0). \tag{3.26}$$

Provided that small absorption and phase shift assumption (weak object approximation) is validated, a Taylor expansion can be performed for the transmission function. At the first order, it yields

$$\tau(\mathbf{r}_\perp) \approx 1 + \mathrm{i}\phi(\mathrm{r}_\perp) - \frac{\mu_t(\mathbf{r}_\perp)}{2}. \tag{3.27}$$

where $\mu_t(\mathbf{r}_\perp) = \mu(\mathbf{r}_\perp)\Delta\mathrm{t}$.

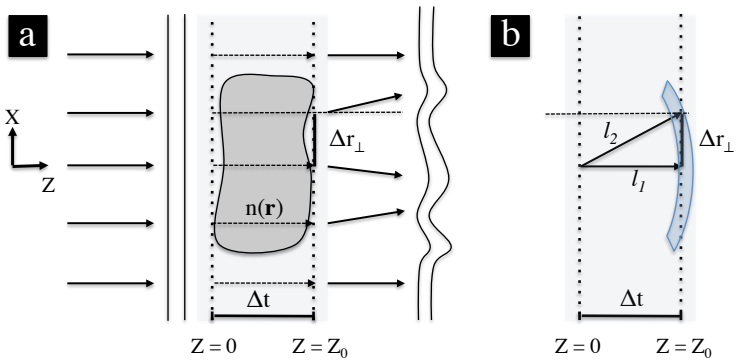

Figure 3.1: Sketch of the X-ray wave propagation after interaction with an object of thickness $\Delta\mathrm{t}$ and refractive index $n(\mathbf{r})$. (a) A distortion of the penetrating wave is noticeable behind the plane $z = z_0$ bounding the object. (b) The region between the planes bounding the medium ($z = 0$ and $z = z_0$) is reproduced and shows the first Fresnel zone encompassed by the radii l_1 and l_2. The spatial resolution achieved by the imaging system is indicated by $\Delta\mathbf{r}_\perp$. Adapted from [Krüger, 2011].

3.2.4 Contrast transfer function and imaging regimes

In Fourier space, the propagated wave-field at a distance $z \geq 0$ is given by

$$\begin{aligned} \tilde{\psi}(\mathbf{k}_\perp, z) &= \tilde{\tau}(\mathbf{k}_\perp) \cdot \tilde{h}(\mathbf{k}_\perp, z) \\ &\approx \left[\delta(\mathbf{k}_\perp) + \mathrm{i}\tilde{\phi}(\mathbf{k}_\perp) - \tfrac{\tilde{\mu}_t(\mathbf{k}_\perp)}{2}\right] \exp(\mathrm{i}kz) \exp\left[\tfrac{-\mathrm{i}z(\mathbf{k}_\perp^2)}{2k}\right], \end{aligned} \tag{3.28}$$

where $\sim$ stands for the Fourier transform of the covered script. From the expression of the intensity $I(\mathbf{r}_\perp, z) = |\psi(\mathbf{r}_\perp, z)|^2$ it follows in Fourier space

$$\begin{aligned} \tilde{I}(\mathbf{k}_\perp, z) &= \mathcal{F}|\psi(\mathbf{r}_\perp, z)|^2 \\ &\approx 2\pi\delta_D(\mathbf{k}_\perp) + 2\tilde{\phi}(\mathbf{k}_\perp)\sin\left[\chi(\mathbf{k}_\perp, z)\right] - \tilde{\mu}_t(\mathbf{k}_\perp)\cos\left[\chi(\mathbf{k}_\perp, z)\right], \end{aligned} \tag{3.29}$$

with $\chi(\mathbf{k}_\perp, z) = (\frac{z}{2k}.\mathbf{k}_\perp^2) \iff \chi(\nu, z) = (\pi\lambda z\nu^2)$. Here, ν denotes the frequency and δ_D the Dirac delta function (see [Bartels, 2013], Appendix A.2). The terms $\sin\chi$ and $\cos\chi$ from Eq. 3.29 are known respectively as the **phase-contrast transfer function (PCTF)** and **amplitude contrast transfer functions (ACTF)** of the Fresnel diffraction pattern. They are shown in Fig. 3.2 as a function of the reduced radial spatial frequency $\sqrt{\lambda z}\nu$ [Pogany et al., 1997]. It is indicated in this figure that the contrast formation in X-ray propagation imaging depends on the property of both the phase and the amplitude at a given spatial frequency. Therefore, different imaging regimes are ensued. It is convenient to define here the Fresnel number

$$F = \frac{\Delta\mathbf{r}_\perp^2}{\lambda z} \tag{3.30}$$

which determines the degree of diffraction for a feature of lateral extent $\Delta\mathbf{r}_\perp$.

Contact plane regime

It prevails at the exit-plane of the object, where the amplitude contrast is maximal. This dominates the intensity distribution in this regime, since the PCTF tends to zero. Hence the regime corresponds to Fresnel numbers large above unity ($F \gg 1$).

Direct phase regime

With increasing distances z and accordingly decreasing Fresnel numbers, the amplitude drops whereby the PCTF arises. This is explained by the diffraction at high spatial frequencies also considered as edges. For this reason the regime is interpreted as edge enhancement regime [Cloetens et al., 1999].
Given that z varies, it is meaningful to consider the contrast evolution according to changes in intensity. By using a wave-field which relates to an intensity as

$$A(\mathrm{r}) = \sqrt{I(\mathrm{r})}\exp(\mathrm{i}\phi(\mathrm{r})),$$

the paraxial Helmholtz equation is solved for this wave if

$$(2\mathrm{i}k\partial_z + \nabla_\perp^2)\sqrt{I(\mathrm{r})}\exp(\mathrm{i}\phi(\mathrm{r})) = 0, \tag{3.31}$$

where $\nabla_\perp^2 = \frac{\partial^2}{\partial x^2} + \frac{\partial^2}{\partial y^2}$ is the Laplacian operator. As a reformulation of Eq. 3.31, the **transport-of-intensity equation (TIE)** is derived as

$$\nabla_\perp\big[I(\mathrm{r})\nabla_\perp\phi(\mathrm{r})\big] = -k\frac{\partial I(\mathrm{r})}{\partial z}. \tag{3.32}$$

In the context of contrast formation in near-field, where the direct phase regime prevails, small propagation distances rule and $\sin\chi = \chi$ is assumed. Consequently, the TIE is a duly representative approach to the contrast transfer function (CTF) in the specific case of low absorption and reads

$$\frac{I(\mathbf{r}_\perp, \Delta z)}{I(\mathbf{r}_\perp, z)} \approx 1 - \frac{\Delta z}{k}\nabla_\perp^2\phi(\mathbf{r}_\perp). \tag{3.33}$$

Holographic regime

When the propagation distance is further increased, the PCTF and ACTF oscillate rapidly with the spatial frequency, whereby the Fresnel number lays considerably under unity but exceed 0.1. This interval comprises partially the near-field and the far-field holographic domain. To Fresnel numbers widely below 0.1, the intensity fluctuation is described by the Fraunhofer diffraction, thus the appellation Fraunhofer regime.

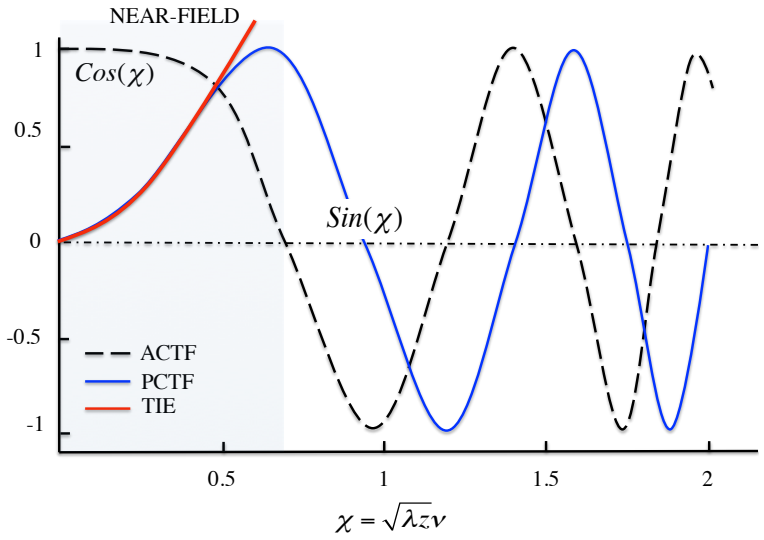

Figure 3.2: Contrast transfer function of the X-ray propagation based imaging assuming small variation of absorption in the object. The amplitude and phase as function of the dimensionless coordinate $\sqrt{\lambda z}\nu$ are indicated by ACTF and PCTF, respectively, where z is the propagation distance after the object in a parallel beam geometry, ν the spatial frequency and λ the wavelength. The transport-of-intensity equation (TIE), which also describes very well the contrast transfer at small propagation distances is shown here for a pure phase object.

3.2.5 Fresnel scaling theorem

The consideration of the propagation of a divergent wave-field as a plane wave illumination is discussed in this section [Paganin, 2006]. By using the paraxial approximation, a divergent wave-field $\psi(\mathrm{r}_\perp, 0)$ at the exit-surface of an object $z = 0$, but originating in a radius z_1 before this surface, is related to a plane-wave illumination $\psi^{(\mathrm{P})}(\mathrm{r}_\perp, 0)$ as

$$\psi^{(z_1)}(\mathrm{r}_\perp, 0) = \psi(\mathrm{r}_\perp, 0) \exp\left[\frac{ik}{2z_1}(x^2 + y^2)\right].$$

Here, z_1 denotes the distance from the point-source to the exit-surface plane $z = 0$ of the object. The propagation of this wave from $z = 0$ to a distance $z = z_2 > 0$ using the

Fresnel-Kirchoff integral yields

$$\begin{aligned}\psi^{(\mathrm{P})}(\mathrm{r}_\perp, z=z_2) \;=\; & \overbrace{\frac{-ik\exp(\mathrm{i}kz_2)}{2\pi z_2}}^{A(z_2)} \exp\left[\tfrac{\mathrm{i}k(\mathrm{r}'^2_\perp)}{2z_2}\right] \\ & \times \iint \psi^{(\mathrm{P})}(\mathrm{r}'_\perp, z=0)\exp\left[\tfrac{\mathrm{i}k}{2}\mathrm{r}'^2_\perp(\tfrac{1}{z_2}+\tfrac{1}{z_1})\right] \\ & \times \exp\left[\tfrac{\mathrm{i}k}{z_2}\mathrm{r}_\perp\cdot\mathrm{r}'_\perp\right]\mathrm{d}\mathrm{r}'_\perp.\end{aligned} \tag{3.34}$$

A reference to the geometric magnification in a cone beam geometry

$$M := \frac{z_1+z_2}{z_1},$$

transposable to

$$\frac{1}{z_1}+\frac{1}{z_2}=\frac{M}{z_2}$$

allows the relation

$$\left|A\Big(\frac{z_2}{M}\Big)\right| = M\Big|A(z_2)\Big|.$$

Hence the amplitude of the wave-field $\psi(\mathrm{r}'_\perp, z_2)$ can be expressed as

$$\left|\psi(\mathrm{r}'_\perp, z_2)\right| = \left|\frac{1}{M}A\Big(\frac{z_2}{M}\Big)\right| \cdot \left|\int \psi^{(\mathrm{P})}(\mathrm{r}_\perp, 0)\exp\left[\frac{\mathrm{i}k(\mathrm{r}_\perp^2)}{2\frac{z_2}{M}}\right]\exp\left[-\mathrm{i}k\frac{\mathrm{r}_\perp\cdot\left(\frac{\mathrm{r}'_\perp}{M}\right)}{\frac{z_2}{M}}\right]\mathrm{d}\mathrm{r}'_\perp\right|. \tag{3.35}$$

Alongside a distance $z=\frac{z_2}{M}$ Eq. 3.35 is assimilable to the amplitude of a planar envelope $\psi^{(\mathrm{P})}(\mathrm{r}_\perp, 0)$ evaluated at the position $\frac{\mathrm{r}'_\perp}{M}$. Accordingly, the planar wave is given by

$$\left|\psi^{(\mathrm{P})}\Big(\frac{\mathrm{r}'_\perp}{M}, \frac{z_2}{M}\Big)\right| = \left|A\Big(\frac{z_2}{M}\Big)\right| \cdot \left|\int \psi^{(\mathrm{P})}(\mathrm{r}_\perp, 0)\exp\left[\frac{\mathrm{i}k(\mathrm{r}_\perp^2)}{2\frac{z_2}{M}}\right]\exp\left[-\mathrm{i}k\frac{\mathrm{r}_\perp\cdot\left(\frac{\mathrm{r}'_\perp}{M}\right)}{\frac{z_2}{M}}\right]\mathrm{d}\mathrm{r}'_\perp\right|. \tag{3.36}$$

It is sufficient to establish the relation

$$Z_{\mathrm{eff}} = \frac{z_2}{M}$$

defined as the **effective propagation distance** to outline that a wave-field issued from a point source at a distance z_1 from the object plane and propagated on a distance z_2 after the object plane with a lateral extent $\mathrm{r}'_\perp$, is equal to the amplitude of a planar wave-field propagated on a the distance Z_{eff} with a lateral extent $\frac{\mathrm{r}'_\perp}{M}$ [Pogany et al., 1997]. The **Fresnel scaling theorem** is then derived as follows

$$\left|\psi(\mathrm{r}'_\perp, z_2)\right| = \frac{1}{M}\left|\psi^{(\mathrm{P})}\Big(\frac{\mathrm{r}'_\perp}{M}, Z_{\mathrm{eff}}\Big)\right|. \tag{3.37}$$

Since the intensity is the quantity accessible at the measurement by the detector, using its

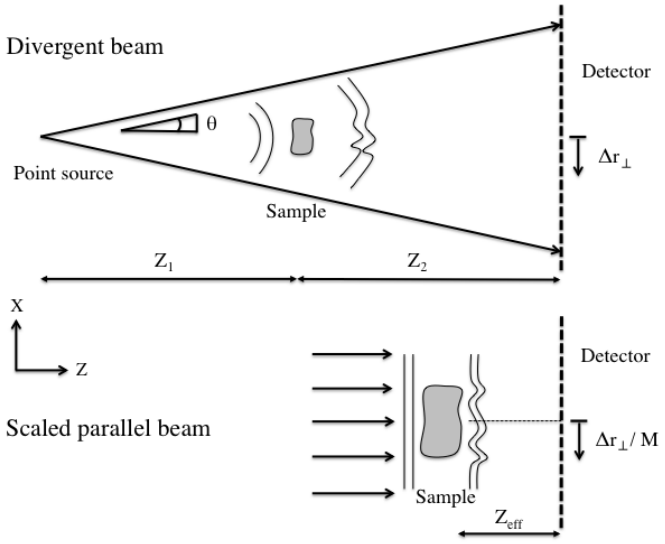

Figure 3.3: Illustrative description of the Fresnel scaling theorem, which sets the circumstances of equivalence between a point source and a parallel beam imaging. Considering the paraxial and the projection approximation, a diffraction pattern viewed by a detector at a distance z_2 and issued from an object illuminated by a point-source at a distance z_1, is assimilable to a diffraction pattern recorded at a distance $Z_{\text{eff}} = \frac{z_2}{M}$ after a object illuminated by a parallel-beam. The geometric magnification in the point source system is indicated by M. Accordingly, the system resolution in the equivalent parallel beam is denoted by $\frac{\Delta r_\perp}{M}$.

usual relation to the wave-field $I(\mathbf{r}) = |\psi(\mathbf{r})|^2$, allows the rewriting of the Fresnel scaling theorem in terms of intensities as follows

$$I(\mathrm{r}_\perp, z_2) = \frac{1}{M^2} I^{(\mathrm{P})}\left(\frac{\mathrm{r}_\perp^{'}}{M}, z = \frac{z_2}{M}\right). \tag{3.38}$$

3.2.6 Coherence

A relevant quantity for PBI is the transversal coherence length l_c also referred to as spatial coherence length. It describes the ability of X-rays of identical wavelength to interfere in a lateral expanse after a certain distance of propagation, although their directions might differ moderately due to the divergence $\Delta\theta$ caused by the finite size of the sources. It is expressed as [Cloetens, 1999]

$$l_c = \frac{\lambda}{2\Delta\theta} = \frac{\lambda R}{S}, \tag{3.39}$$

where R is the distance from the source to the object plane and S the source extent. At a point source system of cone-beam geometry satisfying the small angular approximation, it is perceptible according to Eq. 3.39 that a high coherence length is achievable.

3.3 Phase retrieval

The processing of a single signal recorded in grating-based interferometric PCI has been demonstrated to provide three image modalities, namely the absorption, phase and dark-field images [Pfeiffer et al., 2009, Bech et al., 2010]. In propagation-based PCI though, the phase recovering is achieved through a post-processing phase-retrieval step. Several phase-retrieval procedures are proposed and derivate from the TIE, the CTF or from an approach that combines both [Langer et al., 2008]. Therefore, this section is dedicated to operations meant to solve the phase problem, which arises from the fact that intensities are measured instead of the wave field.

3.3.1 Derivation from the TIE

The contrast in an image has been shown in Fig. 3.2 to be sensitive either to amplitude or the phase according to the distance of propagation. However, the attenuation property of the sample matters for establishing the appropriate phase reconstruction. Hence, some cases of phase retrieval based on this property are distinguishable.

Pure phase object

It denotes the case of no absorption at all. The TIE for such an assumption is then expressed as

$$I(\mathrm{r}_\perp, z) \simeq 1 - \frac{z}{k}\nabla_\perp^2 \phi(\mathrm{r}). \tag{3.40}$$

This is relevant for flat objects where the thickness is very low ($\Delta z \to 0$). The regime of small propagation distances still rules so that for a known intensity $I(r_\perp, z)$, the phase is carried by

$$\phi(\mathrm{r}_\perp) = -\frac{k}{z}\nabla_\perp^{-2}(I(\mathrm{r}_\perp, z) - 1). \tag{3.41}$$

Use can be made of the Fourier representation of the inverse Laplacian $\nabla_\perp^{-2}$ [Paganin, 2006]

$$\nabla_\perp^{-2} = -\mathcal{F}^{-1}\left[\frac{1}{k_\perp^2}\mathcal{F}\right]$$

to grant the following expression for the phase

$$\boxed{\phi(\mathrm{r}_\perp) = -\frac{k}{z}\mathcal{F}^{-1}\left[\frac{\mathcal{F}\left[I(\mathrm{r}_\perp, z) - 1\right]}{k_\perp^2}\right].} \tag{3.42}$$

As the TIE describes very well the changes of intensities with small propagation distances and for any kind of interaction with the object, solving it implies in general to inversely determine the wave-field at a preceding surface such as the exit-surface ($z = 0$). Accordingly, when the absorption in an object is not negligible but varies slowly (weak objects), the phase

of the wave-field is given by [Bronnikov, 2002]

$$\boxed{\phi(\mathrm{r}_\perp) = -\frac{k\Delta \mathrm{r}_\perp^2}{z}\mathcal{F}^{-1}\left[\frac{\mathcal{F}\left[\frac{I(\mathrm{r}_\perp,z)}{I(\mathrm{r}_\perp,z=0)}-1\right]}{k_\perp^2}\right].} \tag{3.43}$$

Modified Bronnikov algorithm (MBA)

The previous equation 3.43 requires the measurement of the contact image $I(\mathrm{r}_\perp, z = 0)$, which represents an issue in common cone-beam geometry, where only the sample stage moves. The effective propagation distance compared to a parallel beam is though given by $Z_{\text{eff}} = \frac{z_1 \times z_2}{z_1+z_2}$. An approach of solution to this challenge is therefore to achieve a phase reconstruction from a single measurement of the object as suggested in [Groso et al., 2006a], [Groso et al., 2006b]:

$$\boxed{\phi(\mathrm{r}_\perp) \simeq -\frac{k\Delta \mathrm{r}_\perp^2}{z}\mathcal{F}^{-1}\left[\frac{\mathcal{F}\left[I(\mathrm{r}_\perp,z)-1\right]}{k_\perp^2+\alpha}\right],} \tag{3.44}$$

where α is a regularization variable, chosen semi-empirically by evaluating the quality of the phase reconstruction.

Single material (SM)

In this case, the object is thought to be made of a unique known material. Hence it is evident that the decrement and the absorption term of the object's complex refractive index can be accessed from literature [Henke et al., 1993]. The propagation-based phase-contrast image viewed as intensity may be expressed as [Paganin, 2006]

$$I(\mathrm{r}_\perp, z) = \left(1 - \frac{\delta}{\mu}\nabla_\perp^2\right)\exp\Big[-\mu T(\mathrm{r}_\perp)\Big], \tag{3.45}$$

where $\mu = \frac{4\pi}{\lambda}\beta$ is the absorption coefficient of the material and $T(\mathrm{r}_\perp)$ its projected thickness. By applying the Fourier representation of the Laplacian, Eq. 3.45 is solved for the thickness as

$$T(\mathrm{r}_\perp) = -\frac{1}{\mu}\log\left(\mathcal{F}^{-1}\left[\frac{\mathcal{F}\left[I(\mathrm{r}_\perp,z)\right]}{1+\left(\frac{\delta}{\mu}z\right)k_\perp^2}\right]\right). \tag{3.46}$$

According to Eq. 3.25 the single material phase retrieval [Paganin et al., 2002] is resumed to

$$\boxed{\phi(\mathrm{r}_\perp) = \frac{\kappa}{\mu}\log\left(\mathcal{F}^{-1}\left[\frac{\mathcal{F}\left[I(\mathrm{r}_\perp,z)\right]}{1+\left(\frac{\kappa\lambda}{4\pi}z\right)k_\perp^2}\right]\right),} \tag{3.47}$$

where $\kappa = 2\frac{\delta k}{\mu}$.

Bronnikov aided correction (BAC)

For non-homogeneous objects or objects endowed with high absorption capacity, it is indisputable that the phase reconstruction fails while using above algorithms. Hence the **Bronnikov aided correction (BAC)** [De Witte et al., 2009] is introduced, which is also based on the TIE. In this approximation, the intensity at the exit-plane is corrected and reads

$$I(\mathrm{r}_\perp, 0) = \frac{I(\mathrm{r}_\perp, z)}{1 - \frac{z}{k}\nabla_\perp^2 \phi(\mathrm{r}_\perp)}, \tag{3.48}$$

where the phase $\phi(\mathrm{r}_\perp)$ is initially calculated by using the MBA.
While the phase-retrieval procedures described above are governed by the transport of intensity equation for small varying propagation distances, reference was first made to the contrast transfer function to illustrate the contrast formation in all imaging regimes. Therefore, an overview of phase-retrieval algorithms based on the CTF and some application in single-distance PCI is reported later in section 7.4.

3.3.2 Derivation from the CTF

While the limitation of the TIE to small propagation distances is shown in Fig. 3.2, the CTF allows the use of multiple data recorded at short (near-field regime) or long propagation distances (holographic regime). It takes into consideration weak absorption and slowly varying phase shift, and enables quantitative phase retrieval from images acquired with hard X-rays [Cloetens et al., 1999]. The optimization of the phase retrieval combining several intensities that are collected at suitable Fresnel numbers along the optical axis was demonstrated to solve zero crossings of the PCTF [Zabler et al., 2005]. In regards to the single-distance PCI, phase-retrieval algorithms based on CTF methods are communicated (see Refs. [Gureyev et al., 2004, Turner et al., 2004, Bartels, 2013]). Treatments of pure phase and small absorption are distuinguishable.

Pure phase object

Considering a pure phase object, the absorption is neglected and Eq. 3.29 reads

$$\tilde{I}(\nu, z) \simeq \delta_D(\nu) + 2\tilde{\phi}(\pi\lambda z\nu^2)\sin\left[\pi\lambda z\nu^2\right]. \tag{3.49}$$

In order to achieve holographic phase reconstruction $\phi(\nu)$, a number N of intensities is acquired at different propagation distances z_m, m $\in$ [1, N]. Based on the least square minimization function definied as

$$S_c = \frac{1}{\mathrm{N}}\sum_{\mathrm{m}=1}^{\mathrm{N}} \int \mathrm{d}\nu \Big| \underbrace{\delta_D(\nu) + 2\tilde{\phi}(\pi\lambda z\nu^2)\sin\left[\pi\lambda z\nu^2\right]}_{\tilde{I}^{(\mathrm{approx})}(\nu, z_\mathrm{m})} - \tilde{I}^{(\mathrm{exp})}(\nu, z_\mathrm{m})\Big|^2, \tag{3.50}$$

where $\tilde{I}^{(\mathrm{exp})}(\nu, z_\mathrm{m})$ represents the measured intensities and the term $\tilde{I}^{(\mathrm{approx})}(\nu, z_\mathrm{m})$ indicates the intensities corresponding to $\tilde{\phi}(\nu)$, the minimum of the first derivative of this function

according to $\tilde{\phi}(\nu)$, i.e, $\frac{\partial S_c}{\partial \tilde{\phi}} = 0$ would give

$$\tilde{\phi}(\nu) = \frac{\sum_{\mathrm{m}=1}^{\mathrm{N}} \tilde{I}^{(\mathrm{exp})}(\nu, z_{\mathrm{m}}) \sin\left[\pi\lambda z\nu^2\right]}{\sum_{\mathrm{m}=1}^{\mathrm{N}} 2\sin^2\left[\pi\lambda z\nu^2\right]}. \tag{3.51}$$

As a result, the phase in real space reads

$$\phi(\mathrm{r}_\perp) = \mathcal{F}^{-1}\left[\frac{\sum_{\mathrm{m}=1}^{\mathrm{N}} \mathcal{F}\left[I^{(\mathrm{exp})}(\mathrm{r}_\perp, z_{\mathrm{m}})\right] \cdot \sin\left[\pi\lambda z_{\mathrm{m}} k_\perp^2\right]}{\sum_{\mathrm{m}=1}^{\mathrm{N}} 2\sin^2\left[\pi\lambda z_{\mathrm{m}} k_\perp^2\right]}\right]. \tag{3.52}$$

Adapted to the single distance, the phase retrieval from Eq. 3.52 is simplified to

$$\boxed{\phi(\mathrm{r}_\perp) = \mathcal{F}^{-1}\left[\frac{\mathcal{F}\left[I^{(\mathrm{exp})}(\mathrm{r}_\perp, z)\right]}{2\sin\left[\pi\lambda z k_\perp^2\right]}\right].} \tag{3.53}$$

By introducing the Born and Rytov approximations formulated in [Gureyev et al., 2004] respectively as

$$I^{(\mathrm{exp})}(\mathrm{r}_\perp, z) = \frac{1}{2}\left(\frac{I(\mathrm{r}_\perp, z)}{I_{\mathrm{out}}} - 1\right)$$

and

$$I^{(\mathrm{exp})}(\mathrm{r}_\perp, z) = \frac{1}{2}\log\left(\frac{I(\mathrm{r}_\perp, z)}{I_{\mathrm{out}}}\right),$$

where I_{out} is the projection acquired without object in the beam, the phase retrieval algorithms of Born and Rytov type for **pure phase objects** is obtained [Burvall et al., 2011]. Because the denominator in Eq. 3.53 can reach zero at $k_\perp = 0$, a regularization parameter $\alpha(k_\perp)$ can be added at the denominator [Gureyev et al., 2004, Bartels, 2013].

Weak-absorption restriction

By small and non-negligible absorption, the treatment of weak absorption with the assumption of homogeneity of the object can be done ($\mu \propto \delta$), and Eq. 3.29 is rewritten as

$$\tilde{I}(\nu, z) \simeq \delta_D(\nu) + 2\tilde{\phi}(\pi\lambda z\nu^2)\sin\left[\pi\lambda z\nu^2)\right] + 2\frac{\delta}{\beta}\tilde{\phi}(\pi\lambda z\nu^2)\cos\left[\pi\lambda z\nu^2)\right]. \tag{3.54}$$

As proceeded above for a pure phase object, the retrieval of the phase yields [Turner et al., 2004]

$$\phi(\mathrm{r}_\perp) = \mathcal{F}^{-1}\left[\frac{\sum_{\mathrm{m}=1}^{\mathrm{N}} \mathcal{F}\left[I^{(\exp)}(\mathrm{r}_\perp, z_\mathrm{m})\right] \cdot \left(\sin\left[\pi\lambda z_\mathrm{m} k_\perp^2\right] + \frac{\delta}{\beta}\cos\left[\pi\lambda z_\mathrm{m} k_\perp^2\right]\right)}{\sum_{\mathrm{m}=1}^{\mathrm{N}} 2\left(\sin\left[\pi\lambda z_\mathrm{m} k_\perp^2\right] + \frac{\delta}{\beta}\cos\left[\pi\lambda z_\mathrm{m} k_\perp^2\right]\right)^2}\right]. \tag{3.55}$$

The corresponding single distance formulation reads

$$\boxed{\phi(\mathrm{r}_\perp) = \mathcal{F}^{-1}\left[\frac{\mathcal{F}\left[I^{(\exp)}(\mathrm{r}_\perp, z)\right]}{2\left(\sin\left[\pi\lambda z_\mathrm{m} k_\perp^2\right] + \frac{\delta}{\beta}\cos\left[\pi\lambda z_\mathrm{m} k_\perp^2\right]\right)}\right],} \tag{3.56}$$

and with the Born and Rytov approximations made in section 3.3.2, leads to phase-retrieval algorithms for weak absorption derived in [Burvall et al., 2011]. The consideration of a non-zero regularization parameter $\alpha(k_\perp)$ at the denominator is still valid as reported by [Turner et al., 2004, Bartels, 2013].

Part II

Experimental setups

Chapter 4

v|tome|x s 240

In the recent past, high-resolution X-ray imaging (µCT) has gained ascendant interest for the analysis of the internal structure of samples which one would not like to damage mechanically, either because they are fragile and unique, or they just need to be non destructively checked. In laboratory-based µCT, the image quality depends essentially on the source extension and the detector performance. In this chapter the device mentioned is described according to the specifications by the manufacturer. Furthermore, knowledge of the performance of its components is a requisite for understanding the achievable resolution. To achieve this, the laboratory equipments are characterized and then, propagation-based phase-contract imaging is studied.

4.1 Description of the system and motivation

The advanced laboratory-based X-ray µCT device v|tome|x s 240 is a commercial product manufactured by General Electric (GE Sensing & Inspections Technologies GmbH, Wunstorf, Germany). The components described in the following are particular to this manufacturer.

Tube

The apparatus is equipped with two switchable X-ray sources: a microfocus and a nanofocus tube. A reflection target serves as anode in the microfocus tube and allows therefore loadable powers up to 320 W for a maximum voltage of 240 kV. A focal spot size of down to 7 µm is achievable with this tube, while it reaches 3 µm in the nanofocus tube [Singhal et al., 2013]. Latter is realizable due to its anode which is a transmission target. With reference to the description of a transmission tube in section 2.1.3, it is reasonable that the maximum acceleration voltage is 180 kV at 15 W. The radiation exit of both tubes are furnished with beryllium windows.

Detector

The detector installed in the apparatus is specified as DXR250CT [Purschke, 2005]. Like any flat panel detector (see section 2.2), it has a large active area of 1000 × 1000 pixels,

where each pixel holds a 200 µm square size. Its high dynamic range[1] (>10000:1) fosters rapid scan of objects of maximum 260 × 420 mm^2 in size[2].

Motivation

Given the characteristics mentioned above, the system benefits from the (800 mm) large focus-to-detector distance to geometrically magnify the samples onto the detector. Profit can be made of the high power delivered by the reflective target for imaging high-density samples, whereas the transmission target with relatively low voltage fits better to the imaging of small and low absorbing samples. The fact that the sources are **open X-ray tubes** – i.e., they can be opened for maintenance and replacement of items – increases the readiness of the setup for users. Combined with the cooling supplied to the components, the system's stability provides high-power and allows for high-resolution non destructive analysis of materials, composite and biomedical samples among many.

Nevertheless, the spatial resolution is eminently degraded with the high geometric magnification and especially the finite source size of the X-ray tube (see Figs. 2.1(b) and (c)). *Hence the image quality is compromised and requires the characterization of the components of the apparatus for understanding its performance.*

4.2 Characterization

It has been demonstrated in section 2.1.3 that the resolution achievable with high geometric magnification by a laboratory system primarily depends on the focal spot size of the X-ray tube. The spatial resolution is though viewed as a first factor of image quality, because it bears the response of the detector and the behaving of the source at a given geometric condition. As a consequence, the measurement of the focal spot size is by all means a separate process from the evaluation of the exact resolution at a specific geometric magnification. These inspection features are imaged at high magnification (20× to 100×) and subsequently, the geometric unsharpness is measured on the recorded image.

4.2.1 Focal spot size measurement

The measurement of effective focal spot sizes of X-ray tubes are regulated by the, say, European Standards Organisation (CEN) [Halmshaw, 2012]. Two of the CEN methods are dedicated to microfocus tubes. Either a small tungsten ball of 1 mm in diameter or a pair of crossed tungsten wires of the same diameter are used. An alternative for high-energy X-ray radiation is the use of a sharp and dense metal edge.

[1] The dynamic range is simply regarded as the depth of a signal that inherently influences the image quality.

[2] https://www.gemeasurement.com/inspection-ndt/radiography-and-computed-tomography/phoenix-vtomex-s (see data sheet - accessed: 2017-01-18).

4.2.2 Imaging resolution

A frequent way to assess the spatial resolution at some imaging settings is the use of image quality indicators (IQI) known as test patterns. In general, they are made of periodic features (lines or holes) of various widths. The resolution potential of the system is then determined by the size of the smallest distinguishable features. A demonstrated precise alternative [Samei et al., 1998, Bushberg and Boone, 2011] consists of using a sharp metal edge. By considering the image of this object at a specific magnification, the plot of the intensity profile through the direction perpendicular to the edge is defined as the **edge-spread-function** (ESF). A numerical differentiation of the ESF yields the **line-spread-function** (LSF), which is a one-dimensional function. The **point-spread-function** (PSF) of the system is rather a two-dimensional function (see Fig. 4.1(a)). In this geometrical conditions, the PSF and the LSF have the full width at half maximum in common (see chapter 3 in [Cloetens, 1999]). The LSF is a function of the standard deviation and is expressed as

$$LSF(x) = \frac{1}{\sigma\sqrt{2\pi}} \exp\left(\frac{-x^2}{2\sigma^2}\right). \tag{4.1}$$

At laboratory systems that operate in cone-beam geometry, some points must be considered.

- Due to the limited flux, an average of the ESF over the recorded image is desired.
- A fit of an error function (erf) is of interest to achieve symmetric LSF upon derivation.

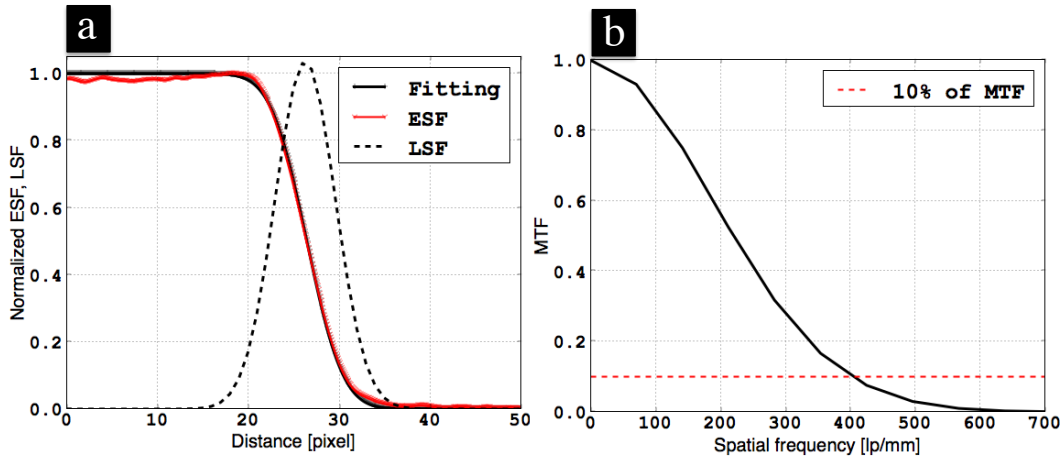

Figure 4.1: Procedure of resolution measurement using a sharp edge. (a) Line profiles are plotted perpendicular to the edge and averaged over a subregion to provide the edge spread function (ESF). The numerical differentiation of the fitting operated on the ESF gives the line spread function (LSF). (b) Modulation transfer function originating from the LSF. The red dashed line indicates the 10% of the modulation transfer function (MTF), that is required for the calculation of the resolution.

At high magnification ($M_{\text{geom}} \gg 1$), the drop of the ESF strongly reflects the blurring caused by the source according to Eq. 2.1, which is also viewed as the source extension if any

other origin of unsharpness is neglected. In this particular condition, the first steps of the measurement of the spatial resolution can be perceived as the evaluation of the focal spot size.

In the pursuit of the measurement of the resolution, the LSF is presented in reciprocal space as the **modulation-transfer-function** (MTF) given by

$$MTF(\nu) = \left|\mathcal{F}(\mathrm{LSF})\right| = \exp\left(-\frac{2\pi\nu^2\sigma^2}{2}\right), \tag{4.2}$$

with spatial frequency ν[lp/mm] (see Fig. 4.1(b)). The spatial resolution classically allies with the Nyquist frequency $\nu_{10\%}$ that corresponds to 10% of the MTF [Bushberg and Boone, 2011] and reads

$$\Delta \mathrm{r}_{\mathrm{res}} = \frac{1}{2\nu_{10\%}}. \tag{4.3}$$

Experimental

Ideally, the imaging resolution of the cone-beam setup can be estimated when the source spot size of the X-ray tube is known by using Eq. 2.1 and its extension to the spatial resolution developed in Appendix A.2. However, this dimension of the source spot for a specific acceleration voltage and current of the X-ray tube is usually unknown. Therefore, the opposite approach is required and the extent of the source spot can be estimated by measuring the MTF, hence deducing the resolution (see Eq. 4.3) and subsequently the source size from Eq. 8.5.

In Appendix A.2, the graph of the progression of the spatial resolution according to the geometric magnification has been demonstrated. Here in Fig. 4.2(a), this progression is plotted for three different source sizes and the magnification of the square region conveys in Fig. 4.2(b) that a certain geometric magnification is required to obtain a spatial resolution equal to the source size (see arrows). Moreover, this magnification would increase for smaller source areas and may be even unreachable in the geometry boundaries of the setup. Ultimately, the acquisition of projections of a knife edge at high magnification is recommended, where the difference between the measured spatial resolution and the calculated source size is extremely small.

4.3 Phase-contrast investigation and limitations

With the transmission tube of the facility adjusted on focus 1 (medium), the resolution has been measured at three different magnifications: 24.9, 49.9 and 99.9, using a 200 µm thick tungsten layer (see Fig. 4.3(a)). Due to the large source-to-detector distance of the facility, the resolution measurement at various magnifications is meant to provide conciseness in the estimation of the spot size. Projections consisted of an average of three images recorded each with an exposure time of 1000 ms.

The stars in the graph of Fig. 4.3(b) show as example the measured resolutions at 60 kV– following the procedure developed in section 4.2.2. For each measured resolution the spot size of the source was calculated out of Eq. 8.5. The progress of the spatial resolution at the

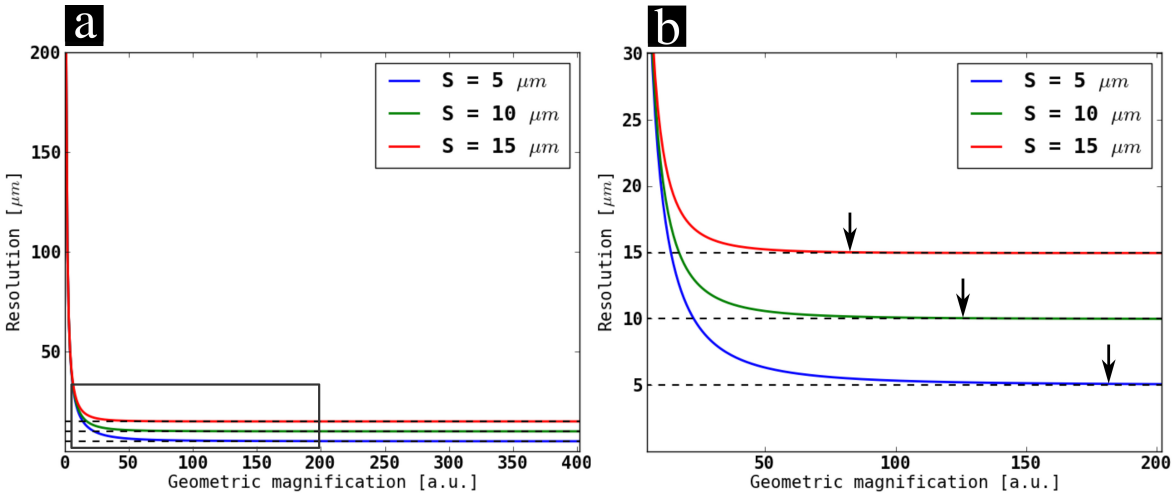

Figure 4.2: (a) Shape of the variation of the spatial resolution for selected source spot sizes (5, 10 and 15 µm) in v|tome|x s 240 as function of the geometric magnification. (b) Magnification of the square region in (a) showing that a higher geometric magnification is required in order to reach a spatial resolution as small as the source spot, when latter gets smaller.

selected currents (10 and 100 µA) confirms the reaching of an optimal resolution for a given source spot size. In order to estimate the source size, the highest magnification, where the spatial resolution remains lower than the calculated spot size has been considered. Using the selected spot size, the system's resolution function is fitted to the measured values as shown with solid curves in Fig. 4.3(b).

Though the measurements are obviously affected by imperfections (see e.g., M_{geom} = 49.9), the authenticity of the results remain valid, as the increase of the source spot with the current is satisfied at any of the three geometric magnifications. With the unexpectedly high spot size ($\approx$ 20 µm) obtained across the investigation above, the outcome is verified in Fig. 4.3(c). In this figure, periods of an Xradia pattern located below 20 µm are not resolved for a projection acquired with a 4.8 µm pixel size. As displayed in Table 4.1, a more general conclusion is drawn about the variation of the spatial resolution [Rueckel et al., 2014] and especially about the source spot extension, while applying various tube parameters.

Despite the inspection of the transmission tube, in the hope of a small source and accordingly a greater partial coherence of the beam, the investigation of the phase-contrast imaging as shown in Figs. 4.4(a) and (b) are rather dominated by the blurring. The study was operated at 60 kV and 10 µA for an exposure of 2000 ms on a cylindric phantom of 4 mm in diameter. The one half of the phantom is made of Polymethylmethacrylat (PMMA) and the second half of Teflon (C_2F_4). In Fig. 4.4(a), a projection of this sample is acquired for a pixel size of 8 µm corresponding to a magnification M_{geom} = 24.9. While it is difficult to observe the edge enhancement, it is conceivable that this effect is weaker in Fig. 4.4(b) collected for a pixel size of 4 µm, i.e., a larger magnification M_{geom} = 49.9 of the object on the detector.

According to the optimization of the resolution presented in the Appendix A.1, which could possibly intensify the effect of edge enhancement, the deconvolution was applied to correct the influence of the point spread function (PSF) on the measured images aforemen-

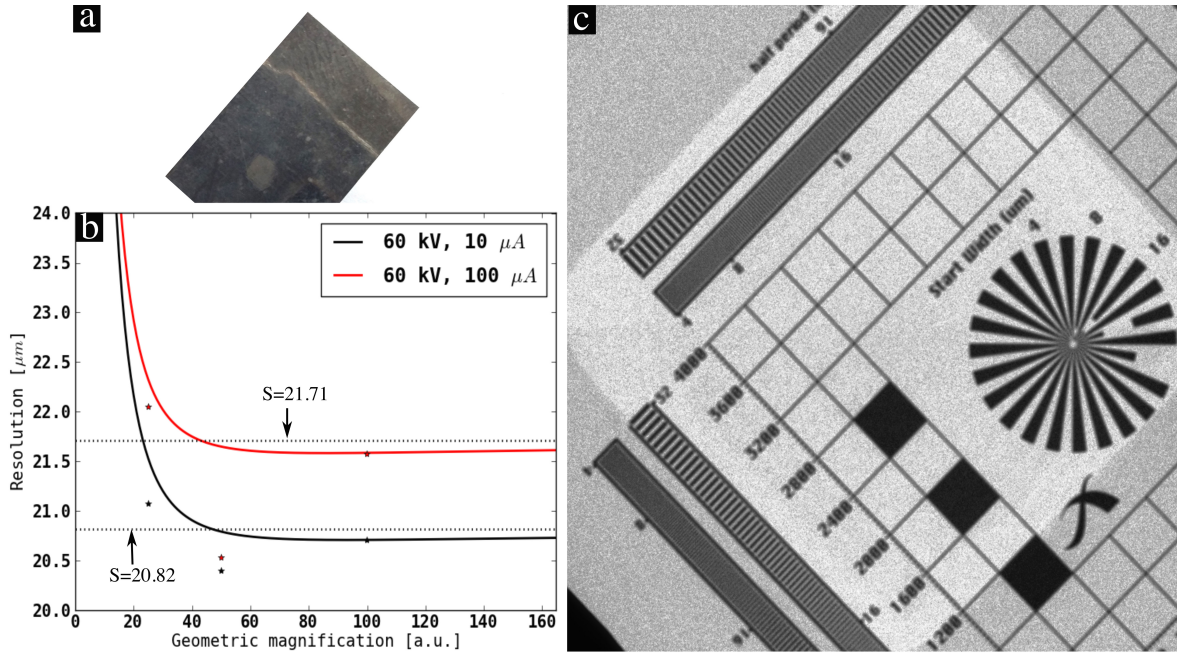

Figure 4.3: (a) Photograph of a 200 µm thick knife edge made of tungsten used in this inquiries. (b) Graph of the variation of the spatial resolution. The stars correspond to the measured values. The source size deduced from these measured values is used to fit the theoretical system's resolution plotted as solid curves. (c) Projection of an Xradia resolution pattern acquired at 60 kV and 10 µA with a pixel size of 4.8 µm. The resolving capability of the system is shown to lay significantly above 16 µm.

Voltage [kV]	Current [µA]	Magnification	Resolution [µm]	Spot size [µm]
60	10	24.9	20.71	20.82
		49.9	20.40	
		99.9	21.08	
	100	24.9	21.58	21.71
		49.9	20.53	
		99.9	22.05	
80	10	24.9	20.30	20.40
		49.9	19.29	
		99.9	21.76	
	100	24.9	20.89	21.00
		49.9	19.68	
		99.9	21.54	

Table 4.1: Summary of the measured resolution and the estimated spot size of the transmission tube for specific voltage and power settings. Measurements were performed at three different magnification to fit on the graph of the variation of the spatial resolution.

tioned. It was conducted in 15 iterations with $\sigma = 4$ pixels and a size of 20×20 pixels. This arbitrary choice is not necessarily the best, but visually conveys more contrast in Figs. 4.4(c) and (d) corresponding to Figs. 4.4(a) and (b), respectively. In addition, the graphs of Figs. 4.4(e) and (f) display profiles taken horizontally over an average of 50 pixels on output images (blue) and the ones corrected applying the deconvolution (red). Expression of edge enhance-

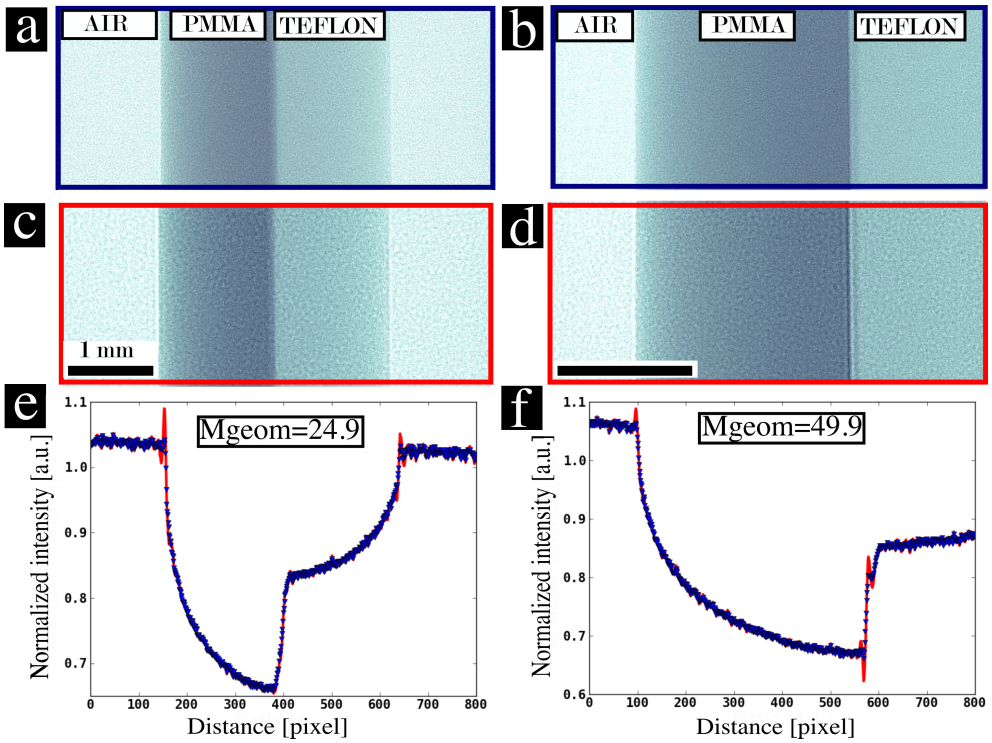

Figure 4.4: Effect of the deconvolution in phase-contrast imaging. (a) Projection image of a 4 mm thick cylindrical phantom acquired at 60 kV, 10 µA and with an exposure time of 2000 ms. This projection was measured with a geometric magnification M_{geom} = 24.9. One half of the phantom is made of Polymethylmethacrylat (PMMA) and the second half of Teflon (C_2F_4). (b) Image of a part of the phantom measured with M_{geom} = 49.9. (c)–(d) Images corresponding to the deconvolution of the figures in (a) and (b) using 15 iterations, σ = 4 pixels and a PSF size of 20 × 20 pixels. Horizontal line profiles averaged over 50 pixels in (a) and (c) are plotted in (e) with blue and red colors, respectively . Similar lines profiles in (b) and (d) are displayed in (f). Scale bar: 1 mm.

ment after deconvolution supports this alternative to consider phase-contrast imaging. For the X-ray tube and the detector are stationary, which would limit a more explicit consideration of this imaging technique, a thorough investigation is recommended in chapter. 5 where the relation between the phase contrast and the blurring will also be interpreted.

4.4 Summary

The expectation of demonstrating partial coherence, which is essential for PCI by studying the spot size of especially the transmission tube was not met. Nevertheless, the surprisingly wide source size achieved at the time of this evaluation explains the weak edge enhancement effect observed in the images. It has been also experienced that the deconvolution process is an approach to improve the spatial resolution and consequently the edge enhancement. Therefore, the study of this imaging technique is suggested to be performed in depth with

ZEISS Xradia 500 Versa, which is provided with motorized components.

Chapter 5

ZEISS Xradia 500 Versa

From conventional to synchrotron X-ray µCT, few factors that make important differences in image quality in setups are the beam flux, its brilliance and the imaging resolution. The first influences the statistics in the image and the acquisition time. The second concerns the possibility to filter some wavelengths so that a monochromatic beam is delivered, which allows for additional imaging methods. The third factor involves the detector sensitivity. These elements are relatively high at synchrotron facilities compared to conventional laboratory-based µCT setups. Filling the gap between both systems in a laboratory would request the achievement of some of these aspects, using advanced components in the setup. In this regard, the device dedicated in this chapter is described for the purpose of its construction as given by the manufacturer. This step precedes the motivation of studying this instrument for its applicability in high resolution range. After evaluation of the properties of the equipment, the single-distance propagation-based PCI is largely developed.

5.1 Description of the system and motivation

Tube

This equipment of the Versa family from ZEISS Xradia uses a maintenance free, sealed transmission tube. The transmission target of 5 µm tungsten is tied at the exit of the tube to a 250 µm thick diamond window. It operates in a voltage range between 30–160 kV and a power range from 2–10 W (see Table 5.1). The third essential criteria that characterizes an

Voltage [kV]	30	40	50	60	70	80	90	100	110–160
Power [W]	2	3	4	5	6	7	8	9	10

Table 5.1: Overview of the known operating ranges of the X-ray tube supplied in ZEISS Xradia 500 Versa. The limitation of the power applicable on the target at each voltage serves on one way, or another to maintain the sealed tube. A 10 W tops the power at voltages above 110 kV.

X-ray tube, apart form the voltage and the power is its focal spot. This varies according to the current but is overall stated to be less than 5 µm. With the contrast and the resolution

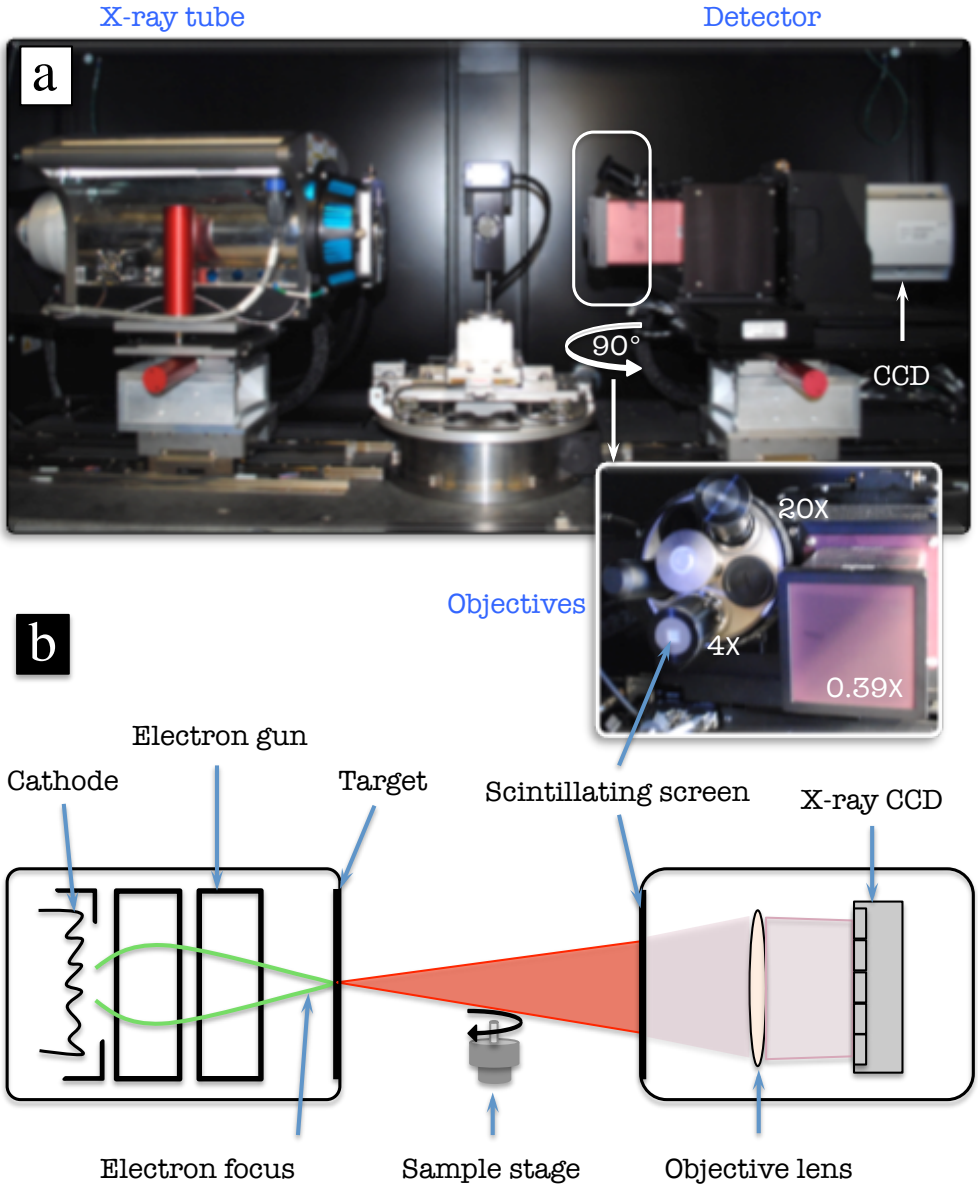

Figure 5.1: Overview inside the laboratory facility ZEISS Xradia 500 Versa. (a) A photograph shows the aligned elements of the setup, namely the transmissive X-ray tube, the automated sample stage and the lens-coupled detector system. The front side of the detector shows the three objectives (0.39×, 4× and 20×) furnished to the used device. (b) A schematic illustration of the working principle of the X-ray tube is shown on the left. On the right side, the details of the detector assembly are sketched. The scintillator screen stands at the front of the objective, whereas the lens sits inside the objective. Each objective automatically couples to the CCD camera when it is chosen for a measurement.

being determined by the source size, especially in X-ray microscopy, there is an overriding reason to investigate the source extension of the X-ray tube at various settings.

Detector

A patented lens-coupled detector system is used. As described in the second part of section 2.2, a fixed tube length is set out so that the objective would determine the resolution in the image if the geometric magnification in cone-beam geometry was not accounted (Fig. 5.1). The distinctiveness of this module resides in the fact that several objectives are provided and switchable based on the need. A 0.39× objective is used as demagnifying objective to fully investigate samples about 3–7 cm in dimension. The 4× and 20× objectives enable high-resolution measurements while magnifying the image on a CCD camera (Andor[1] iKon-L series [Andor, nd]) built of 2048×2048 pixels. With a pixel pitch of 13.5 µm, true spatial resolution down to 0.9 µm is achievable using flexible working distances. The maximum working distance between the source and the detector (scintillator screen) is around 495 mm.

Motivation

Within the general operating ranges summarized in Table 5.1, the transmission tube is ideal for two and three dimensional X-ray microscopy by covering a wide scope of sample exploration from soft or low-Z to high density materials. Beyond the fine source size managed by the power limitation, the lens-coupled detector allows, in combination with the flexible geometric magnification, a prominent spatial resolution. Needless to say, these attributes lead to advanced absorption X-ray imaging but also promote the feasibility of phase-contrast imaging of low-Z materials, where traditional / conventional computed tomography hits its limits. In order to evaluate the degree to which submicro resolution and phase-contrast imaging – initially deployed at synchrotron facilities – can be embedded into laboratories via this equipment, this chapter is dedicated to both the characterization of the apparatus and the inspection of the propagation-based phase-contrast imaging.

5.2 Characterization

5.2.1 Imaging resolution

The image quality indicator used in this section is built by the former Xradia Inc. and assembles various gold patterns on a rod as shown in Fig. 5.2(a). Two of them are star-shaped patterns indicated by label 1 and 2, that have been employed to identify the source size extension for different settings. Instead of estimating visually the resolution of the system from the smallest resolved feature, the method described in section 4.2.2 was preferred, that yields precise results. In Fig. 5.2(b), profiles perpendicular to the middle, horizontal and vertical bars enable the calculation of the spot extension and accordingly the resolution in each corresponding direction. Each line profile (red) was obtained as an average within a subregion (green frame). Given the degree of accuracy that is required for the alignment of the components of this system, the resolution indicator is placed as close as possible to the source and away from the detector, which was driven to its maximal spacing. Such an arrangement

[1] http://www.andor.com/pdfs/specifications/Andor_iKon-L_936_Specifications.pdf (accessed: 2017-01-18).

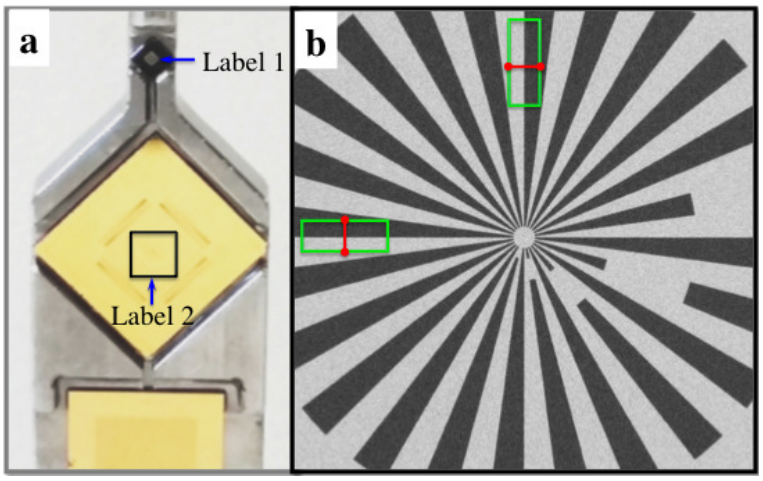

Figure 5.2: Image quality indicator built by Xradia Inc., and dedicated for high resolution measurements. (a) Photograph of the instrument . Fine structures down to 0.5 µm are incorporated in the star-shaped label 1. Label 2 contains features from 4 up to 23 µm. (b) Projection of the label 2 showing concentric features. The frames sketched horizontally and vertically are used to evaluate the source spot size in the vertical and horizontal directions, respectively.

---

could be achieved only with the 4× objective and distances z_1 = 12 mm and z_2 = 287 mm. Correspondingly, a ps_{eff}= 0.27 µm is yielded with the label 1. Considering the FWHM of the LSF as the extension of the source spot, Fig. 5.3(a) shows some values obtained in both x and y directions at 60 kV and 2 W set for the X-ray tube. Thus the shape of the source

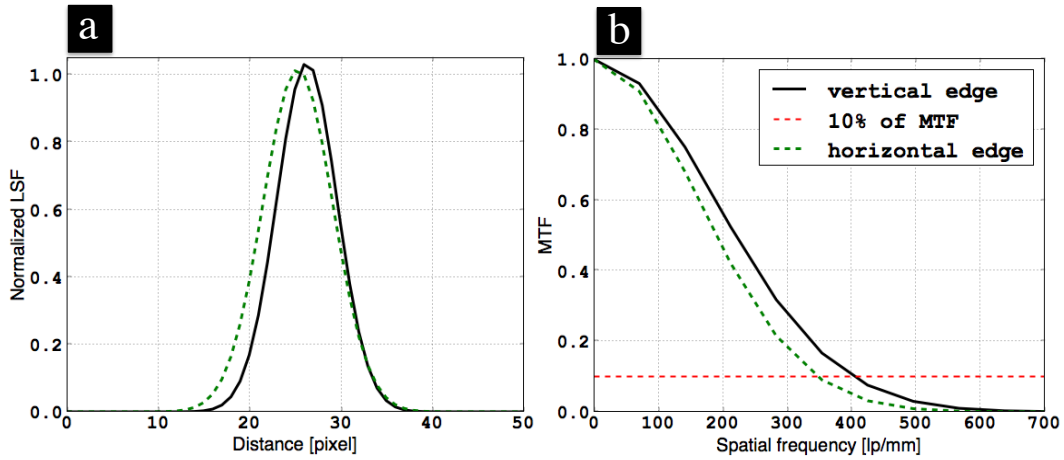

Figure 5.3: (a) Source spot size estimation by mean of the FWHM of the LSF. With a tube acceleration voltage of 60 kV and a power of 2 W, the FWHM is revealed asymmetric. (b) The MTFs corresponding to the LSFs displayed in (a) show a matching behavior. The larger FWHM results in a lower MTF value according to Eq. 4.2.

---

spot has been established with various parameters with mean of specific examples listed in

Table 5.2. Obviously, the spot size influences the system resolution at this geometric magnification (M_{geom} = 25) and the MTFs achieved as displayed in Fig. 5.3(b) could allow the calculation of the resolution using Eq. 4.3. The results of this procedure are summarized in Table 5.2. It is consistent to observe the increase of the source dimension with the power or rather the current for each acceleration voltage. Later the importance of this approach will be

Voltage [kV]	30	60		90		
Power [W]	2	2	5	2	5	8
FWHM [µm]	1.38	1.45	2.20	1.32	1.68	2.73
Resolution [µm]	0.9	0.82	1.17	0.80	0.89	1.56

Table 5.2: Summary of the spot size and the resolution detected for specific voltage and power settings.

reflected for example by way of the assessment of the transverse coherence (Eq. 3.39), which represents a determining factor in the occurrence of the Fresnel diffraction. An impression on the extension of the source according to the parameters applied to the tube is shown in Fig. 5.4. The ellipsoidal shape of the source spot that is elongated in the vertical direction for few parameters, is not of major concern since the horizontal extension of the spot defines the resolution in computed tomography. This spot is so far demonstrated to be smaller in the horizontal direction. Conversely, the PSF of the detector was calculated at its minimal

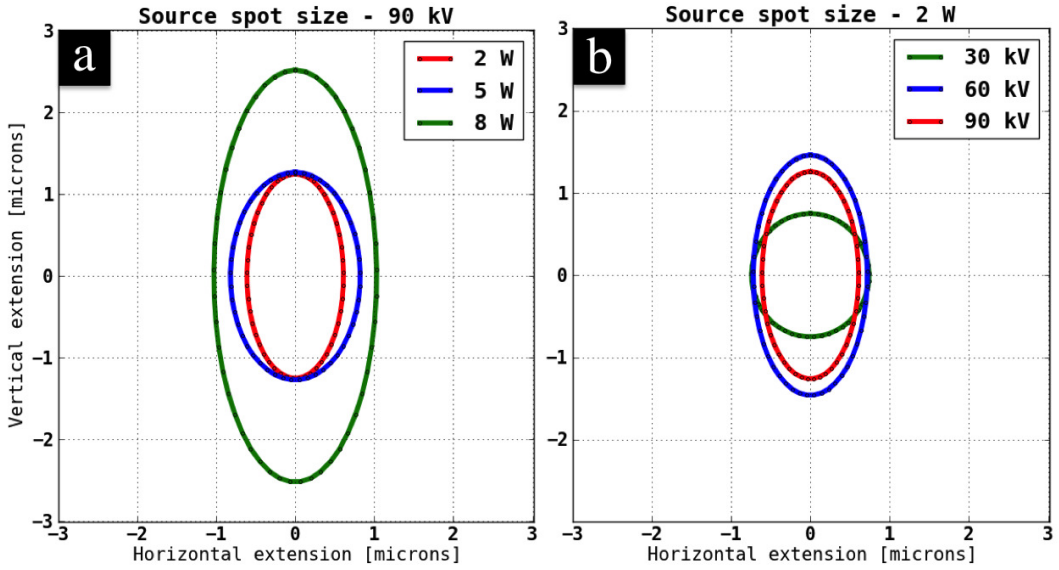

Figure 5.4: Illustration of the source spot extension according to the parameters defined in Table 5.2. (a) Broadening of the source spot in accordance with the increase of the current at a lone voltage of 90 kV. (b) Widening of the source for a fixed current and variable voltage.

spacing z_2 = 4.56 mm and a maximal spacing of the X-ray tube z_1 = 191.7 mm. Such settings were achieved with the 20× objective and meant to support neglecting the influence of the source spot on the system resolution. With a 2× binning of the detector CCD, label 2

of the imaging quality indicator was measured this time, achieving a ps_{eff} = 1.35 µm. The resulting resolution was equal to 2.19µm in each of the x and y directions at 60 kV and 5 W. Compared to a resolution of 1.9 µm in binning 1 that is obtained for the same parameters of the X-ray tube, the PSF procured by the 2× binning of the detector CCD was worse. Despite the awareness of this outcome, the 2-fold binning would be preferred since it is commonly used for quick measurements in the laboratory.

5.3 Phase-contrast investigation

Propagation-based phase-contrast imaging typically appeals to the improvement of the visibility of edges of small features in an image due to Fresnel fringes. In order to resolve smallest structures within a sample, it takes for granted that the investigation of this imaging at a setup might be performed at high resolution. From experience an effective pixel size of $\sim$ 1 µm can be certainly agreed in a cone-beam geometry, where the effective propagation distance is outright smaller than 1 m. For the purpose of this study, a significant physical value that is considerable is the fringe visibility also known as Michelson visibility which is written as

$$V = \frac{I_{\max} - I_{\min}}{I_{\max} + I_{\min}}. \tag{5.1}$$

The maximum and minimum intensities of the fringes are respectively indicated by $I_{\max}$ and $I_{\min}$.

5.3.1 Fundamentals

In this section, the term effective pixel size (ps_{eff}) is used instead of the resolution. Indeed, this value depends, at this setup, on both the geometric magnification (M_{geom}) and the optical magnification (M_{opt}) provided by the detector's objective. Given the size of the physical pixel (ps) of the CCD with a value of 13.5 µm, the ps_{eff} reads

$$ps_{\text{eff}} = \frac{ps}{M_{\text{geom}} \cdot M_{\text{opt}}} = \frac{ps}{(1 + \frac{z_2}{z_1}) \cdot M_{\text{opt}}} \tag{5.2}$$

It is appropriate to bring up the effective propagation distance

$$Z_{\text{eff}} = \frac{z_1 \times z_2}{z_1 + z_2} = \frac{z_2}{M_{\text{geom}}}, \tag{5.3}$$

as it will be required during the phase reconstruction step. This equation connotes that Z_{eff} is a function of the distance z_2 only if the M_{geom} is a constant, which is designated here by M_0. The condition is fulfilled while the ratio $\frac{z_2}{z_1}$ from Eq. 5.2 is constantly maintained. This requirement is generally not achievable through typical cone-beam geometry setups with fixed X-ray tubes and detectors. However, the motion provided to all the components of this setup solves this specification. It is thus expected that the object-to-detector distance

becomes function of the source-to-object distance is given by:

$$z_2 = z_1 \cdot \left(\frac{ps}{ps_{\text{eff}} \cdot M_{\text{opt}}} - 1 \right) = z_1 \cdot \left(\frac{M_0}{M_{\text{opt}}} - 1 \right). \tag{5.4}$$

With regard to Eqs. 5.3 and 5.4, it is suggested here to vary z_2 and consequently Z_{eff} for a constant ps_{eff} such as at a facility endowed with a parallel beam geometry.

Phantom When a CCD is illuminated, a number of charges (electrons) proportional to the light quanta are created. They are collected in chips and converted into an image at the end of the exposure time. Thus it is likely that the exposure time determines the noise level in an image. Decreasing this level even at low exposure times required a 2-fold binning that corresponds to a two-dimensional detector of 1024 × 1024 pixels. In order to estimate the

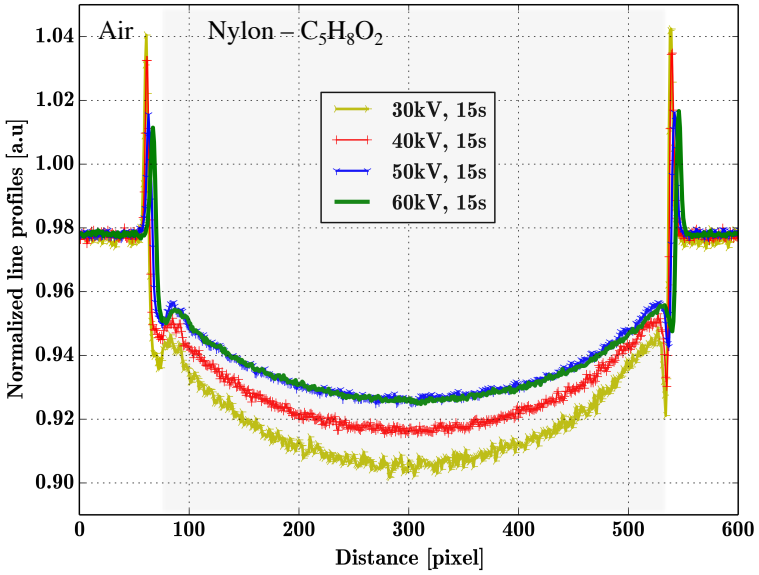

Figure 5.5: Course of fringes averaged over 200 pixels at the edge of an ≈ 350 µm thick nylon wire, which projections were acquired with an arbitrary exposure time of 15 s for various voltages. Using a 4× optical magnification and setting the specimen at z_1= 10 mm and z_2 = 80 mm yields a ps_{eff} = 0.75 µm. The height of the fringes denotes the quality of the diffraction according to voltage.

more valuable setting for the voltage, projections of a simple nylon wire of ≈350 µm in diameter were acquired at various voltages, but fixed exposure time (15 s) and propagation distance (z_1= 10 mm, z_2 = 80 mm). A pixel size value of 0.75 µm was achieved with the 4× objective of the detector (see Fig. 5.5). Despite the averaging of the line profiles over 200 pixels, they reveal the level of noise recorded at the selected voltages. Note that the highest power at each voltage was applied. Thus it is intelligible to observe better statistics at the highest voltage (60 kV, 5 W), however, the more qualitative fringes are obtained at 30 kV and 2 W. Hence, a compromise between high statistics and fringes should be determined for specific investigations. Source parameters of 40 kV and 3 W have been used in this work.

5.3.2 Feasibilities with various objectives: 0.39×, 4×, 20×

By choosing the **0.39× objective** and considering a $ps_{\text{eff}} = 1$ µm acquired with a 2× binned detector pixels i.e., $ps = 27$ µm, Eq. 5.4 reads

$$z_2 = z_1 \cdot \left(\frac{27}{1 \times 0.39} - 1 \right) = z_1 \times 68.23.$$

In view of the room left to avoid collision between the sample holder and the source, a minimal distance $z_1 = 10$ mm is used. It results in a value of $z_2 = 682$ mm that is sufficiently above the geometric allowance of the facility. The observation of fringes in the aforementioned settings is thereby subject to geometric limits. Moreover, the exposure time that may be requested during CT-acquisitions at large z_2 distances might be important.

With the **4× objective**, Eq. 5.4 turns to

$$z_2 = z_1 \cdot \left(\frac{27}{1 \times 4} - 1 \right) = z_1 \times 5.75.$$

The distance $z_1 = 10$ mm, implies $z_2 = 57.5$ mm, so that the ratio $\frac{z_2}{z_1}$ has a large range until the geometric limits of the instrument are reached at $z_1 = 192$ mm and $z_2 = 287$ mm. Here, the relation $z_2 \geq z_1$ applies.
The object-to-detector distance reads

$$z_2 = z_1 \times 0.35$$

at the highest optical magnification (**20**×) provided by the apparatus. Aside from the case $z_2 = z_1$, the investigation of phase contrast can be performed here in the so-called **inverse geometry**, where $z_2 < z_1$. A foreseeable limitation for such a settings is the collision range between the object and the detector, and hence a limited range conferred to the ratio $\frac{z_2}{z_1}$.

Experimental investigation

For the reasons expressed above, the modification of fringes at different propagation distances have been studied with the 4× objective. Projections of the sample were acquired with an acceleration voltage of 40 kV and a power of 3 W. Three main settings i, ii and iii are sketched in Fig. 5.6(a) and the corresponding parameters are listed in Table 5.3. There is clear evidence that the counts in the images would decrease with Z_{eff}, so that adequate exposure times are calculated at various distances according to the inverse square law (see [Halmshaw, 2012], chapter 6). Thus the exposure times were fixed correspondingly in Table 5.3. The choice of several intermediate distances would have been possible, but is not mandatory. Therefore, the chosen settings are representative of the behavior of the fringes on the entire geometry provided by the system.

According to the description of imaging regimes developed in section 3.2.4, the rise of fringes with the distance indubitably shows that the system performs in near-field regime above the contact regime [Gureyev et al., 2008], which is rather unreachable in divergent

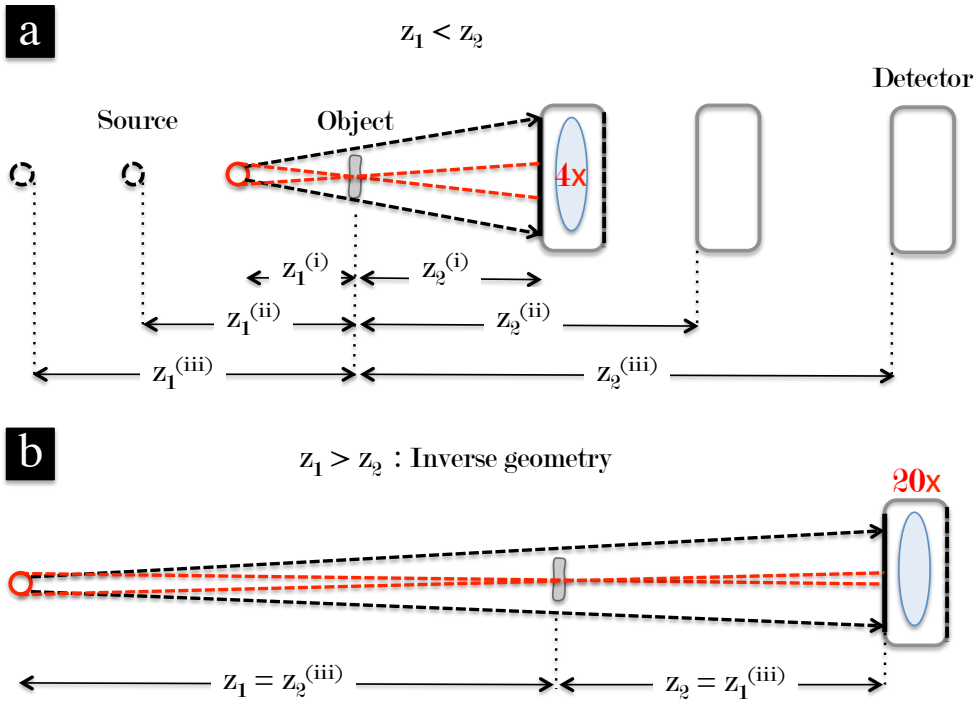

Figure 5.6: Scheme of the geometrical settings allowed by the facility. Not to scale. (a) While using the 4× objective of the detector, the achievement of pixel sizes down to less than 1 µm relies on the geometrical magnification, where $z_2 > z_1$. Hence a flexible range of geometrical settings is given. Three settings are illustrated with i, ii, iii where the ratio $\frac{z_2}{z_1} = 6$ is held constant. (b) The range of pixel size mentioned in (a) can be obtained with the 20× objective, even at $z_1 > z_2$. This represents the unique geometrical condition provided by the instrument, where the inverse geometry is accomplished at high resolution.

Code	z_1 [mm]	z_2 [mm]	Z_{eff} [mm]	ps_{eff} [µm]	exposure time [s]
i	10	60	8.5	0.96	5
ii	20	120	17.14	0.96	20
iii	40	240	34.28	0.96	80

Table 5.3: Resume of geometrical settings required to achieve various effective propagation distances while the ps_{eff} is held constant.

beam geometries. Propagation-based PCI is attributed the merit to considerably reduce the noise level in images when the phase retrieval is performed. This means that fringes could be observed with some extent of noise in an image. Thereby, Fig. 5.7 compares the evolution of fringes in images recorded for different and same (5 s) exposure times.

This figure illustrates the contrast formation with the distance, based on the visibility (Eq. 5.1). The proportional relation between Z_{eff} and z_2 for a constant M_{geom} (Eq. 5.3) provides a rationale for the similar trajectory of the graphs in Fig. 5.7(a) and (c), where the exposure times of the projections acquired are adjusted. Notwithstanding, the graphs from Fig. 5.7(b) and (d) show the ascent of fringes with Z_{eff} and z_2 at an equal exposure.

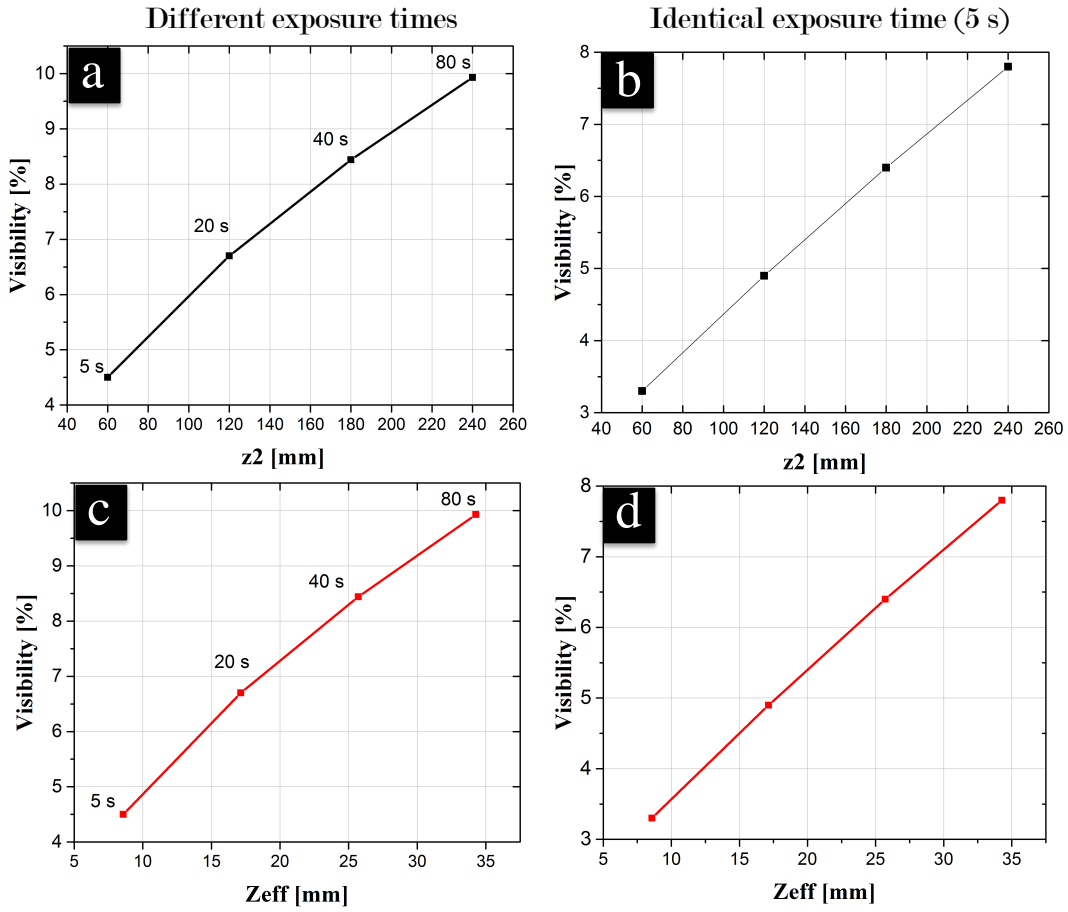

Figure 5.7: The visibility, chosen as indicator of the rise of fringes with Z_{eff} and z_2 is plotted. The graphs in (a) and (b) show the increase of the values according to z_2 for variable and identical (5 s) exposures, respectively. The graphs in (c) and (d) indicate similarities to (a) and (b), though visibilities are networked with respect to Z_{eff}.

While qualitative fringes are obtained at long distances Z_{eff}, long exposures may be required to accomplish excellent results in tomographic scan. As a drawback, scan times would be increased. The phase retrieval approach for even low scan time might solve this issue. This explains the illustration of the contrast with equal illumination of the phantom at variable Z_{eff}.

The use of the 20× objective allows of a $ps_{\text{eff}} = 0.675$ µm already at $z_1 = z_2$ as resumed in Table 5.4. Considering the enhancement of fringes with Z_{eff} in Fig. 5.8, which is similar to that of Fig. 5.7 regardless of the illumination, it is evident that the setup operates in the near-field regime for both the objectives (4× and 20×).

Interpretation of experiment and simulation

Experimental results of this procedure are plotted in Fig. 5.9(a). It is thus proved that in a cone beam the intensity of fringes increases with Z_{eff} for the same ps_{eff} attained in the image. Also, there is a widening of fringes perceived at the edges of the specimen. These observa-

z_1 [mm] = z_2 [mm]	Z_{eff} [mm]	exposure time [s]
10	5	5
20	10	20
40	20	80
80	40	350

Table 5.4: Resume of geometrical settings used to evaluate the evolution of visibilities according to Z_{eff} while using a 20× objective. Accordingly a constant $ps_{\text{eff}} = 0.675$ µm was achieved.

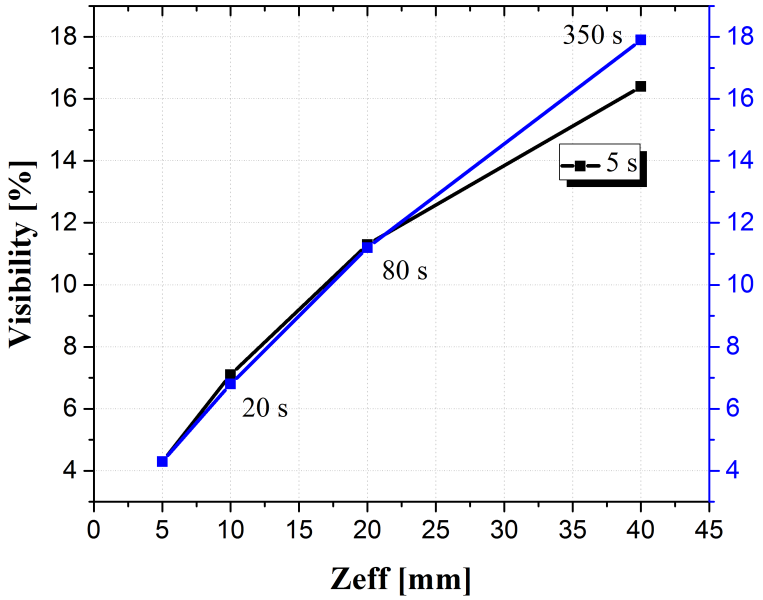

Figure 5.8: Graph of the changes evolved in fringes measured at radiographs recorded with constant (5 s) and variable exposure times at several Z_{eff}, considering a 20× objective. Given a $ps_{\text{eff}} = 0.675$ µm already at $z_1 = z_2$, this configuration was eligible for this experiment.

tions are perfectly reproduced by the simulation procedure (see Fig. 5.9(b)), that considers a cylindrical object of the same size and composition as the measured phantom. Given a plane wave to the simulated X-ray beam, the treated propagation distances are equivalent to the effective distances resulting from the scan parameters in cone-beam geometry. An energy of ≈ 13 keV reviewed as the average energy of the polychromatic spectrum of tungsten was adopted, correspondingly. The analysis of the experimental results compared to the simulated ones is performed in the section to come.

This section is dedicated for the explanation of the effects observed by measurement and simulation of the cylindrical object in Fig. 5.9. For this purpose, it alludes to the intensity fluctuation recorded on the detector, as function of the phase variations introduced by the object placed into the beam (Eq. 3.38). Let us bring up the fact that the wave-optical approach, which implies the Fresnel diffraction, has been adopted in the formalism of phase sensitive imaging in section. 3.2. However, another formalism might be pointed out, which uses the **ray-optical approach**, that rather involves the refraction for the description of in-

tensity variations in phase-contrast imaging, as reported in [Ishisaka et al., 2000, Peterzol et al., 2005, Wu and Liu, 2003]. No restriction is induced on the maximum phase shift coming from the object [Peterzol et al., 2005] and the ray-optical approach finds similarity to the wave-optical approach, despite the multiple postulations applied in latter: low image spatial resolution [Wu and Liu, 2003, Pavlov et al., 2004], low image spatial resolution and phase perturbations [Pogany et al., 1997], weak perturbation of the incident spherical wave [Gureyev and Wilkins, 1998]). Thus an universal formulation of the intensity registered at the detector, by considering the attenuation in the phantom can be written as

$$I(\mathrm{r}_\perp, Z_{\mathrm{eff}}, \lambda) \approx I^{(\mathrm{P})} \exp\Big(-2k\beta(\mathrm{r},\lambda)\Delta\mathrm{t}\Big)\left[1 - \frac{\lambda}{2\pi} Z_{\mathrm{eff}} \nabla^2 \phi(\mathrm{r}_\perp, \lambda)\right]. \tag{5.5}$$

As one might expect, there is a rise of intensity but also a minimal enlargement of the fringes. For a polychromatic spectrum, the fringe width would become more significant due to the multiple wavelengths of the spectrum [Boone, 2013, Kardjilov, 2003]. According to Eq. 5.5, it is well founded that the transmission varies with the spacing $Z_{\mathrm{eff}} = \frac{z_2}{M_{\mathrm{geom}}}$.

This results in variable transmission values through the phantom (blue-to-red marked line) simultaneously assessed in the experiment and the simulation. Since the description of the phase contrast by refraction was introduced here, it is possible to consider this effect as an edge blurring (EB) [Ishisaka et al., 2000]. With regard to the report of this author, the EB defined as

$$EB \cong a \cdot \{z_2 \lambda^2 (2x)^{1/2}\}^{2/3} + b \tag{5.6}$$

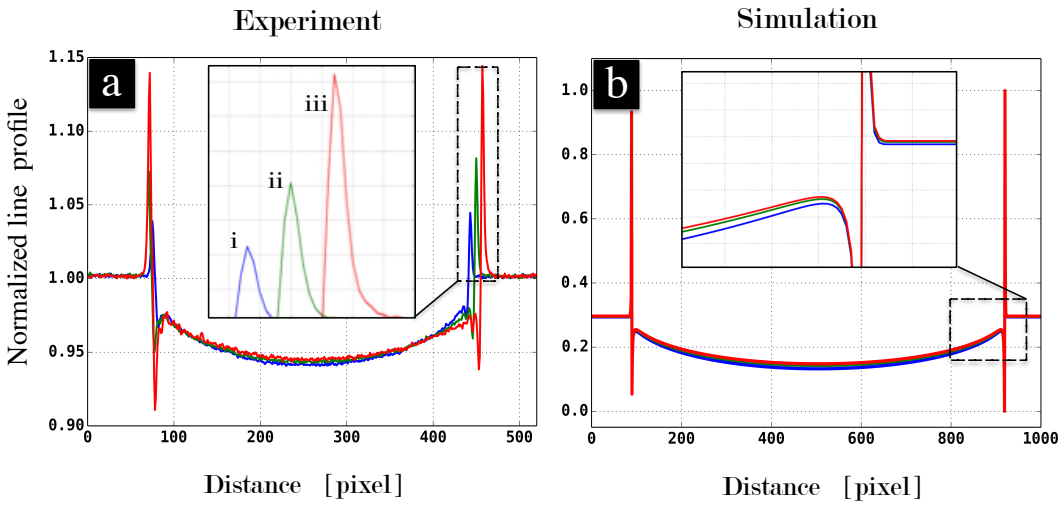

Figure 5.9: Course of fringes at the edge of cylindrical phantom of 1 mm in diameter. Experimental results of projections acquired at three distances as in Fig. 5.6(a). (a) The exposure times were 5 s, 20 s and 80 s, respectively, to compensate for the statistics when the distances increase. (b) Simulated results show equivalent behavior of the fringes as observed experimentally. It is noticed in both experimental and simulated results, that the curvature of fringes at the edges of the phantom broaden slightly with increasing propagation distance (see the frame zoomed in (b)).

depends on both z_2 and the wavelength λ of a monochromatic beam. The terms a and b take constant values when M_{geom} is fixed. The radius of the cylindrical object is designated by x. It is recognised that the width of EB varies slightly in the experiment as it depends on one hand on z_2 and implicitly Z_{eff}, and on the fact that several wavelengths contribute to the phase contrast on the other hand [Pogany et al., 1997]. As stated in this analysis, it is agreed that the blurring is involved in the formation of the contrast phase. If it should not be neglected, a deconvolution process correcting for the source extension may be desirable. Therefore, this process is addressed in Appendix A.1. Despite the fact that the ps_{eff} is the same and hence assumes the fringe profiles to be superimposed, an expansion is found in the experiment (see inset in Fig. 5.9(a), i–iii). A likely reason for this error is a non-alignment of the components of the system. In principle such a defect is of minor importance to a measurement made at a single distance, so for tomography or single-distance PCI.

By contrast, as the system architecture can acquire identical images at different Z_{eff}, the superposition of those would have been a first in a cone geometry system to perform a phase calculation based on the TIE in Eq. 3.33. In perspective, an estimate of this error that seems linear and a correction of the images could allow the calculation of the phase through the TIE at this setup.

5.3.3 Imaging in inverse geometry

Introduction

The influence of the source spot size at a setup using a divergent (cone) geometry has been already formulated in the introduction of this work (see section 2.1.3). A point source is noticed as ideal to improve the spatial resolution of the imaging system, but is extremely difficult to achieve, so that the lateral source dimension usually reduces the resolution expected while using a high geometric magnification i.e., $M_{\text{geom}} \gg 1$ (see Eq. 2.1). An alternative is to make use of the detector PSF by setting the geometric magnification to a low value ($M_{\text{geom}} \to 1$), if allowed by the system (compare Appendix A.2). Optimization of the spatial resolution by imaging in the so-called inverse geometry has been successfully performed with an in-house developed system [Bartels, 2013, Bartels et al., 2013]. Such an application at a commercial system requires though some investigation, hence this section reports the demonstration of the optimization of the spatial resolution in ZEISS Xradia 500 Versa, which offers simultaneously the high geometrical magnification and the inverse geometry settings (see Fig. 5.6).

Experimental procedure

For an effective pixel size $ps_{\text{eff}} = 1$ µm, the relation $\frac{z_2}{z_1} = 0.35$ is lower than unity and represents the so-called **inverse geometry** (see Fig. 5.6(b)). By holding this ratio constant, the increase of the effective propagation distance Z_{eff} is reversely warranted (Eq. 5.3) as listed in the Table 5.5. The visibilities calculated for such settings and those obtained at high magnification ($M_{\text{geom}} \gg 1$) with the 4× objective are plotted versus Z_{eff} in Fig. 5.10.

It is shown in this figure that the quality of the fringes is higher in the inverse geometry. This has been practically proven on a biological sample in [Bartels et al., 2013], where two independent setups were used. At the present setup though, the feasibility of the two

	4×				20×					
z_1 [mm]	20	30	40	50	57	67	77	87	107	127
z_2 [mm]	115	172.5	230	287.5	20	23.5	27	30.72	37.54	44.56
Z_{eff} [mm]	17.03	25.55	34.07	42.59	14.8	17.39	19.99	22.70	27.79	32.98

Table 5.5: Geometrical settings used to compare the evolution of fringes as function of Z_{eff}, by applying the 4× and the 20× objectives. The first provides settings at high magnification ($M_{\text{geom}} \gg 1$), whereas latter enables inverse geometry settings ($z_1 > z_2$). Images of the phantom were recorded at a pixel size $ps_{\text{eff}} = 1$ µm chosen to facilitate the comparison. An arbitrary exposure time of 10 s was applied in order to avoid much noise in the recorded images of the phantom.

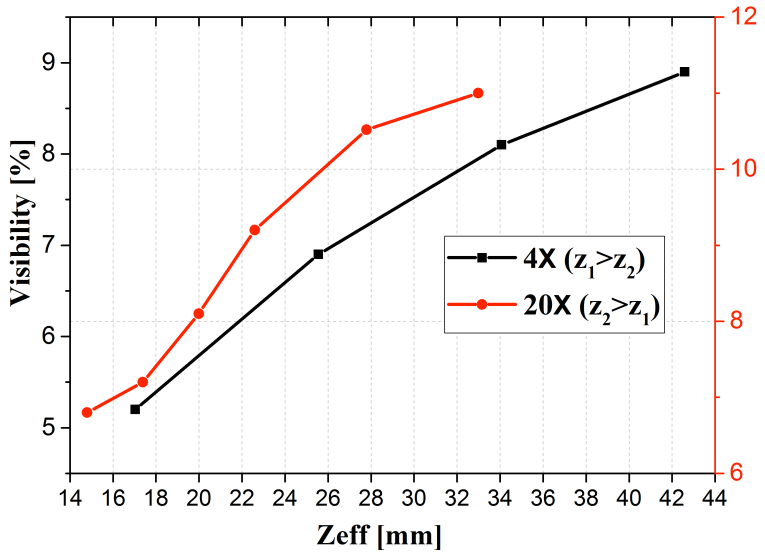

Figure 5.10: Graph showing the modification of fringes in the high magnification configuration (dark plot) as well as the inverse geometry design (red plot), according to the parameters reported in Table 5.5. The higher visibility values reached by latter indicate a prominent rise of fringe contrast in this geometry than high magnification settings.

geometrical settings at the same instrument is established thanks to the pair of magnifying objectives.

The setting i of the experiment I that was performed in section 5.3.2 is considered in the following because it allows us to obtain an equivalent inverse geometry configuration with the used device. It can be recalled that the source-to-sample and sample-to-detector distances were $z_1 = 10$ mm and $z_2 = 60$ mm, resulting in a geometric magnification $M_{\text{geom}} = 7$. An effective propagation distance Z_{eff} = 8.57 µm was achieved, whereas an effective pixel size ps_{eff} = 0.96 µm was reached with a 4× objective lens. If one would denote Z_{eff} and ps_{eff} as constant values C_1 and C_2, a corresponding setting in the inverse geometry ($z_2 < z_1$) would only be possible with the 20× objective lens (see Fig. 5.6). By reformulating Eqs. 5.2 and

5.3, the following linear equation system is formed:

$$\begin{cases} z_2 &= \frac{ps}{20 \cdot C_2} - 1 \\ z_2 &= \left(1 + \frac{z_2}{z_1}\right) \cdot C_1. \end{cases} \tag{5.7}$$

The physical pixel (ps) of the detector is still 2-fold binned and has a value of 27 µm. Based on Eq. 5.7, the distances z_1 and z_2 to retain in the inverse geometry for the given ps_{eff} and Z_{eff} are 30 and 12 mm, respectively.

Later in chapter 7, the application of both geometries in tomographic PCI are explored.

5.3.4 Flat object

Although the quality of the fringes was estimated by the visibility, the propagation-based PCI completes with the extraction of the phase and amplitude out of the mixed projections as introduced in [Paganin et al., 2002], and developed through several algorithms presented in section 3.3.1. From the conclusion made above, the near-field regime imputed to the imaging system allows to execute the phase retrieval algorithms based on the transport-of-intensity equation. It was deemed appropriate to adopt the single material algorithm where the object is considered homogeneous and of uniform thickness (Eq. 3.46). Since this algorithm reproduces the thickness of the specimen, this choice gives the possibility to compare the results of the algorithm to the true measurable thickness of the sample. Hence the use of a flat object made of teflon (C_2F_4). The following results are communicated in [Bidola et al., 2015b].

Two experiments are reported in this section. They are designated as experiment I and II. The first is conducted with regard to the scheme of Fig. 5.6(a) and the spacing parameters of Table 5.3, where M_{geom} = 7. With reference to Eq. 2.1, the standard deviation of the system is reduced to $\sigma_{\text{sys}} \approx 0.73 \times \sigma_{\text{src}}$. While these geometric settings are enabled by the motion awarded to the components of the setup, they are not obvious at a conventional laboratory facilities where only the sample stage shifts along the beam direction. Therefore, experiment II deals with the case of a fixed source-to-object spacing z_1 in order to estimate the enhancement of the fringe contrast as function of the effective propagation distance.

To minimize the resolution limitation through the finite source size, a compromise was found between low source size and high fringe contrast (Fig. 5.5). Thus the compact source settings (40 kV, 3 W), resulting in a FWHM = 1.8 µm were admitted to be optimal for this study and later in real phase-contrast measurements of weak absorbing objects with this device. Also, holding M_{geom} constant in experiment I may prevent a significant variation of the blurring at various propagation distances. Given a source size of 1.8 µm, the minimal transversal coherence provided by the beam for phase-contrast imaging is calculated conformally to Eq. 3.39 and according to the spacings in Table 5.3 as l_c = 0.52 µm [Wilkins et al., 1996, Cloetens, 1999].

Spectrum and energy optimization

Phase-contrast imaging with polychromatic compact sources is realisable thanks to the fact that the contrast in these images can be considered wavelength independent [Pogany et al.,

1997, Nesterets et al., 2005]. However, the retrieval of the phase from the recorded phase-contrast images requires an unique wavelength λ if the Paganin's algorithm is adopted. Hence, a spectral weighted average of the source spectrum measured for 40 kV tube voltage was calculated as:

$$E_{\mathrm{av}} = \frac{\int E\Phi(E)dE}{\int \Phi(E)dE}. \tag{5.8}$$

Here, $\Phi(E)$ represents the photon fluence and E each energy value of the spectrum. The spectrum of the transmission tube containing a tungsten anode was measured (see Fig. 5.11) using an energy sensitive X-123 Amptek spectrometer (AMETEK, Inc.).The detected histogram was corrected for the absorption in the 500 µm silicon path to the Amptek detector, giving E_{av}= 13.05 keV. According to [Nesterets et al., 2005], a wavelength spread $\Delta\lambda$ around the effective one is eligible to achieve optimal phase-contrast. In the following, we will retrieve the phase from from the measured data for 6 different X-ray energies around E_{av}. These energies are given by the CXRO x-ray database [Henke et al., 1993] depending on the properties of the phantom.

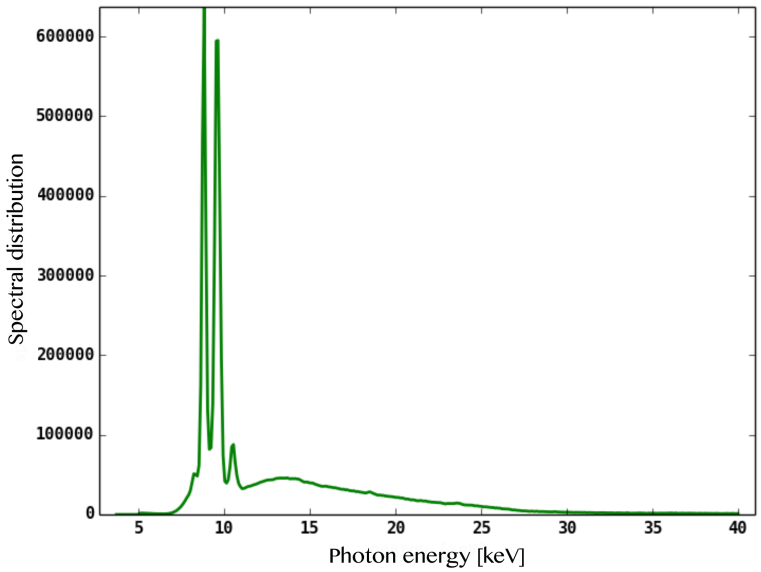

Figure 5.11: Spectrum of the beam for the tungsten target measured at 40 kV tube voltage with an energy sensitive X-123 AMPTEK spectrometer. The beam was corrected for the 500 µm silicon path to the detector.

The phantoms used in both experiments were a low absorbing Teflon layers (C_2F_4) with a density of 2.2 $\mathrm{g/cm^3}$. The projections of the samples were corrected for flats (projections taken without any sample in the beam).

The image quality is evaluated with the signal-to-noise ratio (SNR), calculated as [Diemoz et al., 2012]

$$SNR_{\mathrm{area}} = \frac{\sqrt{A}(I_{\mathrm{obj}} - I_{\mathrm{back}})}{\sqrt{std^2(I_{\mathrm{obj}}) + std^2(I_{\mathrm{back}})}} \simeq \frac{\sqrt{A}(I_{\mathrm{obj}} - I_{\mathrm{back}})}{\sqrt{I_{\mathrm{obj}} + I_{\mathrm{back}}}}. \tag{5.9}$$

Position	visibility [%]	SNR$_{area}$ projection [10^{-05}]	SNR$_{area}$ phase [10^{-04}]
i	31.78	1.72	7.77
ii	45.07	1.68	7.62
iii	49.68	1.66	7.45

Table 5.6: Propagation distances and calculated parameters used to evaluate the quality of the images. The magnification is constant and implies a unique ps_{eff} = 0.964 µm

The mean intensity values in a given area A of the object as well as its background are $I_{\text{obj}} = \frac{N_{\text{obj}}}{A}$ and $I_{\text{back}} = \frac{N_{\text{back}}}{A}$, respectively, where N_{obj} and N_{back} depict the number of counts on the detector in these regions. The quantities $std(I_{\text{obj}})$ and $std(I_{\text{back}})$ stand for the standard deviations of I_{obj} and I_{back}. The variables I_{min} and I_{max} are the minimum and maximum intensities of the averaged intensity profile within the area A. The results are reported in Table 5.6. Although Eq. 5.9 assumes a 100% efficiency of the detector, which is a non stringent condition, the SNR_{area} is considered here as a suitable parameter to express the quality of phase-contrast images because they were recorded with almost the same photon flux.

Position	z_1 [mm]	z_2 [mm]	Z_{eff} [mm]	ps_{eff} [µm]
iv	10	20	6.66	2.25
v	10	30	7.5	1.687
vi	10	60	8.57	0.964

Table 5.7: Propagation distances and calculated parameters used to evaluate the quality of the images for variable magnifications.

Images of a 500 µm thick phantom were acquired according to experiment I (described in Fig. 5.6), analyzed and plotted in Fig. 5.12. The phase-contrast images of the three positions in this experiment are shown in Figs. 5.12(a)–5.12(c), respectively. The mean line profile throughout 200 pixels in each image were plotted and shown in Figs. 5.12(d)–5.12(f). The visibility (see Table 5.6), which also represents the magnitude of the phase-contrast increases with the propagation distance Z_{eff}, while the SNR decreases, because the exposure time was unchanged [Gureyev and Wilkins, 1998]. As the changes of the visibility in the phase-contrast images only are not sufficient to conclude about the quality of the data, the thickness of the phantom was plotted for various energies around the average energy of the X-ray beam (13.09 keV, 14.03 keV, 15.03 keV, 16.11 keV and 17.26 keV) (see Figs. 5.12(g)–5.12(i)). The δ and β values corresponding to these selected energies were computed for a density of 2.2 g/cm^3 from the CXRO X-ray database [Henke et al., 1993]. The plots of the thickness is used to interpret the quantitative correctness of the retrieved phases. Energy values close to the calculated average (13.09 and 14.02 keV) yield a thickness value close to the exact thickness of the phantom. Therefore, using 13.09 keV as effective energy is a good approximation for quantitative phase-contrast imaging. However, the effect of blurring induced by the source could affect the retrieved phases. This is observed in the regions

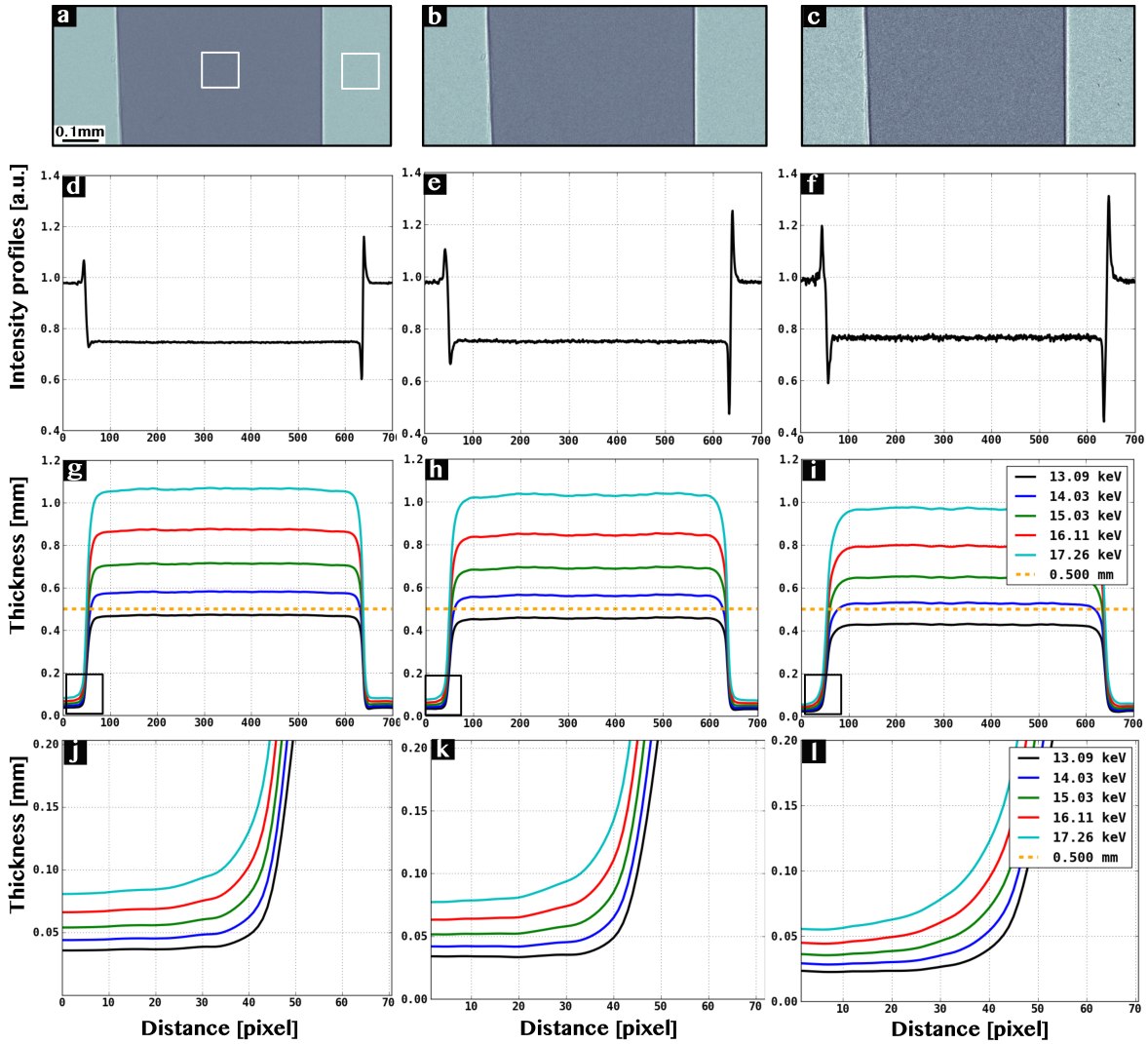

Figure 5.12: Panels (a)–(c) are single projections of a 500 µm thick Teflon phantom (C_2F_4) which were recorded with an exposure time of 5 s. The areas framed in (a) are used for the calculation of the signal-to-noise ratio (SNR) in each image. Panels (d)–(f) are the intensity profiles of the phantom, recorded at the given distances in Table 1, respectively, showing an increase of the edge enhancement. Panels (g)–(i) depict the thicknesses of the phantom calculated for different energies using Eq. 3.46. The orange broken lines show the correct thickness of the phantom. The edges of the phantom (in the rectangle box in (g)–(i)) are magnified to j, k and l, respectively. These serve for qualitative interpretation of the image.

of Figs. 5.12(g)–5.12(i) marked by rectangles and magnified in Figs. 5.12(j)–5.12(l). The plots in these figures shows an opening with the effective propagation distance Z_{eff}, even though the magnification is maintained. Hence, the most qualitative image of experiment I is obtained at position I.

The second experiment was performed at a fixed source-to-sample distance z_1 = 10 mm. A 250 µm thick phantom was studied by changing the sample-to-detector distance. An in-

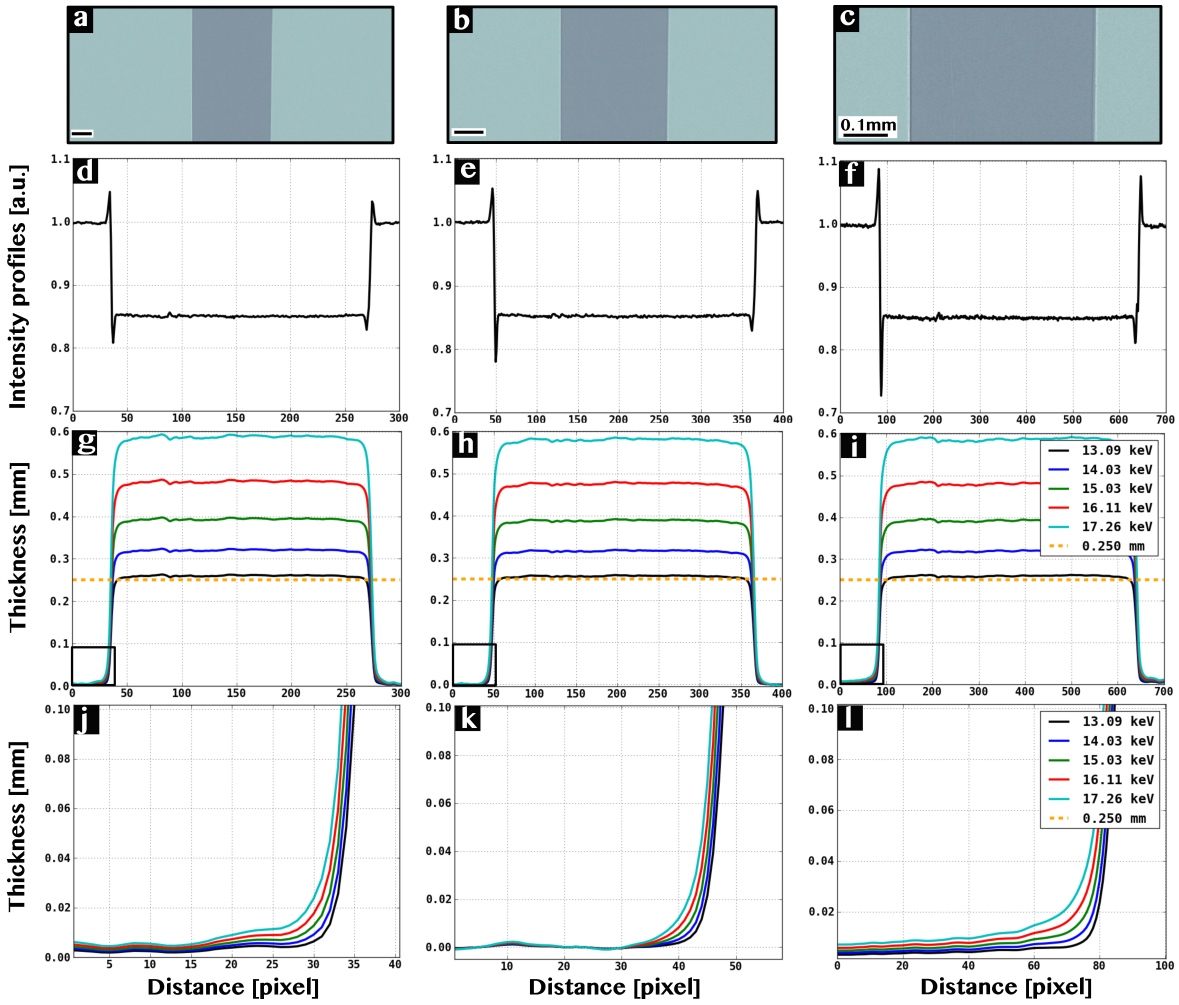

Figure 5.13: Panels (a)–(c) are projections of a 250 µm thick Teflon phantom, recorded with an exposure time of 5 s at a source-to-sample distance z_1 = 10 mm and various sample-to-detector distances z_2=20, 30 and 60 mm. Panels (d)–(f) are the respective intensity profiles of (a)–(c). A correction for the magnification was applied to make the plots comparable. The calculated thicknesses according to Eq. 3.46 are plotted for various energies in (g)–(i). The broken orange line correspond to the correct thickness of the phantom. The course of the plots surrounded by the boxes in (g)–(i) is magnified in (j)–(l), respectively.

crease of the visibility with the distance in the phase-contrast images was noticed at the edges of the phantom (see Figs. 5.13(a)–5.13(c)). These images were corrected for the magnification to allow comparable plots, which are shown in Figs. 5.13(d)–5.13(f). The results in Figs. 5.13(g)–5.13(i) confirm that an energy of 13.06 keV yields the most accurate phase retrieved. The magnification of the rectangles in Figs. 5.13(g)–5.13(i) shows in Figs. 5.13(j)–5.13(l) a small but still existing opening of the curves compared to Figs. 5.12(j)–5.12(l). This result can be understood with the following explanations, considering the functions $Z_{\mathrm{eff}}^{\mathrm{experimentI}}$ equivalent to Eq. 5.3 and

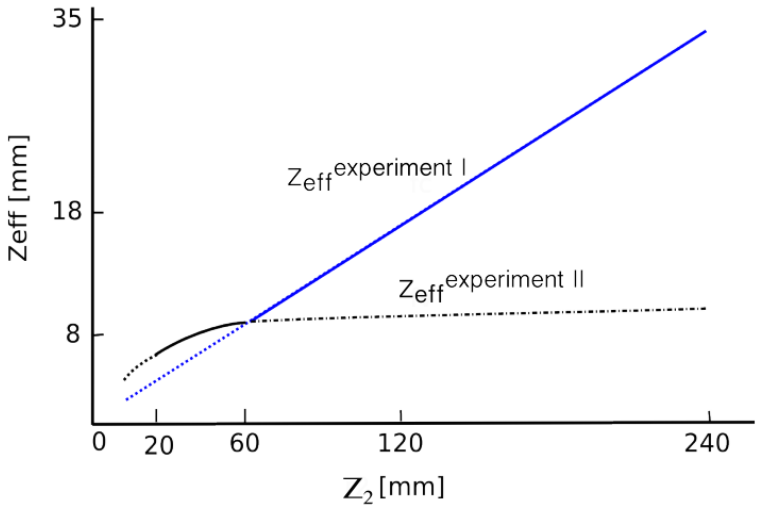

Figure 5.14: Variation of the effective propagation distance Z_{eff} with the sample-to-detector distance z_2, for a constant (blue) and variable (dark) magnification. Solid lines indicated the values resumed in Table 5.6 and Table 5.7. Dashed lines show the real course of the functions $Z_{\text{eff}}^{\text{experimentI}}$ equivalent to Eq. 5.3 and $Z_{\text{eff}}^{\text{experimentII}}$.

$$Z_{\text{eff}}^{\text{experimentII}} = \frac{1}{\frac{1}{z_1} + \frac{1}{z_2}} = \frac{1}{\text{const} + \frac{1}{z_2}}, \tag{5.10}$$

where $Z_{\text{eff}}^{\text{experimentII}}(z_2)$ represents here the variability of Z_{eff} as function of z_2 for variable magnification. The term $\frac{1}{z_1} = \text{const}$ expresses that this quotient is constant. The graph in Fig. 5.14 shows (in blue) the function $Z_{\text{eff}}^{\text{experimentI}}(z_2)$, which represents the growth of the propagation distance with z_2, when z_1 could also increase. The function $Z_{\text{eff}}^{\text{experimentII}}$ in (dark) shows a weak increase of the propagation distance with z_2, while z_1 is constant. The behavior of these functions is believed to affect the visibility and justifies the results in Figs 5.12 and 5.13. Thus, the quality of the phase-contrast images primarily depends on the propagation distance Z_{eff}. The little variation of this distance in experiment II, therefore, was not favorable to observe significant improvements in the phase-contrast images. It follows that the study of the phase-contrast in a cone-beam geometry, like here, requires the possibility to simultaneously change the distances z_1 and z_2.

In fact, the effective pixel size of 0.964 µm obtained in experiment I corresponds to a spatial resolution up to $u \approx 1.03 \times 10^6$ m^{-1}. When a source size of 1.8 µm are taken into account (Eq. 2.1), u is estimated to be $\approx 7.5 \times 10^5$ m^{-1}. However, the spatial frequencies $u = (2\lambda Z_{\text{eff}})^{-1/2}$ yielding the maximum of the CTF for the effective propagation distances in Table 1 are 7.8×10^5, 5.56×10^5 and 3.93×10^5 m^{-1}, for $\lambda = 0.95 \times 10^{-10}$ m (E = 13.09 keV). The maximum of the CTF at position I of experiment II is the closest to the point spread function of the system. Qualitatively, this explains the achievement of the best image quality at position I. In experiment II, the optimal phase contrast is not observed in the image with the lower magnification, where the spacing value $d \approx \frac{1}{u} = 1.12$ µm is much lower than the effective pixel size at the image position. This fulfils the assertion by Pogany

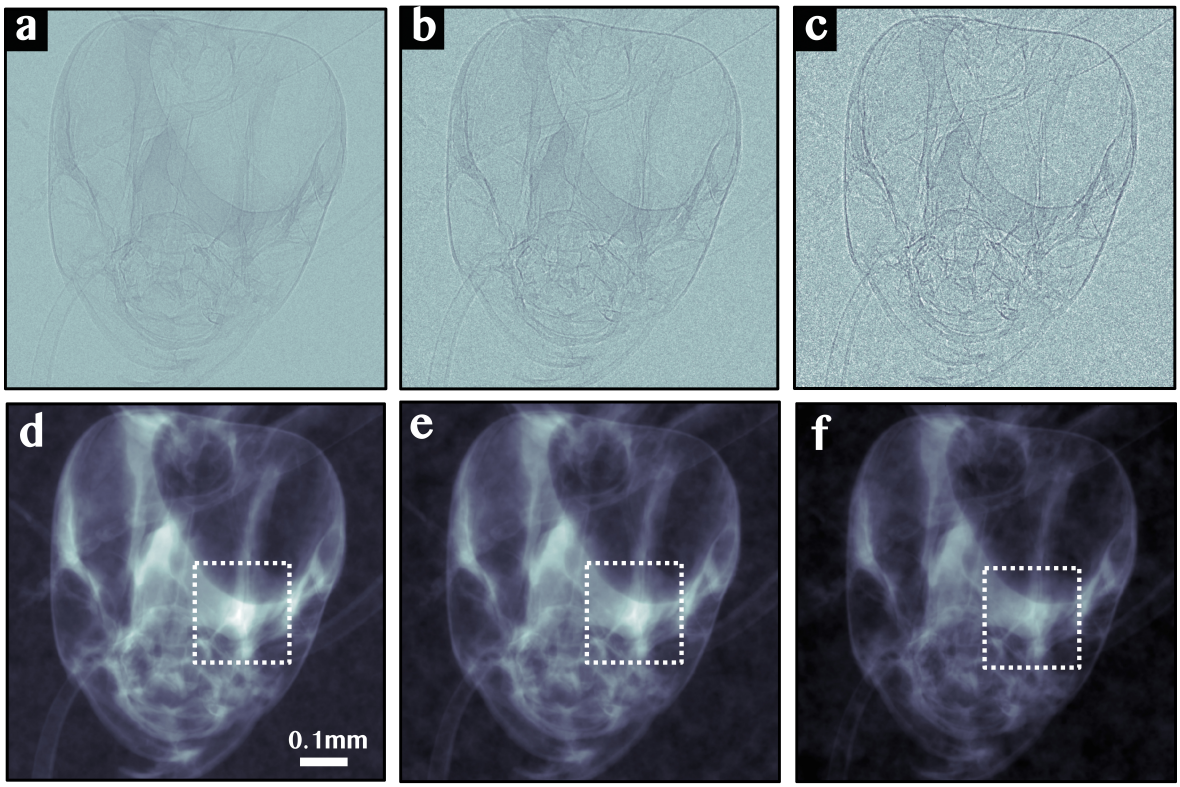

Figure 5.15: Images of an ant head projections (a)–(c) were taken with 5 s exposure time at the three variable distances in Fig. 5.6. Panels (d)–(f) are their respective phases. The selected square regions in each phase image provide a proof that the contrast differs with the effective propagation distance.

---

et al. [Pogany et al., 1997].

In opposition to experiment I, the slight difference of Z_{eff} over the three positions in experiment II explains the weak blurring induced by the filtering during the phase retrieval. In summary, the filtering that occurs with the phase reconstruction is shown to increase with the effective propagation distance Z_{eff} or z_1, which could however be mitigated by a sharpening filter as performed in [Nugent et al., 1996].

5.3.5 Real object

According to the results obtained above, the recipe conditions of experiment I were chosen to image a substantial and representative sample: a head of an ant. The choice of this sample was based on the positive experiences to investigating phase-contrast on specimens made of chitin[Tuohimaa et al., 2007]. The projection images of the sample at the various distances Z_{eff} are shown in Figs. 5.15(a)–5.15(c). Their respective phases are shown on the second row, where the noise is remarkably reduced. The phases were calculated for chitin $(C_8H_{13}O_5N)_n$ with δ = 1.77e-06 and β=1.63e-09 computed for an energy of 13.09 keV and a density of 1.38 $\mathrm{g/cm^3}$. The regions marked in Fig. 5.15(d) show a slightly different contrast to those

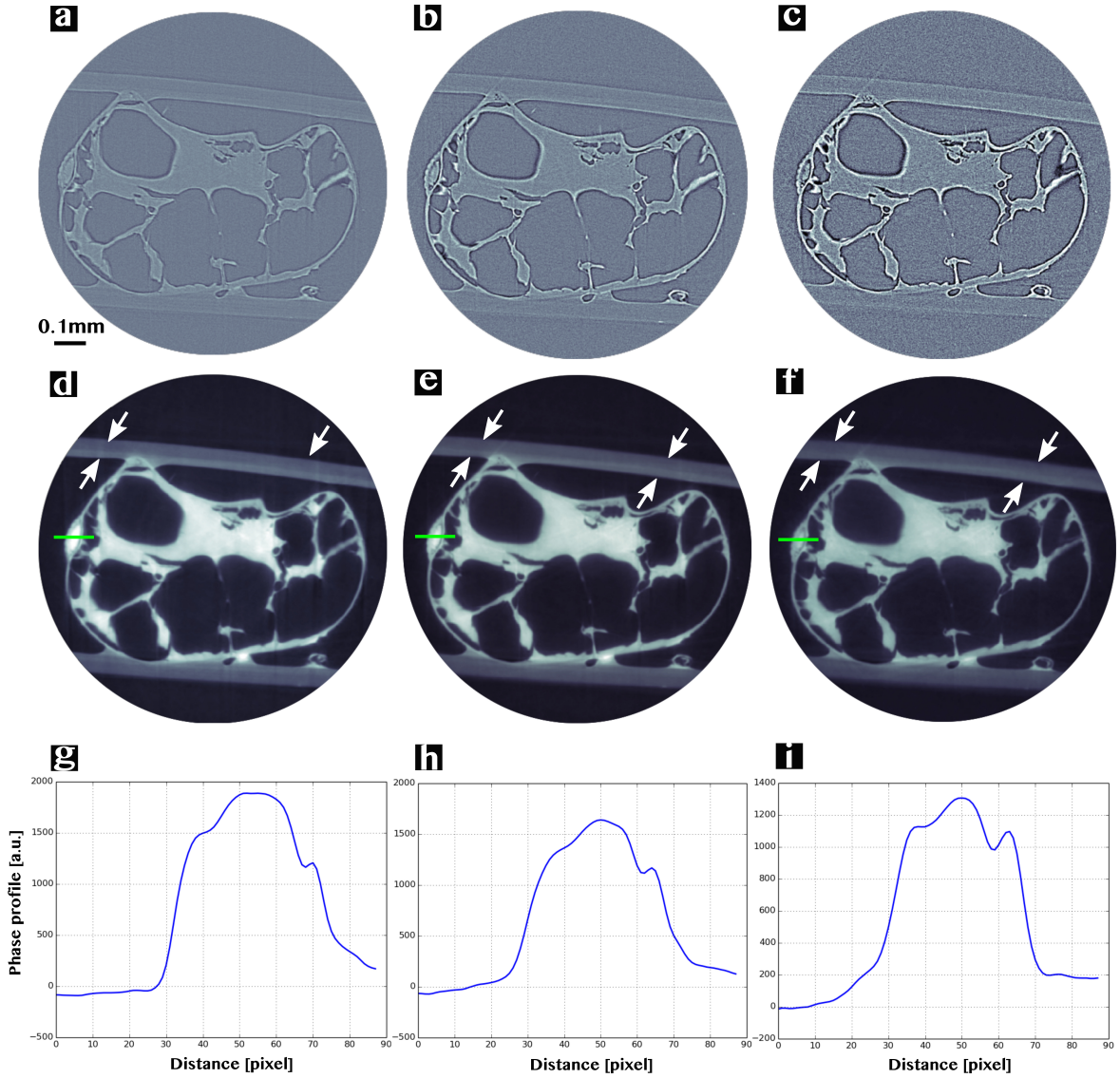

Figure 5.16: Panels (a)–(c) Tomograms of the ant recorded with 5 s exposure time at the three variable distances in Fig. 5.6. Panels (d)–(f) are the corresponding slices from the reconstructed phases. Profiles along the green solid lines in (d)–(f) are plotted in (g)–(i), respectively. The contrast is obviously accurate in (d) as shown by the plot, but also the arrows in (d)–(f) indicate some contrast variabilities in these images, along the tape (made of plastic and glue) used to fix the sample.

in (e) and (f). This is an evidence of the variability of the contrast in retrieved phases with the distance for any investigated object. The tomography of the ant's head at positions i, ii and iii, with the same effective pixel size (0.964 µm) was performed, acquiring 1600 projections for each scan with an exposure time of 5 s per projection. Figs. 5.16(a)–5.16(c) are the reconstructed tomograms using the standard filtered backprojection algorithm. The phases of the projections were calculated as in Eq. 3.43 and reconstructed using the filtered backprojection. The reconstructed slices of these phases, which correspond to the tomograms

in the first row are shown in Figs. 5.16(d)–5.16(f), respectively. The increase of noise with the distance in the normal tomograms is obvious. The reconstructed slices of the phases give a better contrast, besides the decrease of noise. A simple way to compare the reconstructed phases is to plot a line in a selected region made of various structures (see green line in Figs. 5.16(d)–5.16(f)). Their respective profiles are shown in Figs. 5.16(g)–5.16(i), and illustrate the contrast in that selected region. Once again, the optimal defocusing distance, where high contrast has been obtained corresponds to the smallest sample-to-object distance z_1 (see values in Fig. 5.16(g)).

5.3.6 Geometric boundaries

Provided that the contrast transfer function lies in the direct phase regime, the Fresnel number from Eq. 3.30 satisfies the relationship $F \geq 1$. It follows

$$Z_{\text{eff}} \leq \frac{\Delta \mathbf{r}_{\perp}^2}{\lambda}. \tag{5.11}$$

Considering that the sample thickness is much smaller than the effective propagation distance i.e., $\Delta t \ll Z_{\text{eff}}$ [Weitkamp et al., 2011] Eq. 3.21 that determines the samples thickness for the Fresnel diffraction to take place is established as well.
Let's consider a critical effective propagation distance $Z_{\text{eff,c}}$, which is sufficient for the argumentation of the geometric boundaries. Here, the resolution is meant to be two times the effective pixel size of the detector [Weitkamp et al., 2011]

$$Z_{\text{eff,c}} = \frac{(2 \cdot ps_{\text{eff}})^2}{\lambda}. \tag{5.12}$$

With the average energy of 13.05 keV obtained from the spectrum measure at 40 kV, a wavelength $\lambda = 0.91$ Å is calculated. Evidently, the graph in Fig. 5.17 reflects a quadratic course of the function $Z_{\text{eff,c}}(ps_{\text{eff}})$. Within the range of propagation distance accounted in experiment I (see Table 5.3), the spacing z_2 draws close to the geometric boundaries of the setup for $Z_{\text{eff,c}}$= 34.28 mm[2]. The side length of the field of view that may display the measurable object size by binning 2 is defined as

$$FOV = \underbrace{1024}_{\text{Number of pixels}} \times ps_{\text{eff}}, \tag{5.13}$$

which is ~ 1 mm in this specific case. Reversely, in order to measure entirely an object of thickness $\Delta t \simeq 3$ mm in the near field regime at the setup, a $ps_{\text{eff}} \approx 2.9$ µm is required and corresponds to a $Z_{\text{eff}} \approx 396$ mm that is far above the geometric boundaries of the setup. Hence, the restricted propagation distance Z_{eff} enables the phase-contrast imaging of objects which size remain in a range smaller than a couple of millimeters. However, this is actually the scope of performance of a microscope and proves that the X-ray microscope is accommodated for phase-contrast imaging.

[2]The definition of $Z_{\text{eff,c}}$ is considered as sufficient since its value could even get higher for a true resolution, which might exceed two time the ps_{eff} according to Fig. 5.17

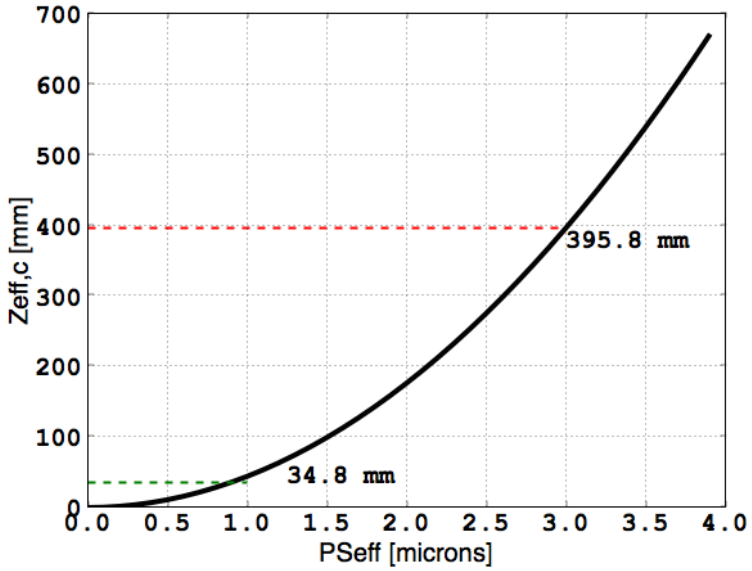

Figure 5.17: variation of the effective propagation distance Z_{eff} in accordance with the effective pixel size ps_{eff}. Depending on the geometric boundaries z_1 and z_2 of the system, the ps_{eff} achievable and the corresponding FOV can be evaluated, where the phase-contrast imaging is executable.

5.4 Summary

Studying the geometry, source and detector resolution of the X-ray imaging device ZEISS Xradia 500 Versa enabled us to find the optimal conditions for phase-contrast imaging with, subsequently, phase reconstruction. With some comparison to previous studies at X-ray microscopes [Pogany et al., 1997], the influence of the magnification (z_2=z_1) and the effective propagation distance Z_{eff} (implicitly z_1) on the quality of the retrieved phase has been experimentally verified. While maintaining the magnification, it has been experimentally demonstrated with a simple realistic object (Teflon - C_2F_4) that the phase contrast is optimized at low source-to-object distance (z_1). These results have been clearly observed by using a representative object (ant), where a net contrast in the reconstructed phase was achieved. This unprecedented experimental study with ZEISS Xradia 500 Versa has the importance to reveal the performance of the machine in terms of phase-contrast imaging. Ultimately, it is shown in practice that fast phase-contrast imaging is optimally applicable on real low absorbing objects, and yields high quality phase images in this laboratory device. Despite the choice of only a mean wavelength value λ from the source spectrum and the one-material non-stringent assumption of the phase retrieval used in this work, it can be agreed that the results obtained quantitatively (thicknesses) worked perfectly. However, the correct quantification could deviate, if λ is not chosen properly. Apart from the fact that: (1) the imaging system resolution is limited by the finite source size, and (2) reaching high contrast is limited by z_1 (geometry), this study shows optimal application of phase-contrast imaging in radiography and tomography on low absorbing real objects in this commercial device.

Part III

Applications

Chapter 6

Microscopic computed tomography

In this chapter, some pertinent investigations at medium and microscopic resolution using the X-ray systems outlined in this work are featured. It is shown that the association of µCT with a few techniques can enable the execution of various inquiries. As example, µCT combined with methods to improve the contrast such as the staining of biological tissues and the dual-energy CT are demonstrated.

6.1 Introduction

Recent introduction of micro-computed tomography from medium to high resolution in laboratories helped to relieve synchrotron facilities and allowed pertinent solutions in different fields. Not long ago, state of the art and upcoming technologies available on the market for industrial applications of computed tomography were surveyed [De Chiffre et al., 2014], while their aptitude in meteorology was also reported [Kruth et al., 2011]. By means of µCT, the study of ancient insect species fossilized in amber allowed to report on the global distribution of today's related species [Penney et al., 2012], or facilitated taxonomic equivalence between specimen of different era [Dunlop et al., 2011]. With case studies of sample fossilized in the sediment such as the Ediacaran specimen *Corumbella werneri*, µCT enabled the recovery of the morphology of the fossil [Bidola et al., 2015a] and coupled with its skeletonization the taxonomic ranking was completed [Pacheco et al., 2015].

Imaging of soft tissues at true microscopic resolution employing fixation along with staining have been demonstrated [Shearer et al., 2014] and a periodical overview of the status of the technology could introduce in the developments and applications of µCT in biomedicine [Ritman, 2004, Ritman, 2011]. Compared to high flux facilities, studies elaborated in X-ray laboratory apparatuses need longer scan times, but they are in return easier to access, they generate less expenses, and experience a substantial development towards higher resolution, as well as imaging techniques (e.g., dual-energy CT). For both devices stated in this work, this chapter illustrates the capabilities of µCT through outstanding case studies.

6.2 Preclinical studies: stained lungs

6.2.1 Motivation

The characterization of individual genes related to the genesis and growth of tumors is a critical prerequisite to provide rational targets for future anti-cancer therapy. In order to assess the relevance of certain genes for tumor development or maintenance, gene-targeted mouse models deficient of certain genes or harboring specifically modified gene sequences are largely used in preclinical lung cancer studies. The tumor volume is often used as a measure for the impact of the respective gene on carcinogenesis in experimental mice and is an important parameter in cancer research. Thus, here we present an approach for volumetric quantification of tumor volume in ex-vivo stained mouse lungs imaged with high-resolution micro-computed tomography (μCT). We selected an appropriate staining protocol for mouse lungs among those available in literature and we have investigated four tumor-burdened lungs using it. The high-contrast images of stained tumorous lungs obtained by μCT allowed us to segment the tumors and make an overall quantification of the total volume of unhealthy tissue areas in each diseased lung. Our results revealed that the combination of staining and μCT is an effective strategy to obtain valuable information of unhealthy tissue in genetically engineered mouse models that, in combination with histopathological studies, may be beneficial to preclinical lung cancer research.

Merits of the inquiries

Lung cancer incidence has been particularly harmful since the 21^{st} century [Jemal et al., 2011, Siegel et al., 2013]. A significant number of cases (41 %) are diagnosed at an advanced stage, where surgical resection is not recommended and, consequently, survival rates are low [CDC, nd]. Finding novel therapies that will help a wider range of patients is critical for improving overall survival rates, thus strategies using drugs designed to prevent tumor initiation and progression are being clinically developed [Sotgia et al., 2011, Kasinski and Slack, 2012]. Over the years, researchers have benefited enormously from genetically engineered mouse models for lung cancer, as they mimic the pathophysiology of human cancers, providing a deep understanding of the steps involved in the progression of the disease [Cheon and Orsulic, 2011, Kelly-Spratt et al., 2008, Haines et al., 2009]. Precise quantification of the tumor volume is fundamental in genetic and molecular studies of the lung carcinogenesis with experimental mice [Cheon and Orsulic, 2011, Fushiki et al., 2009, Kirsch et al., 2010] and this requires an imaging modality capable of representing the pulmonary architecture down to the level of individual alveoli in three-dimensions (3D). Histopathology is a well-established approach used in the clinics for the examination and diagnosis of cancer type in diseased lung tissues. The specimens are cut into thin slices and stained, and the images obtained afterwards display high-contrast and high-resolution in two-dimensions (2D). Ideally, the digitization of several 2D histological sections would provide a 3D histopathological image of the entire specimen and would allow the quantification of tumor volume. However, 3D reconstruction of an entire volume from histology data presents drawbacks mostly related to tissue deformation inherently induced during the flow of the sample preparation process [e Silva et al., 2015, Amunts et al., 2013, Stille et al., 2013, Alic et al., 2011, Dauguet et al.,

2007]. Very recently, staining of soft-tissue samples combined with X-ray absorption micro-computed tomography has been demonstrated to be a beneficial tool for imaging biological specimens [Alanentalo et al., 2008, de Crespigny et al., 2008, Metscher, 2009a, Ribi et al., 2008, Weninger et al., 2006]. Hence, in this work we explored staining and μCT to visualize and quantify the volume of tumors in genetically engineered mouse models of pulmonary cancer. After performing tests with some common staining agents on lungs of wild-type mice, we selected the most appropriate staining protocol for this organ and proceeded with further investigations of the tumor-burdened counterparts. Three-dimensional segmentation of the reconstructed data of the scanned tumor-burdened lungs was operated using a semi-automated method to determine the ratio of tumor volume to the total of lung tissue volume. We discuss the advantages and limitations of our method of tumor bulk evaluation by applying it to a total of four diseased specimens and by comparing it to the well-established histopathological analysis of hematoxylin and eosin-stained (H&E) diseased tissues.

Methods

Contrast agents For our experiments, we adopted the contrast agent staining protocols presented in ref. [Metscher, 2009a]. Three solutions were used: (1) phosphotungstic acid in water (PTA); (2) a mixture of iodine (I2) and potassium iodide (KI) in water (named as IKI); and (3) iodine dissolved in absolute ethanol (I2E).

Sample preparation Prior to the main experiment, four non-tumorous lungs stained with different contrast agents were analyzed to determine the best contrast medium for this study. The size of the lungs ranged between 1.2 and 1.3 cm in diameter (Fig. 6.1). In a preliminary preparation, the lungs were inflated via tracheal incision preceding the closure of the trachea by a surgical suture. They were fixed in 4 % paraformaldehyde (PFA) and subsequently placed in 70 % ethanol in order to shrink the lungs to a stable size [Hsia et al., 2010]. The staining was executed by placing each lung in one of the following contrast agent solutions for 14 h: PTA, IKI or I2E. One lung used as control was not stained and was solely set in 70 % of ethanol. Afterwards, the lungs were washed and fixed in a tube filled with ethanol 70 %. The investigation of tumorous lungs was performed on specimens taken from mice after 19 weeks of tumor induction. At an age of six to eight weeks, the mice are infected intranasally with a Cre-expressing adenovirus, which results in the Cre-mediated excision of a gene from its genetic recombination site called “STOP cassette.” This allows the tissue-specific genetic expression of the formerly silent K-RasG12D gene, a pro-proliferative gene carrying the G12D-mutation to turn it into a tumor-driver [Jacks et al., 1994]. As this gene is often mutated in humans, this is not only a well-established mouse model, but also a good representation of the disease in humans. In addition to possessing the driving mutation, the mice used in our imaging experiments could further be divided into Mcl-$1^{+/+}$, Mcl-$1^{fl/+}$ and Mcl-$1^{fl/fl}$ genotypes [Jackson et al., 2001, Opferman et al., 2003]. By the same mechanism, the Cre-enzyme leads to the removal and thus deficiency of one or both alleles of this gene.

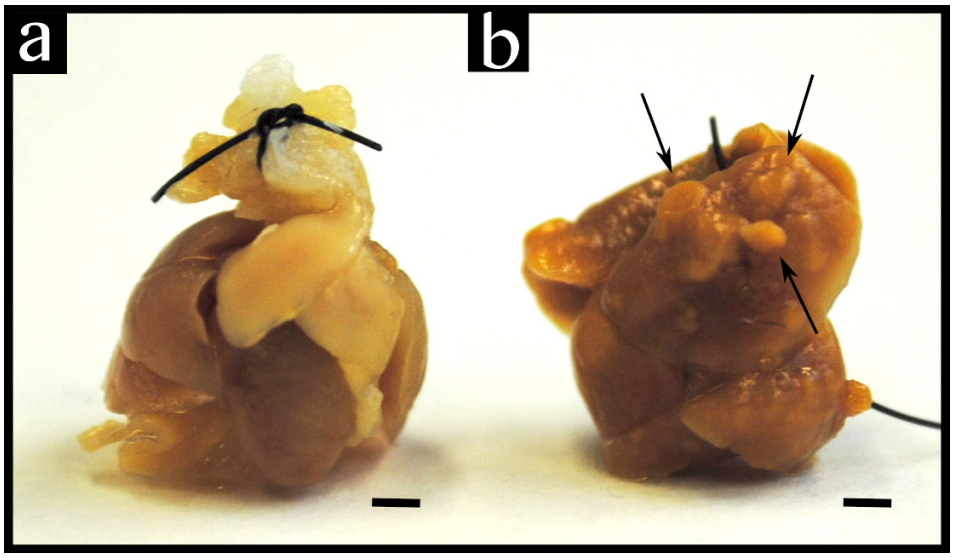

Figure 6.1: Digital photographs of inflated lungs. (a) Unstained healthy lung, and (b) stained tumorous lung. Tumors are indicated by the arrows. Scale bar: 2 mm.

μCT Imaging protocol

The commercial laboratory-based μCT system ZEISS Xradia 500 Versa (former Xradia, Inc) was used for the measurements presented here. A binning of 2 × 2 pixels was used for image acquisition to increase the statistics at a reasonably short exposure time of 12 s and the image reconstruction was performed with 1 × 1 pixel binning. All measurements were performed at a tube voltage of 40 kV and a current of 63 μA using the 0.39× objective lens. The source-to-sample and sample-to-detector distances were chosen individually for each specimen in order to capture the entire sample in the optimal FOV. Consequently, the effective pixel size of scans differed slightly from each other, but was in the range of 12–13 μm. A total of 1201 projections over 360 degrees were acquired for each scan.

Visualization

The 3D rendered images shown here were obtained from data reconstructed as 16-bit TIFF and processed with the software VGStudio Max (Volume Graphics GmbH, Heidelberg, Germany). Thereafter, segmentation was performed to depict the tumors from the lung tissues. For an accurate volume extraction of the tumorous areas, the semi-automated tool "region grower" available in VGStudio Max was used. This tool selects a region with a flooding algorithm. The "static mode" option adds a voxel if it has a gray value that varies not more than half of the adjusted tolerance.

6.2.2 Results

A comparison of an unstained lung with a stained one, both analyzed by μCT under the same experimental conditions, highlights the need of a contrast agent to observe well-resolved structures in the sample (Fig. 6.2). In the unstained lung (Fig. 6.2(a)), the gray values of

lung tissues and ethanol do not differ considerably, making any precise definition of pulmonary structures extremely difficult. In this work, we treated lungs with a few different soft-tissue staining protocols from the literature [Metscher, 2009a, Fernández et al., 2014], including one based on phosphotungstic acid (PTA) and others based on iodine (Fig. 6.2(b) and Fig. 6.3). Among them, the ethanol-based iodine (I2) solution, named I2E, resulted in a great increase of contrast of the soft-tissues and the finest structures of the lung were clearly highlighted. Lobe bronchi as well as the terminal bronchioles were well resolved (Fig. 6.2(b)). This contrast medium diffuses homogeneously through the connective tissues of the lung and binds to the vascular walls. Consequently, it significantly improved the contrast within the lung structures and was then used in the following investigations.

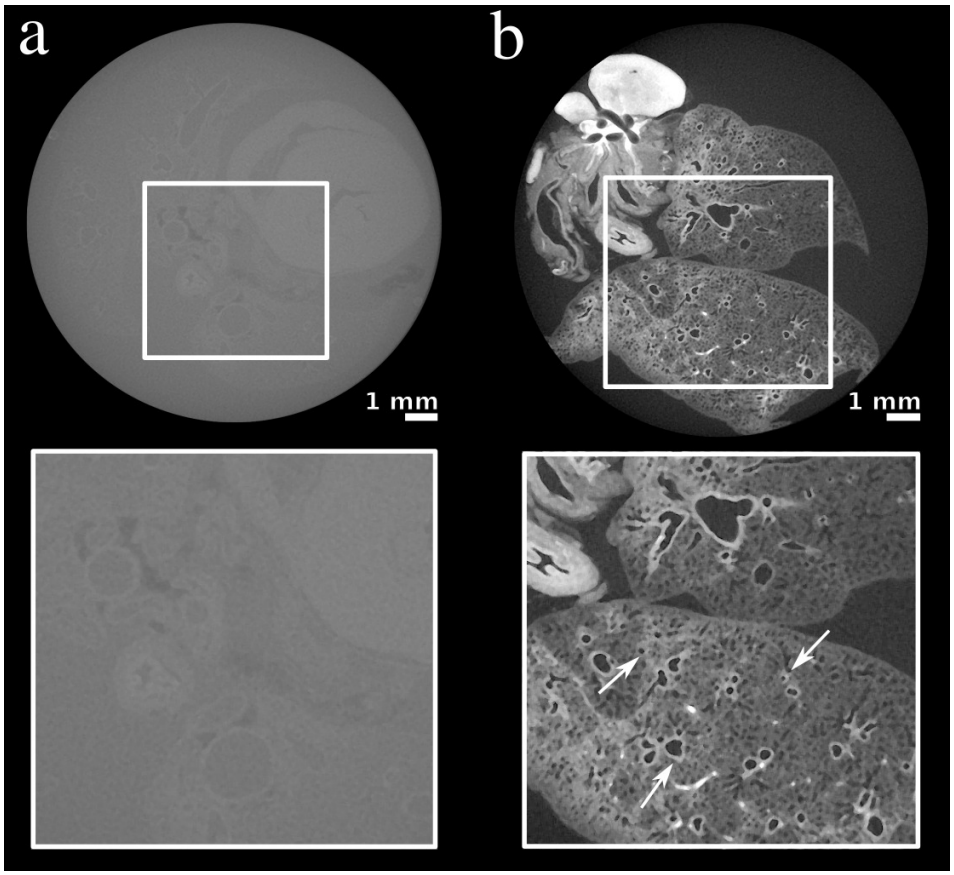

Figure 6.2: Comparison between unstained and stained lungs. The staining procedure with I2E increased the image contrast, as is seen in the comparison of the tomograms of (a) an unstained sample and of (b) a lung stained with I2E. Enlarged images of selected regions are shown below the corresponding sample to show details. Arrows indicate lobe bronchi and small air ducts.

When applied to a diseased lung, we confirmed that I2E not only spots the main features of the organ, but also highlights the tumorous areas (Fig. 6.4(a)). The good contrast provided by this staining agent as well as the air present in the lung capillaries allows the segmentation of tumors and air ducts from the surrounding tissue (Fig. 6.4(b)). The contrast and the details revealed in the tomograms can be displayed in a histogram consisting of gray value

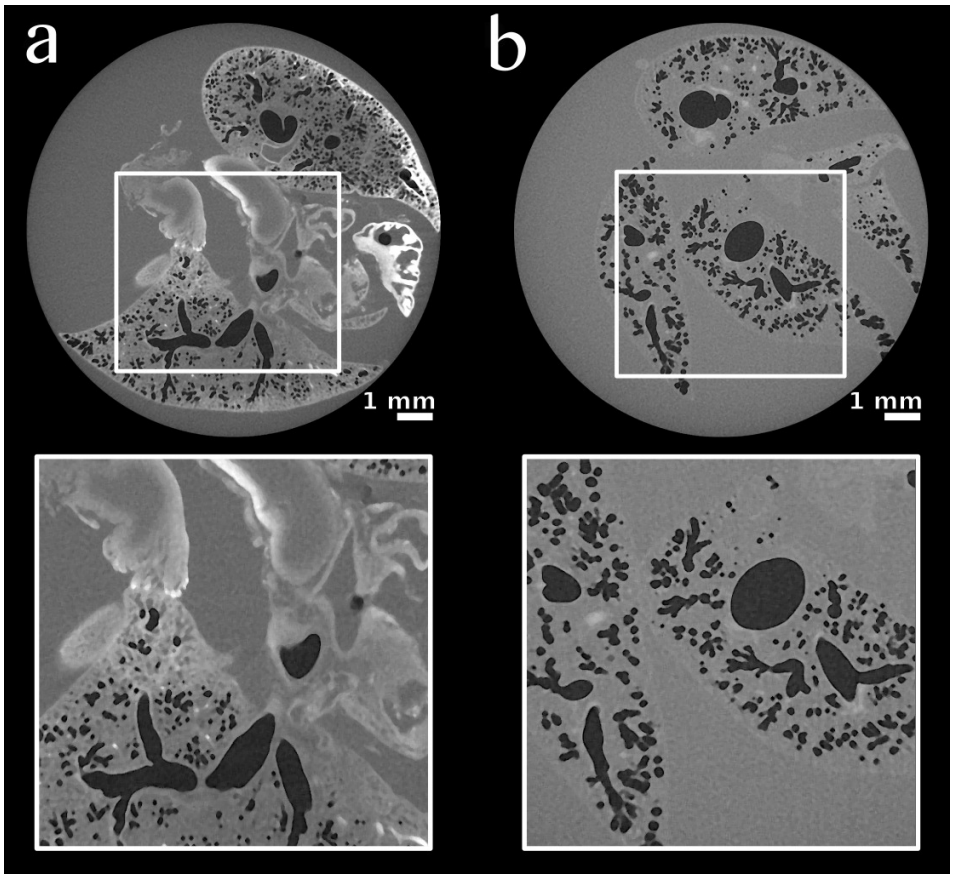

Figure 6.3: Tomograms of lungs stained with other staining agents tested. Tomogram of (a) lung stained with PTA and of (b) a lung stained with I2 in KI aqueous solution (IKI). Zooms of selected regions are shown below the corresponding sample.

intensities (Fig. 6.4(c)). A segmentation procedure consists in the selection of a range of gray values corresponding to a specific tissue out of the total of gray values, which correspond to the entire volume of the specimen analyzed. This differentiation of the lung content in gray values allows the estimation of the percentage of tumors within the volume of the organ. We used a semi-automated tool to segment the lesioned regions in this lung. The lesions in this specific sample are illustrated by the areas pseudo-colored in pink, corresponding to 15.4 % of the entire volume of the lung that was rendered transparent in (Fig. 6.4(b)). Further analyses performed on three supplementary tumorous samples, which were stained with I2E as well (Fig. 6.5), indicate that the volume of tumorous lesions in the lungs changes according to the mouse model, and is equal to 1.6, 2.0 and 6.5 % in Fig. 6.5(d), (e) and (f), respectively.

The tumorous lungs were primarily analyzed by μCT then later embedded in paraffin, sliced, stained with hematoxylin and eosin, and imaged at an optical microscope. Virtual slices from μCT and similar H&E-stained slices of the same sample are compared (Fig. 6.6). The contrast at high-spatial resolution allows the differentiation of lesions from the healthy tissue areas in these lungs' virtual and histological slices (Fig. 6.6(a)–(c) and (d)–(f), re-

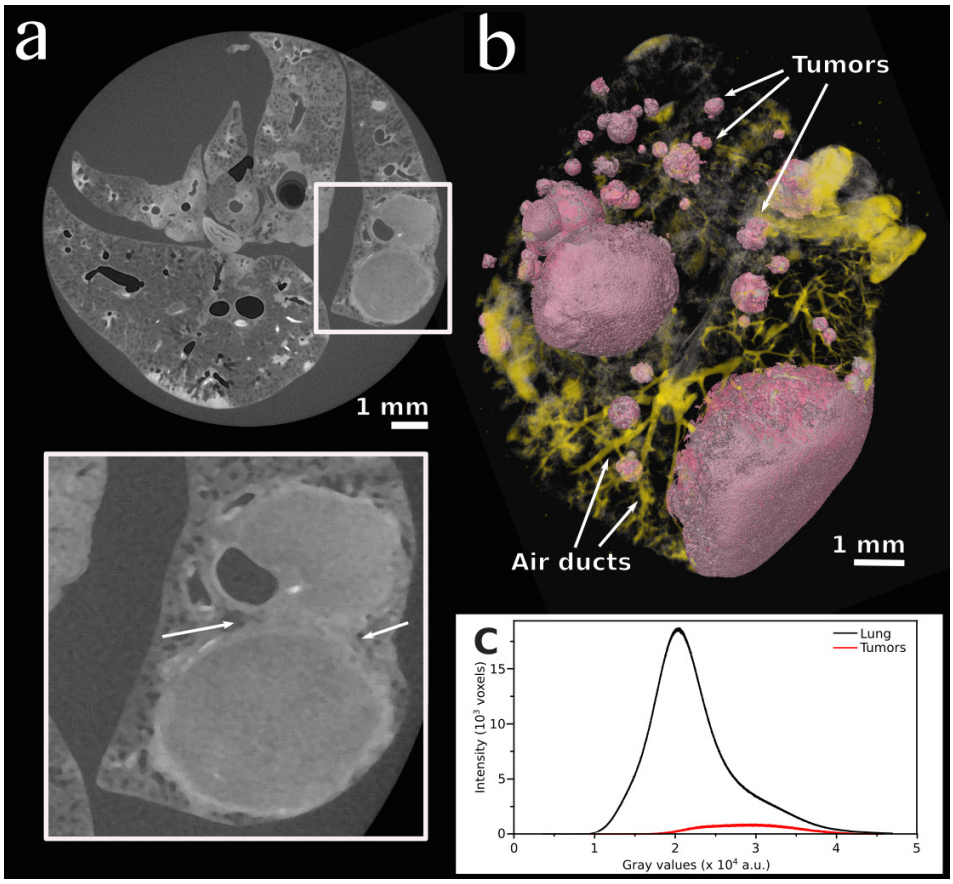

Figure 6.4: Images of a tumorous lung. (a) Tomogram of a tumorous lung. The area selected by the square was enlarged to show a tumorous area and the undefined boundaries between two tumors. (b) The excellent contrast obtained for lesions (due to I2E staining) and air ducts allowed their segmentation and reconstruction shown in this image, where tumorous areas with spheroidal morphology (light pink) and air ducts distribution (yellow) are well discriminated from the healthy soft-tissue, rendered colorless, therefore not visible. (c) Distribution of voxel intensity values for the whole organ and for the total volume of tumors in this sample, which corresponds to 15.4 % of the entire lung's volume.

spectively). Nonetheless, a comparison between the tumorous areas marked in a histological slice and the nearly equivalent μCT virtual slice shows differences in the areas delineated (Fig. 6.7).

6.2.3 Discussion

In this study, iodine-stained tumorous lungs from mouse models of pulmonary cancer were inspected with μCT. The need of using a contrast agent in attenuation-based μCT of organs is demonstrated in the comparison of an unstained lung (Fig. 6.2(a)) with a stained one (Fig. 6.2(b)). We tested some staining solutions containing either tungsten or iodine as X-ray absorbing elements, and we finally selected an iodine in ethanol solution (I2E) as the best

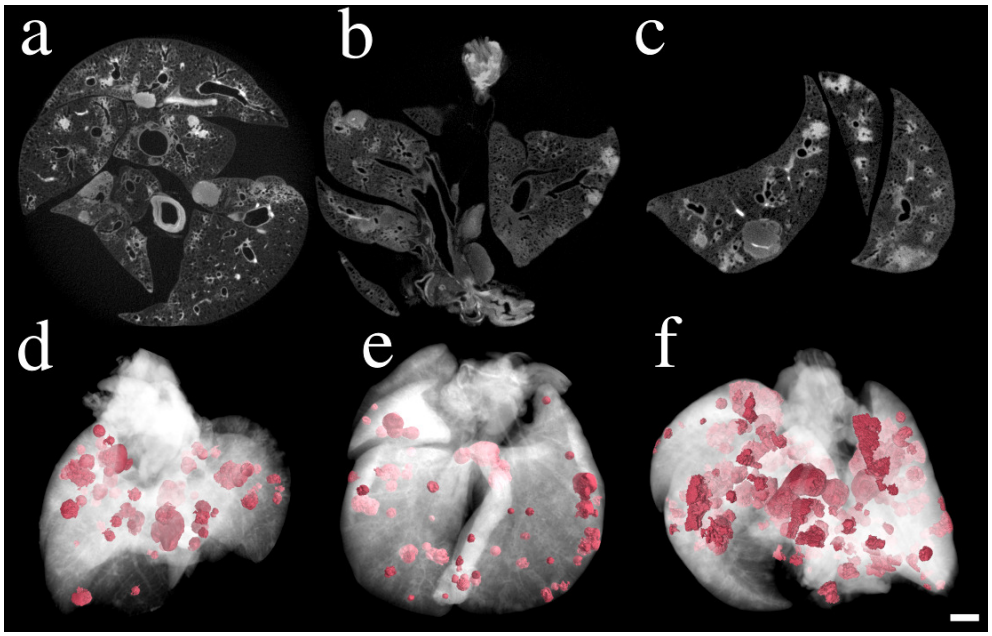

Figure 6.5: 2D and 3D images of three different I2E-stained tumorous lungs. (a)–(c) Tomograms of three different types of lung samples carrying tumors show lesions, including some tumors with undefined boundaries. Below, their corresponding three-dimensional renderings are shown (d)–(f), with normal lung tissue represented in transparent white to allow the visualization of the tumorous lesions pseudo-colored in pink. Scale bar: 1 mm.

staining agent for our purposes (Fig. 6.2(b) and Fig. 6.3). I2E is known as a good contrast agent to highlight the morphology of organs of mammals [Rasch et al., 2016] and, as we show here, it is also adequate to discriminate areas of healthy tissue from unhealthy tissue in diseased lungs. Due to the small voxel size obtained in the reconstructed I2E-stained lungs, we were able to segment the tumors that grow with defined boundaries using a semi-automated tool of the VGStudio software. However, the growth of tumors does not always occur with well-defined limits and burdens may not have very precise edges, as indicated, for example, by the arrows in the enlarged area in Fig. 6.4(a). These areas are a challenge for the semi-automated segmentation. Therefore, additional manual intervention was taken along with an interpolation over the reconstructed slices to obtain the reconstructed lungs shown in Fig. 6.5. To validate our method, the tumorous lungs previously analyzed by µCT were later stained with the well-established H&E-staining protocol and imaged with an optical microscope. Routine H&E-staining plays a key role in histopathological studies of tissues for diagnosis and research purposes. It yields excellent contrast to the histological slice images obtained with an optical microscope, thus tissue morphology as well as tissue microscopic changes and abnormalities can be well identified. The H&E-stained slices of three different diseased lungs are compared to similar virtual µCT slices in Fig. 6.6. Almost identical structures are observed in both the H&E-stained slices (Fig. 6.6(d)–(f)) and the analogous virtual µCT slices (Fig. 6.6(a)–(c), enlarged areas), such as indicated by the arrows that identify tumor burdens (blue) and blood vessels (red). A meticulous analysis of one histological slice and a much comparable virtual µCT slice shows differences in the

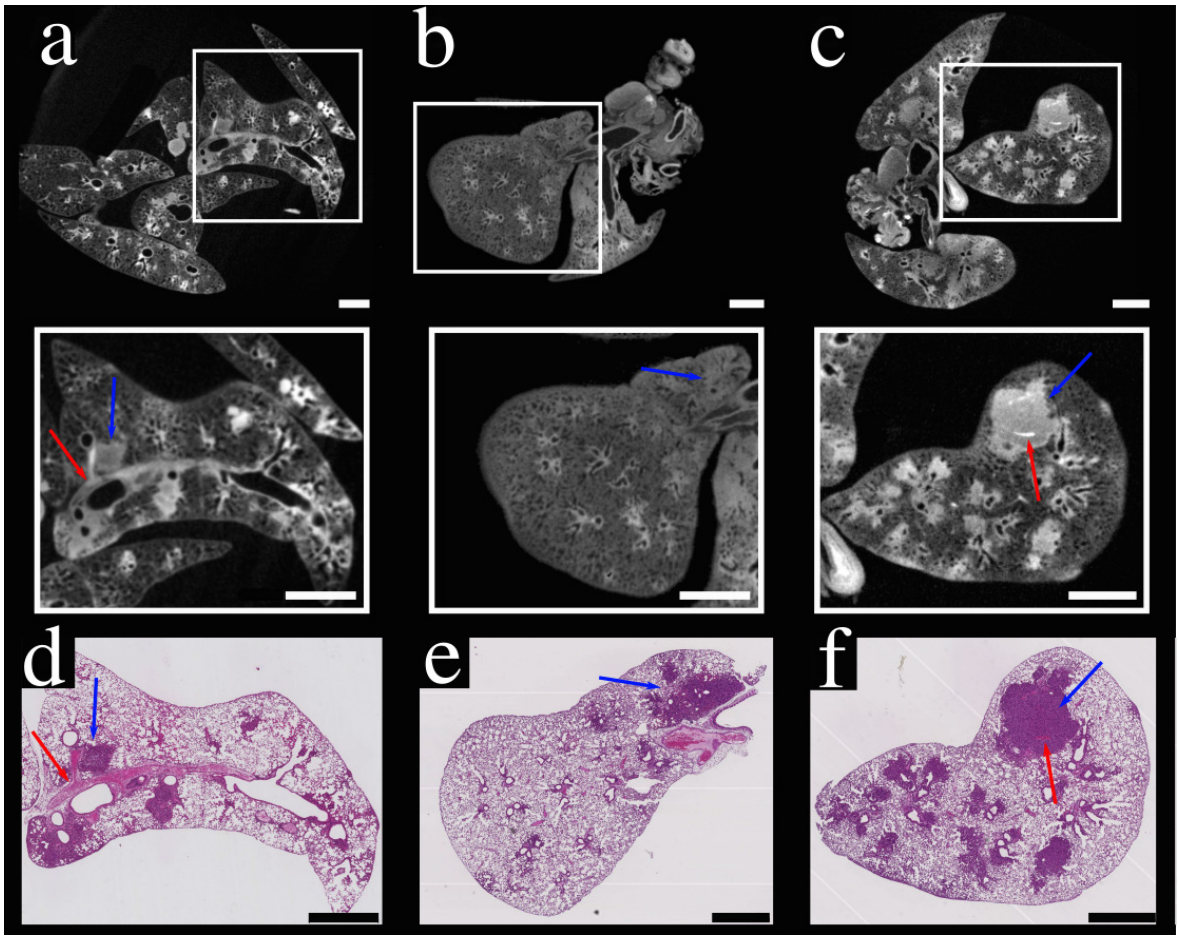

Figure 6.6: Tomograms and comparable H&E-stained histological sections of three tumorous lungs. (a)–(c) Tomograms of tumorous lungs, with the corresponding framed highlighted areas shown below. The regions of these tomograms are equivalent to the histological slices shown in (d)–(f). Blue arrows point tumor burdens, while red solid arrows indicate blood vessels. Scale bar: 1 mm.

areas identified as tumors. The tumorous regions marked with red lines in histological slices in Fig. 6.7(a) and (b), were delineated by an experienced pathologist. They correspond to 20.5 % (Fig. 6.7(a)) and 3.3 % (Fig. 6.7(b)) of the total surface of the lung in these specific slices. Other areas located in the outer limit of the red contours, although stained in a darker pink tone, do not correspond to tumors, but to abnormal tissue such as inflammation, dead and/or stressed tissue. The segmentation tool used to define the tumorous areas marked in red in the virtual µCT slices give slightly higher numbers of tumorous areas (22.8 % in Fig. 6.7(c) and 10.5 % in Fig. 6.7(d)). Even considering small deviations conditioned by the individual interpretation of suspicious structures in the histological slice, there is a discrepancy between the percentage of tumorous areas in the histological (Fig. 6.7(a)–(b)) and virtual µCT slices (Fig. 6.7(c)–(d)). The stain (Iodine) used here to improve the contrast in µCT is non-specific to tumorous tissue, and therefore stains similarly the inflammation and the dead and/or stressed tissue.

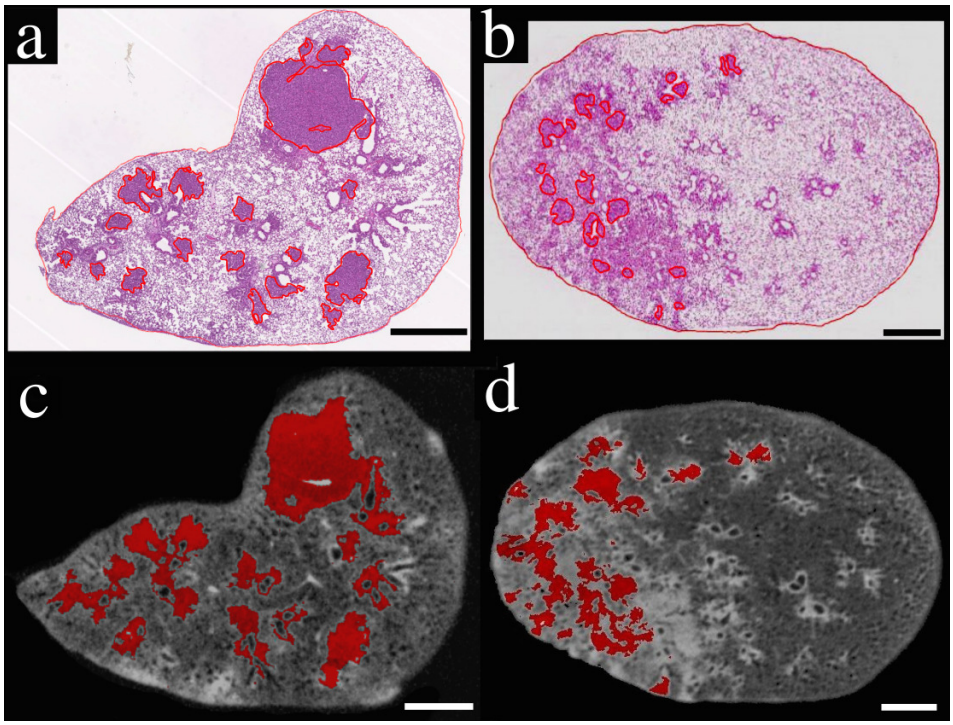

Figure 6.7: Segmentation of tumorous areas in histological sections and their more resembling virtual µCT slices. (a)–(b) Histological sections of diseased lungs with tumorous areas circumscribed about red lines. (c)–(d) Virtual µCT tomograms, corresponding to the histological slices above. Red marked areas correspond to tumors identified using the semi-automated "region grower" tool of VGstudio Max. Scale bar: 1 mm.

Nowadays, H&E is the gold standard in histopathological studies, providing a detailed representation of tissues with high resolution, thus allowing to identify tissue abnormalities. However, it is known that even among experienced histopathologists some differences in the evaluation of tumor extents are likely to occur. Moreover, histopathology does not allow the volumetric study of tumors, since evaluating the percentage of tumorous areas based on a few histopathological slices presents a major drawback related to the missing information from the excluded slices. Hence, performing µCT prior to H&E-staining would be advisable in a workflow, as the first does not prevent the latter to be completed. Especially in the case of tumor volume studies, µCT would provide extra volumetric information that is important in the evaluation of potential differences in the macroscopic growth of patterns among tumor types.

6.2.4 Conclusion

In conclusion, here we show that the selection of an appropriate staining protocol combined with µCT is an adequate method for studying healthy lung tissues at high resolution and with high contrast, leading to non-distorted 3D information and inherent registration of the slices without the need of physical sectioning of the sample. Specifically in mice models that produce lung tumors with well precise boundaries, our described method could be used

to evaluate the tumorous tissue volume. However, for tumors surrounded by multiple inhomogeneous tissue modifications, such as inflammations, dead or stressed tissue, our semi-automated segmentation method overestimates the tumor margin, thus giving the percentage of general unhealthy tissue in the entire organ. As diagnostic accuracy plays an important role in research, we believe that for a more reliable volumetric quantification of ex-vivo tumorous lung tissue, which is an important parameter in cancer research, the combined use of H&E histology and μCT would provide extra information, not available in one single imaging technique. Moreover, the presented method holds a great potential to be explored as a 3D histopathology procedure if staining agents capable of targeting specifically the tumor cells are used.

6.3 Industrial applications

6.3.1 Batteries

Motivation

Li-ion batteries are sustaining standardized employment in energy storage and are widely used in portable electronic, as well as electric and hybrid electric vehicles due to their high power and energy densities. However, some reasons of concern in their improvement are thermal safety issues [Doughty and Roth, 2012] and their loss of performance overtime [Jacoby, 2013]. High-speed synchrotron radiation CT has been used in conjunction with thermal imaging for this purpose to assess the progress of internal structural deformation during thermal abuse [Finegan et al., 2015a]. By a similar study, the material displacement that results in degradation mechanisms and loss of performance of the battery has been captured in real time [Finegan et al., 2015b]. Few factors that also affect the performance of these batteries are spatial inhomogeneities of the current, the lithium and the electrolyte [Senyshyn et al., 2015] according to the cell design. To this end, Senyshyn et al ([Senyshyn et al., 2015]) initiated a spatially-resolved neutron powder diffraction as an in situ method to probe the lithium concentration in the graphite anode of different Li-ion cells. They used laboratory-based X-ray CT mainly to favour the morphological correlation with the scattering angles registered in the neutron diffraction. In connection with this, the current section aims to unveil the usefulness of laboratory systems, especially in the study of batteries.

Experimental

A commercial Li-ion cell of 18650-type was chosen to be illustrated in this part. It has been non-destructively probed using X-ray tomography with v|tome|x s 240. The direct tube was used with a voltage of 130 kV and a current of 100 µA. With a sample of approximately 18.5 mm in diameter and 66 mm in height, the effective pixel size of the scan was rather defined by the width of the sample that fits in the field of view, so that a value of 40 µm was achieved. Therefore, two datasets (top and bottom part) of the cell were acquired, each with 1000 projections. Note that a projection consists of an average of 3 single exposures recorded in 1000 ms each. The datasets were reconstructed and merged using the costumery software phoenix datos|x and ImageJ, respectively.

Indeed, the interest pursued in this research is to find out the lithium prevalence in the graphite anode at the state of charge. Since lithium is a low Z atom, it is apparent that the use of X-ray absorption/attenuation imaging could not effectively lead to an adequate resolution. Hence the use of spatially resolved neutron diffraction. Nevertheless, the planar 2D reconstruction of the distribution of the lithium concentration as shown in Fig. 6.8(f) requires the angles of neutron scattering events to correlate with the morphological constitution of the investigated specimen. There lies the validity of the message highlighted in this section, namely the importance of using X-ray µCT in combination with other methods to solve several inquiries. A selected 3D reconstructed slice (Fig. 6.8(b)) shows inherently the inner skeleton of the cell, especially the electrodes comprised in the enlarged regions (Fig. 6.8(a) and (c)). This constitutes a decisive contribution as the building of the electrodes

inside Li-ion cells differs according to the manufacturer.

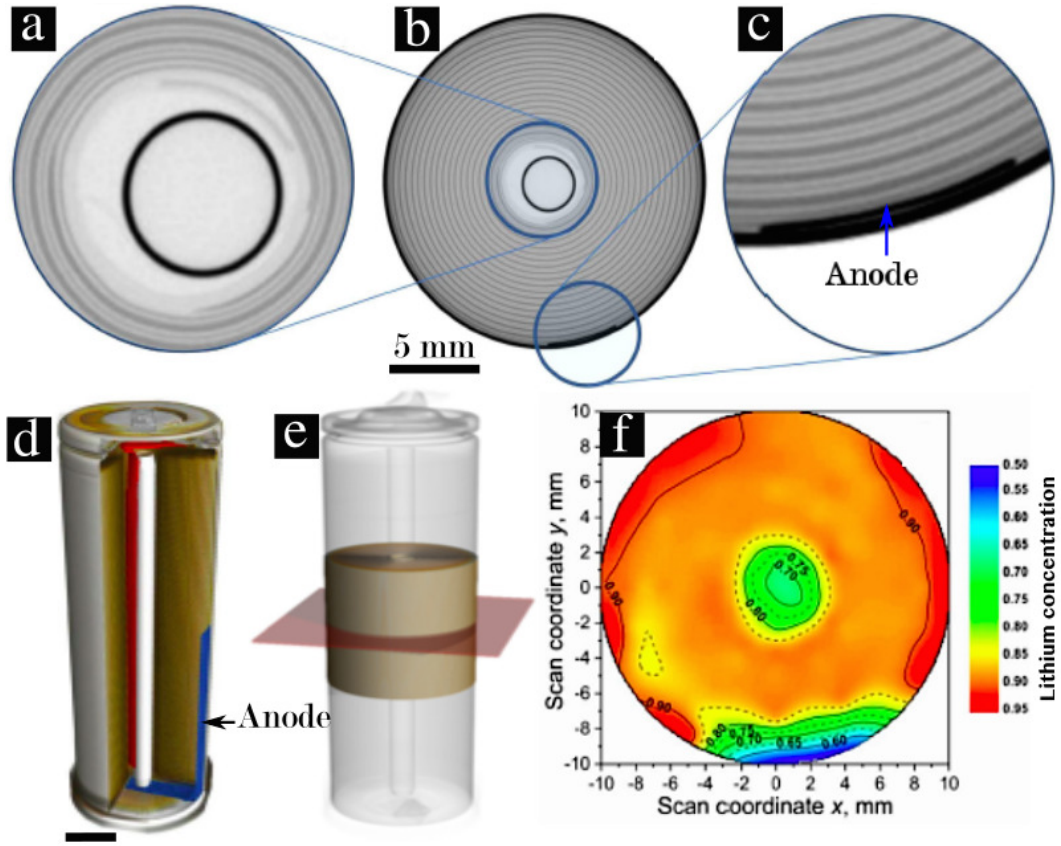

Figure 6.8: Li-ion battery investigated by means of X-ray imaging and neutron powder diffraction. (a) and (c) represent zoomed regions from the tomogram (b), issued from the 3D reconstruction of the sample scanned by X-ray tomography. (d) and (e) illustrate 3D renderings of the sample. In (f), a 2D planar distribution of lithium concentration through the plan selected in (e) is displayed, and also corresponds to the tomogram in (b). Some of these images were kindly provided by Dr. Martin Mühlbauer[1], whereas others were partially adopted from [Senyshyn et al., 2015]. Scale bar: 5 mm.

In the 3D renderings carried out with VGStudio Max (Fig. 6.8(d) and (e)), the selected section corresponds to the tomogram in Fig. 6.8(b) and the planar distribution of lithium in the cell (Fig. 6.8(f)). For more details on the spatially-resolved neutron powder diffraction experiment, one may refer to [Senyshyn et al., 2015].

Conclusion

In order to remain concise in the message conveyed above, the spatial-resolved powder diffraction has not been stretched. The involvement of X-ray μCT was shown as essential to

[1]Heinz Maier-Leibnitz Zentrum (MLZ), Technische Universität München, Lichtenbergstr. 1, 85748 Garching, Germany.

perform the main experiment, which consisted of tracking lithium distribution in a Li-ion cell of 18650-type. X-ray µCT performed at middle resolution (ps_{eff} = 40 µm) at the laboratory facility v|tome|x s 240 is demonstrated as a simple case of delightfulness of laboratory X-ray systems and unnecessariness to turn to extremely high-resolution and high-power facilities.

6.3.2 Dual-energy CT of precious stones

Motivation

In fact, gold extraction is an expensive process which requires optimization to reduce the expenses. A determination of particle size and crack density is essential for this purpose as it has been proven to correlate with efficient gold extraction [Nwaila et al., 2013]. During their investigation performed on gold ores from the Witwatersrand Basin in South Africa, latter authors made among others use of the X-ray micro-tomography showing several composites such as chlorite-muscovite, quartz, uranium oxide and pyrite. Gold particles though are relatively small with a general particle size range of 5 µm to 1.2 mm [Hallbauer and Joughin, 1972] and are strongly associated to pyrite [Koglin et al., 2010]. Hence, high-resolution (microscopic) imaging is recommended and the discrimination of gold particles from the obviously surrounding pyrite is desirable. This implies the investigation through microscopic X-ray DECT of a gold ore sample from Witwatersrand, that was provided in a collaborative work by Lunga Bam (South African Nuclear Energy Corporation, NECSA).

Merits of DECT

Sample description The gold ore specimen presented in the following has a maximum size of 11 mm in length, 5 mm in width and 2 mm in thickness (Fig. 6.9(a)). The sample did not require any specific preparation prior to the measurement.

Experimental procedure The investigation was done at ZEISS Xradia 500 Versa. An initial scan has been performed at 60 kV with a filter (denoted by LE #2) made of a 330 µm thick SiO_2. By using the 0.39× objective the geometry was adjusted to achieve an effective pixel down to 5.23 µm. For this value, a region of about 5.35×5.35 mm^2 could be scanned. Therefore, three successive regions of the sample were scanned in separate steps and merged at post-reconstruction thanks to the accustomed reconstruction software XMReconstructor. At each step 1600 projections were acquired with an exposure time of 8 s.

Results and discussion In Fig. 6.9(a), a 3D rendering of the gold ore is displayed. Its corresponding histogram resulting from the CT scan is shown in Fig. 6.9(b). Herewith, the compounds contained in the sample were differentiated by simple threshold. The color coding in the histogram perfectly fits to the components revealed in Fig. 6.9(c), namely gold, pyrite and quartz. The area circled in this last image was reproduced in a local tomography at higher resolution (ps_{eff} = 1.9 µm), from which the histogram plotted for the gray value regime of pyrite and gold (Fig. 6.9(e)) is equivalent to the dissociation shown in Fig. 6.9(b).

Notice that gold particles are morphologically located adjacent to other components, whose mass attenuation coefficients are also close to each other ([Nwaila et al., 2013],

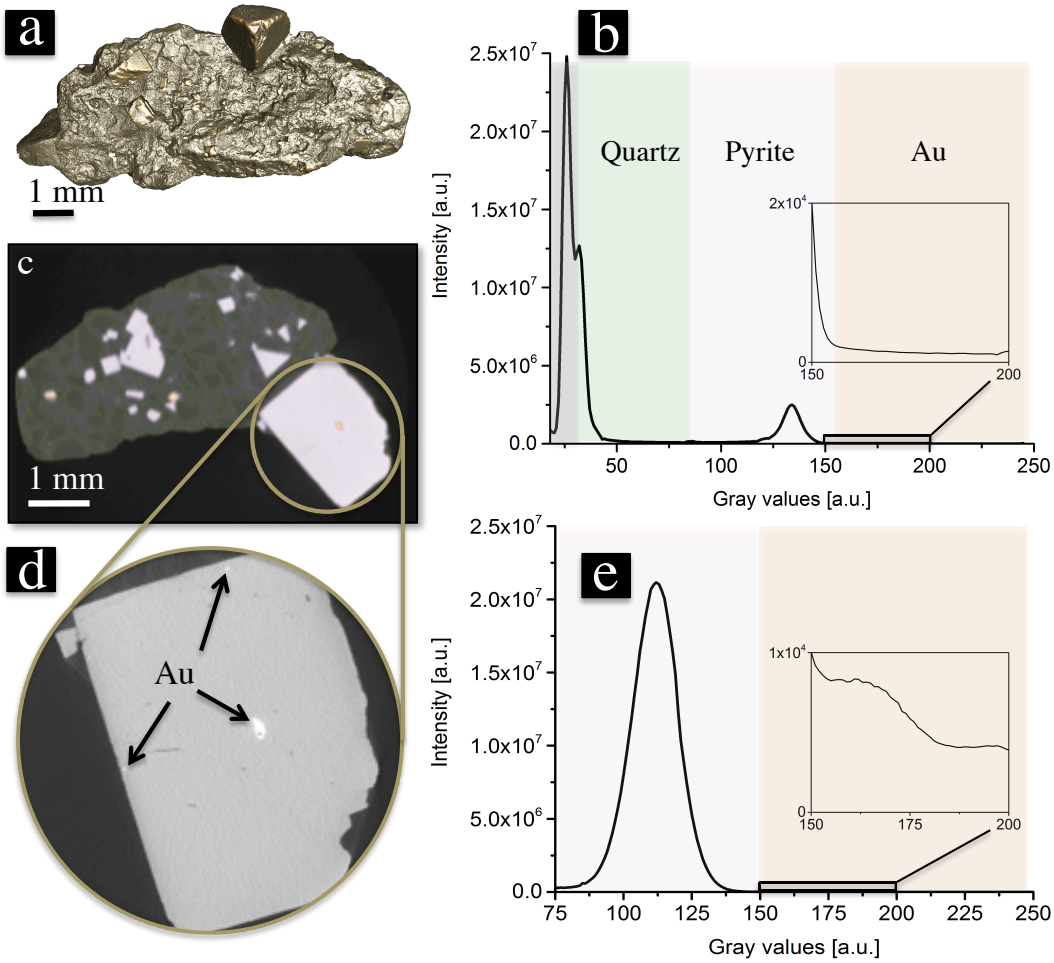

Figure 6.9: Gold ore sample from the Witwatersrand Basin in South Africa. (a) 3D rendering of the sample. (b) The histogram ensued from the CT scan at sub-micron resolution using ZEISS Xradia 500 Versa. Through simple thresholding, different materials could be represented as displayed in the tomogram (c). (d) Scan of the region selected in (c) at a higher resolution, that enabled to resolve highly absorbing features – more likely gold (see arrows). By omitting air, (e) displays an equivalent composition as in (b).

Fig. 4a), e.g., gold (Au) and lead (Pb). For this reason the use of the term **gold** is empirical, since the lead content of the sample would be misinterpreted as pure gold.

Merit of setup optimization for DECT

Experimental procedure The sample has been scanned additionally at 120 kV using a 2500 µm thick CaF_2 filter. Both spectra used for the purpose have been simulated using the pyPENELOPE[2] software and are plotted in the Fig. 6.10(a). Using these compound filters deal to clearly separate the average energy of the beam without cutting its K-edges. In fact, the filters eliminated the low energies of each polychromatic spectrum and thus increased the

[2] http://pypenelope.sourceforge.net/documentation.html (accessed: 2017-01-18).

average energy of the beam, which is denoted by **beam hardening** (see [Van Metter et al., 2000], chapter 1).

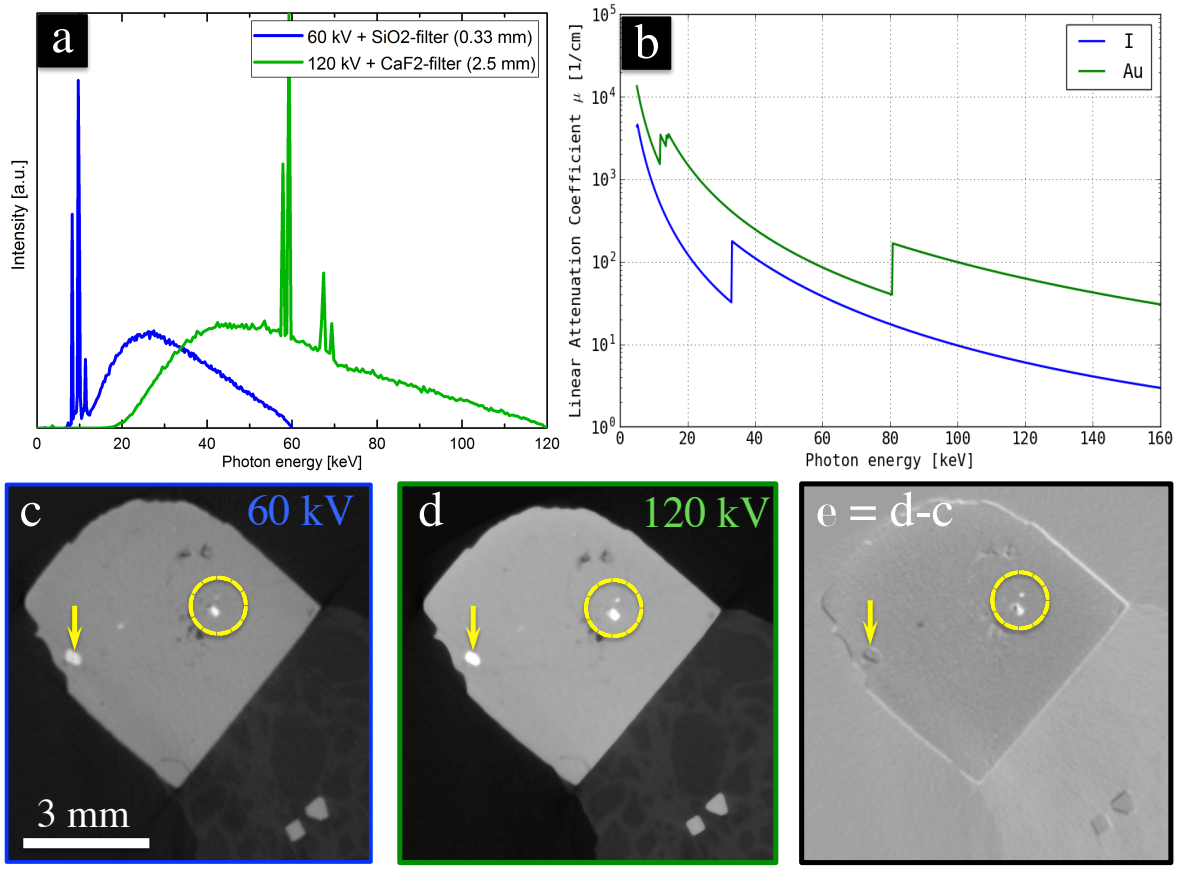

Figure 6.10: First (non-optimized) attempt of microscopic dual-energy CT. (a) Simulated spectra using pyPENELOPE [Pinard et al., 2010] for tube voltages of 60 kV (blue) and 120 kV (green), which were filtered respectively with a 330 µm thick SiO_2 and a 2500 µm CaF_2 filters. (b) The mass attenuation cross sections of Iodine (I) and gold (Au) are plotted. (c) – (d) Tomogram of the gold ore scanned with the blue spectrum (60 kV – filtered) and the green spectrum (120 kV – filtered), respectively. The arrows and the circles highlight high-absorbing features. (e) The subtraction of the tomograms in (d) and (c) is displayed. Here, the difference in contrast between the high absorbing materials featured in (c) and (d) shows that they are non-identical.

Results and discussion In [Krissak et al., 2013], the authors took advantage of the K-edge of gold (81 keV) being located in the energy range of diagnostic CT to show the benefit of gold as a potential contrast agent for DECT as its mass attenuation coefficient lay sufficiently apart from that of iodine (see Fig. 6.10(b)). The contrast has then been proven optimal for iodine at 80 kV and for Gold at 140 kV.

Figures 6.10(c) and (d) display tomograms of the sample initially scanned with 60 kV and subsequently with 120 kV. In the subtraction of both data (Fig. 6.10(e)), the example pointed

by the arrow indicates that this feature has sustained a slight difference in attenuation upon the acquisition with different energies. The region encircled shows a feature similar to the observation in Fig. 6.10(c) and (d) and conveys a strong difference in attenuation within both data. It is conceived that this simple procedure works for high differences in attenuation but may not lead to reliable results within a composite material such us the gold ore.

This result demonstrates the need for optimization of the spectra in relation to the sample investigated, which might improve the contrast by applying microscopic DECT.

Optimized DECT

The purposes stated in the motivation of this section have been thoroughly investigated in [Schwarz, 2014]. From that work, which covers different aspects of the dual-energy μCT, it is chosen to resume the post-processing analysis of the gold ore in the following.

Experimental procedure The low – and high energy scans were recorded throughout optimization at 40 kV without filter and 160 kV with a 5.01 mm thick CaF_2 filter. A single region of the sample was scanned with an effective pixel size of 4.23 μm using the 4× objective. In order to avoid a predictable low SNR in the high energy measurement, 400 more projections were acquired than in low energy scan performed with 1601 projections. The SNR was enhanced in both data by experience using a 3D median filter with kernel 7, which was applied two-times on the high energy dataset and once on the low energy dataset. The analysis of the DECT datasets was performed with a Dual Scan Contrast Visualizer (DSCoVer) by ZEISS Xradia.

Results and discussion High and low energy data are loaded subsequently and combined into one data from which a 2D histogram is retrieved (see Fig. 6.11(a)). A drop-like pile up of intensity pair denotes the predominance of a material. Air is systematically located at the bottom of the 2D histogram. The misalignment of the intensity pairs symbolizes the presence of several materials of non-identical densities within the selected histogram. In Fig. 6.11(a), the white straight line testifies the occurrence of a high absorbing material of identical density in the selected reconstructed slice. Nevertheless, the exact determination of this material was intractable without further exploration although the element could be yet easily segmented from the combined dual-energy data using the 3D visualizer Avizo Fire (FEI, 5350 NE Dawson Creek Drive Hillsboro, Oregon 97124 USA). Compared to Fig. 6.11(b), this appearance is illustrated with the red-circled particle in Fig. 6.11(c). Thus a repetition of the dual-energy scan was completed on a phantom made especially of some elemental minerals already known from [Nwaila et al., 2013]. Hereafter, slopes could be identified for each material and enabled the assignment of the white straight line to Lead (Pb).

Summary

Using the X-ray microscope ZEISS Xradia 500 Versa, it has been demonstrated that dual-energy CT at sub-micron resolution can be implemented in laboratories for practical use in the decomposition of compounds such as the gold ore presented in this section. This

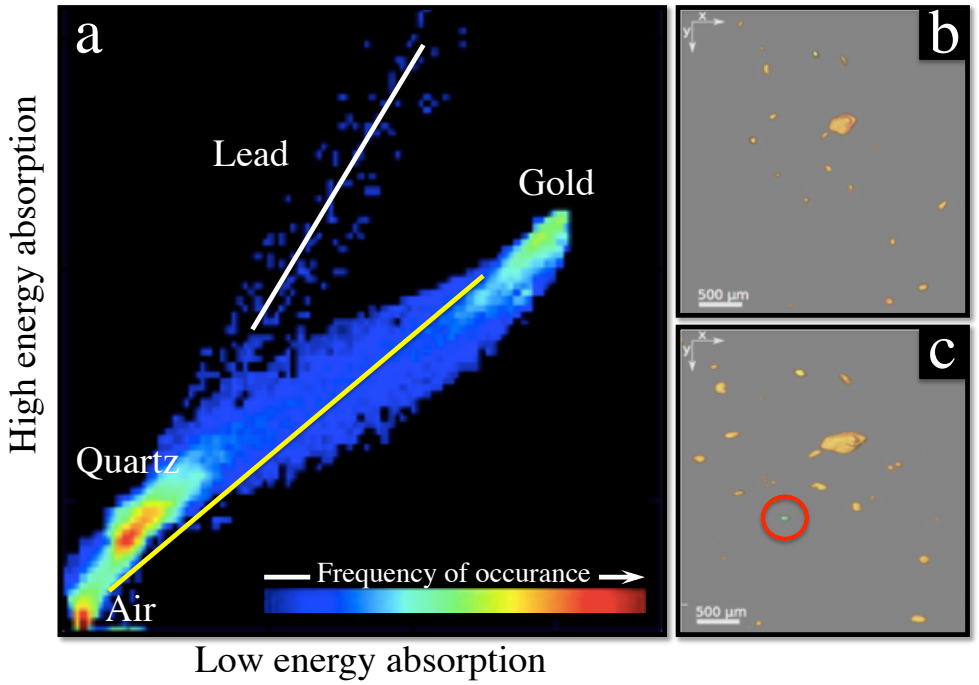

Figure 6.11: Analysis of combined data from low energy (40 kV) and high energy (160 kV) scans of the gold ore. (a) 2D density histogram of the combined datasets. The lines represent traces of the elements such as gold (yellow) and lead (white). (b) Segmentation of gold particles from the high energy scan through simple thresholding–using the 3D visualization software Avizo Fire. (c) Appearance of a new material (see red circle) in addition to a better detection of gold particle through the material decomposition procedure. Figures courtesy of [Schwarz, 2014].

technique can be granted an establishment in laboratories and demands knowledge about the elemental composition of the object, which can however be resolved by complementary methods like X-ray fluorescence (XRF) [Schwarz, 2014].

6.4 Conclusion

Three specific cases of practical use of micro- and sub-micro-computed tomography have been presented. They illustrate usability in various fields of research including biology, battery and the mining industry. Two aspects of growing imaging strategies were experimented. The first is the staining of biological specimen, which, combined with µCT has been shown as a promising method for imaging biological specimens in the laboratory. The tumor quantification performed here was based on the contrast provided by the emphasis of intensities among healthy tissue and tumor burden, according to the distribution of contrast agent. Therefore, the improvement or development of staining protocols e.g., [e Silva et al., 2015] in collaboration with chemically trained experts are assets that may enable better morphological discrimination of structures in tissues and eventually allow morphology-based segmentation.

The second aspect is the dual-energy CT, which is mainly used in clinical application. Here, it has been shown feasible at higher resolution (dual-energy μCT) on a commercial laboratory instrument. In conclusion, the use of commercial X-ray laboratory machines is extending beyond the revelation of 3D morphology of samples. Emerging techniques as communicated in this chapter increase the interest in laboratory systems. Likewise, the next chapter demonstrates the application of another imaging method explored in this dissertation, namely the single-distance propagation-based phase-contrast imaging.

Chapter 7

Phase-contrast imaging

In the motivation with regard to our work, some methods were mentioned that emerged at synchrotron sources but were gradually introduced into laboratories with the advantage of providing usability to multiple users. This is essentially the propagation-based PCI, which was reduced in our case to the single-distance PCI for the reasons outlined in section 5.3.2. This type of imaging in 3D was executed employing advanced synchrotron light to solve practical inquiries [Betz et al., 2007, Moosmann et al., 2013], sometimes with subsequent phase retrieval [Cloetens et al., 2006]. Several setups developed in the laboratories have also demonstrated the application of this method (e.g., [Bartels et al., 2013, Penney et al., 2012]) using phase retrieval [Bartels, 2013, Boone et al., 2009]. In commercial setups, these implementations have not been proven yet. Advanced laboratory setups available as commercial products are usually provided with several courses of action, which may be already sufficient for some users for some time. However, there is still room for further development, and by conducting some imaging techniques, beyond possibilities actually procured to the users. Therefore, it is intended to investigate but essentially complete the phase-contrast imaging with phase retrieval, and hence, go further than the high-resolution μCT measurements. Complex samples and samples of significant meaning in various fields of research have been investigated by means of the aforementioned procedure.

7.1 Tomography of an Ant

7.1.1 Motivation

A number of studies on arthropods have been accomplished in μCT seeking various aims (e.g., [Westneat et al., 2003]). But they are prized in propagation-based PCI for their chemical composition, which is ideal to express diffraction, and so, the presence of the phase contrast in propagation [Penney et al., 2012, Dunlop et al., 2011]. This is also why this specimen was chosen in this work. This chapter is dedicated to the implementation of phase calculation algorithms and their performance [De Witte et al., 2009, Boone et al., 2009] using parameters collected in ZEISS Xradia 500 Versa. It is intented to highlight the variety of information that can be drawn from data recorded through phase-contrast tomography of specimens made from chitin, but the major advantage to show is the fact that the results attained are qualitatively comparable to synchrotrons, although having been achieved with a

laboratory-based commercial system.

7.1.2 Experiment and data analysis

As shown in section 5.3.5, the sample was prepared without any stringent requirements and mounted with the aid of a transparent tape on the top of a thin aluminium pipe. The experiment was performed acquiring 1601 projections at z_1, z_2 = 10, 60 mm, respectively, each with an exposure time of 6 s. A tube setting of 40 kV, 3 W and a 2-fold binning of the detector CCD camera were adopted during the experiment. The phase reconstruction was conducted with an average energy of 13.05 keV (see section 5.3.4). By considering chitin as material of the sample, a corresponding ratio $\frac{\delta}{\beta} = 1085.89$ (see Experimentation in section 5.3.5) was deemed appropriate for the single material (SM) algorithm. A regularization value α = 2.e-03 was found suitable for the phase retrieval operated on the MBA (see Eq. 3.44).

7.1.3 Results and discussion

The reconstruction of the raw data is identified as transmission. A slice throughout the reconstructed 3D data (see Fig. 7.1(a)) unveils the manifestation of edge enhancement, which is highlighted in the zoomed frame. Comparatively, the phase retrieval by means of SM (Fig. 7.1(b)) brought remarkable discrimination of limbs, that were barely distinguishable inside the head. While performing X-ray phase-contrast imaging, one must be aware that the retrieved phase map is proportional to the electron density of the measured object, $\phi(\mathrm{r}_\perp) = r_e \lambda \rho_e(\mathrm{r}_\perp)$ [Pogany et al., 1997], where r_e represents the classical electron radius and ρ_e the projected electron density. During the quantitative study in the section 5.3.4, a single material of known width was used. These facts fulfilled perfectly the requirements of the SM constraint. Thus, the conditions were unified to claim **quantitative** sensitiveness to the electron density of the material.

In contrast, for a complex material such as the head of an ant, the exact composition of which is unknown, the improvement of the contrast is admitted to be an asset of the procedure adopted. Nonetheless, it is admitted that the results are to some extent related to the electron density of the components observed in the specimen, without being exactly quantitative. For an identical virtual slice in Figs. 7.1(c) and (d), it has been proven that the reconstructions using the MBA and the SM algorithm, which are both based on the TIE, have performed well qualitatively. Therefore, Figs. 7.2(a) and (b) present 3D renderings of both the raw data reconstructed by FBP, and the data from which phase maps were calculated by using the SM prior to the 3D reconstruction. The 3D virtual section in Fig. 7.2(b) exhibits more visible structures within the specimen. This fact is explained by the distinct peaks appearing in the histograms of Fig. 7.2(c) corresponding to the 3D volumes of the data processed using the phase retrieval. Nevertheless, the hairs of the sample, visible in Fig. 7.2(a) because of edge enhancement have been partially removed. The phase-retrieval algorithms considered in this section (MBA, SM) then react as smoothing filters.

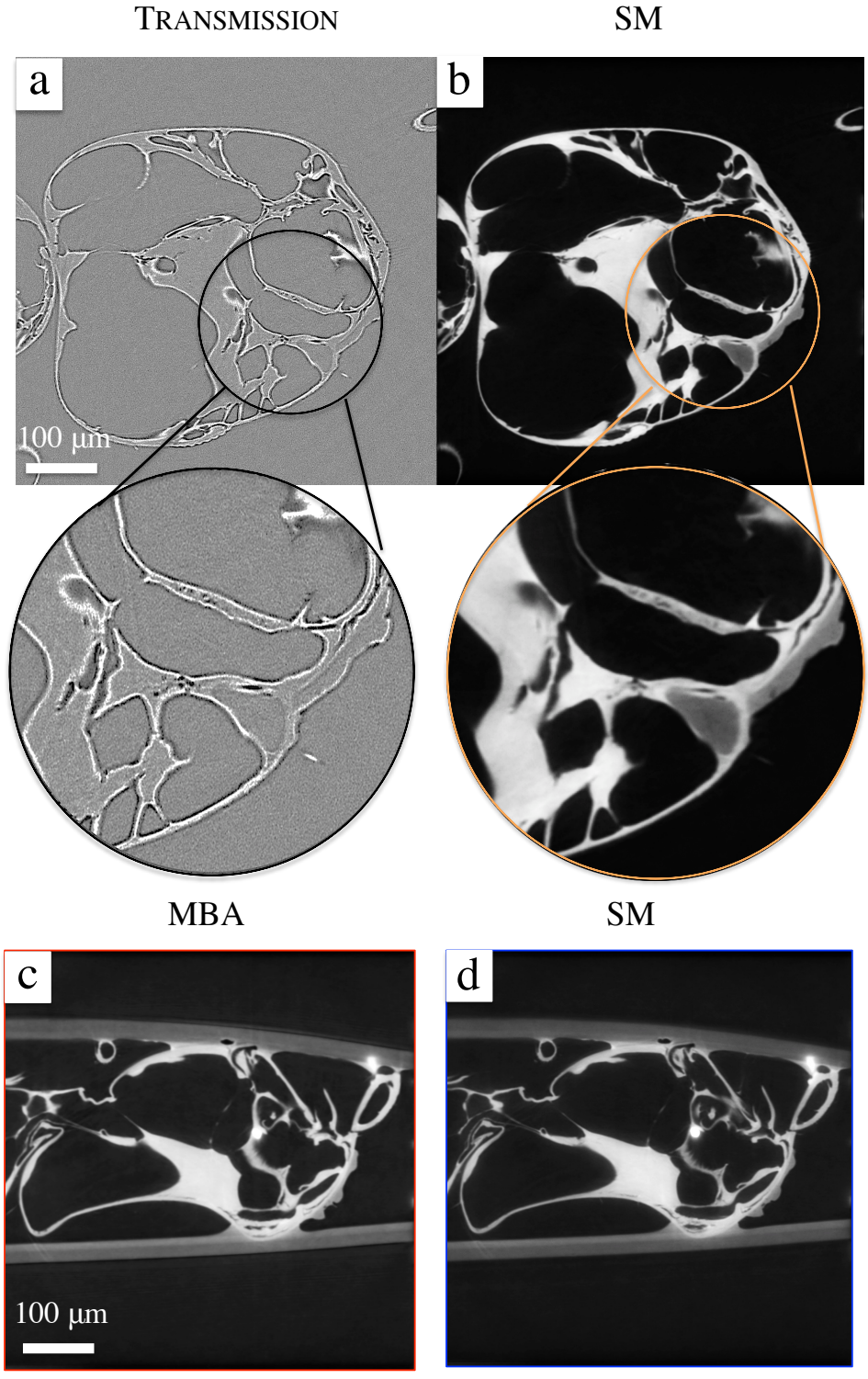

Figure 7.1: Phase-contrast tomograms of an ant's head. (a) 2D sagittal slice displaying mixed phase and amplitude. (b) The phase retrieved image of (a) using the single material algorithm is shown. Zooms within the regions encircled in (a) and (b) exhibit superior contrast arising out of the phase correction. (c) and (d) Identical profile slices reconstructed using the modified Bronnikov algorithm (MBA) and the single material (SM) algorithm, respectively.

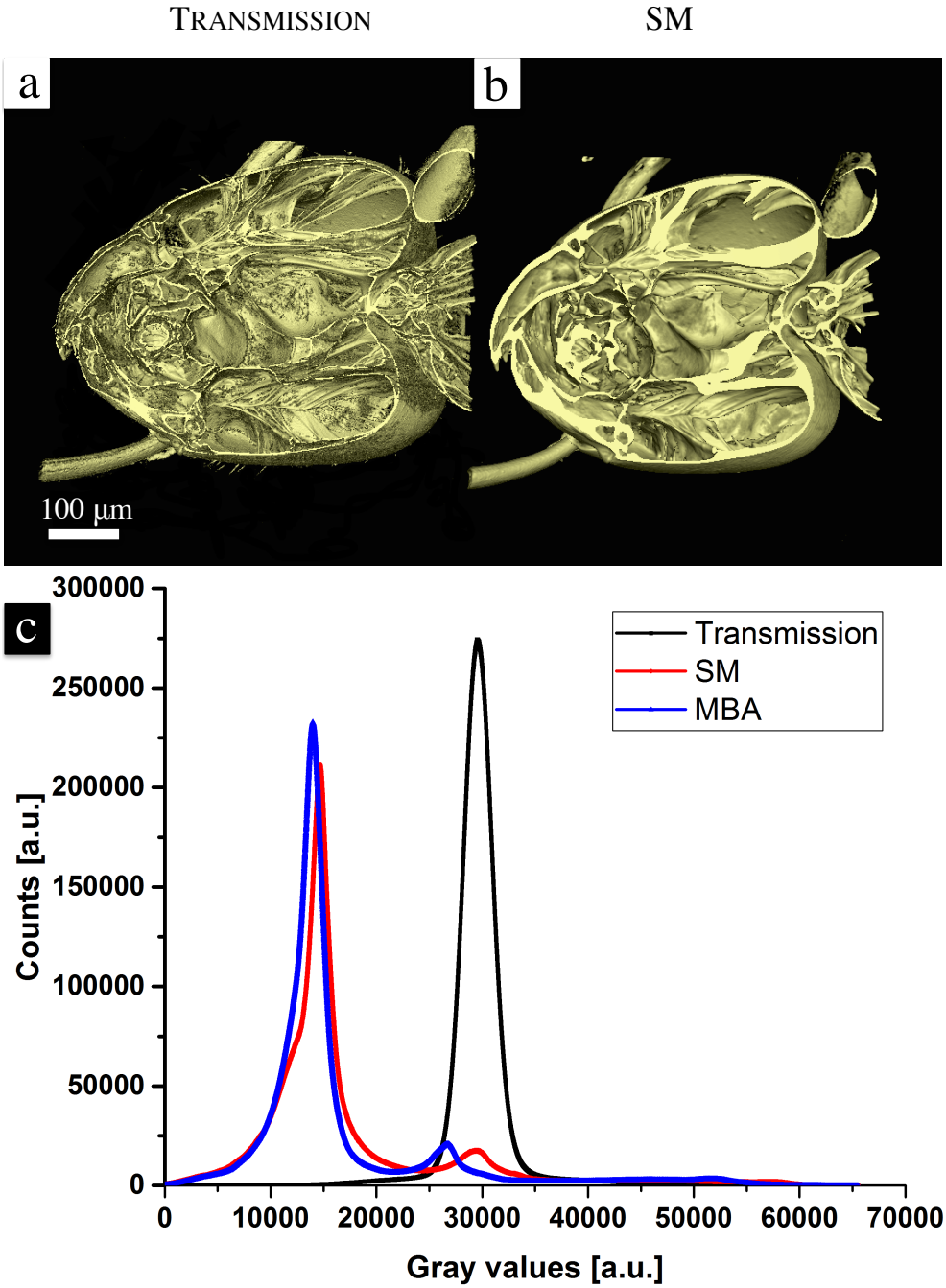

Figure 7.2: 3D models of the ant's head rendered using VGStudio Max. (a) This image illustrates a cut off through the transmission data revealing the inside of the head capsule. The image in (b) presents the data reconstructed using the single material algorithm. (c) The histograms show similar performances of the SM (red line) and MBA (blue line) compared to the transmission data (dark line).

7.1.4 Conclusion

This subsection has discussed the performance of two selected algorithms based on the TIE, namely the single material and the modified Bronnikov algorithms were chosen as proof of principle. The advantage of both algorithms lays in the increase of detail recognition in a "noisy" environment. However, their limit is evidenced by the smoothing that can utterly wipe out some details in the sample. As a perspective, a demonstrated alternative to solve this inconvenience would be the Bronnikov aided correction (section 3.3.1) [De Witte et al., 2009] or the post-processing method [Wernersson et al., 2013] that is meant to reduce the phase effect in raw data already reconstructed through FBP.

7.2 Tomography of a seed

7.2.1 Motivation

The structure of the endosperm plays a major role during seeds germination. Therefore, specific seeds such as Arabidopsis (*Arabidopsis thaliana*) and its close relative Lepidium (*Lepidium sativum*) are used to explore the architecture of the endosperms [Lee et al., 2012]. Henceforward, various imaging modalities are employed, apart from the usual bright field microscopy. Nevertheless, several details regarding the anatomy and the weakening of the endosperms [Müller et al., 2006], as well as details of the dormancy mechanisms of these seeds remain unknown [Finch-Savage and Leubner-Metzger, 2006]. Using quantitative phase tomography with synchrotron light [Cloetens et al., 2006], the architecture of Arabidopsis could be revealed in a non-invasive manner. The intracellular void network revealed during this investigation highlighted the utility of X-ray tomography and phase-contrast imaging at sub-micron resolution in plant cell physiology. Since then, further studies were performed to track the development inside seeds using synchrotron radiation micro-computed tomography (SR-μCT) [Verboven et al., 2013]. Herewith, it is shown that results of similar quality of complex samples can be obtained, especially using commercially available systems, which eliminate the need to access synchrotron light sources.

7.2.2 Lepidium (*Lepidium sativum*)

Sample preparation

The samples probed in this section were procured as standard goods commercially available and did not require any specific treatment for μCT. However, a dissection was requested for the SEM scanning. Here, longitudinal and axial sections of the seeds were coated with a thin layer of Gold (Au) using the SCD 005 model of BAL-TEC Sputter Coater.

A description of the sample is given in Fig. 7.3. A parallel slice through the sample shown in the photograph (a) is schematically represented in (b). With an additional transverse scheme of the seed (c), the anatomy of the seed is viewed. According to structural similarities between Lepidium and Arabidopsis seeds [Müller et al., 2006], Fig. 7.3(a) and (b) were adapted from the description of the Arabidopsis seed performed in [Cloetens et al., 2006]. The diminutive words of the different components of the seed are interpreted in the caption.

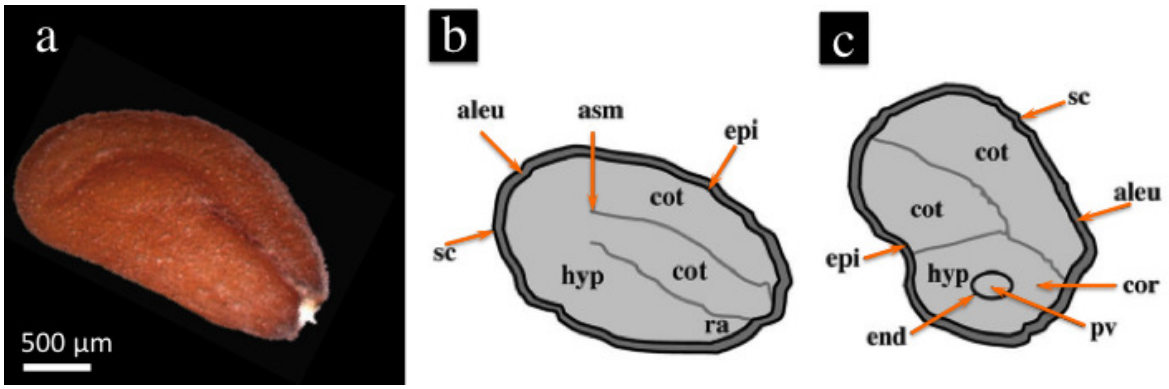

Figure 7.3: Description of Lepidium seeds. (a) Photograph of a Lepidium seed (adapted from [Müller et al., 2006]). Scheme of a longitudinal slice (b) and a transverse slice through the seed (c), showing its architecture. Due to the similar architecture of Lepidium and Arabidopsis seeds, (b) and (c) are adapted from the description of a seed of *Arabidopsis* as communicated in [Cloetens et al., 2006]. The diminutive words may be understood as follows: aleu, aleuron; cot, cotyledon; hyp, hypocotyl; ra, radicle; asm, apical shoot meristem; sc, seed coat; cor, cortex; end, endodermis; epi, epidermis; pv, provasculature.

Experiment and data analysis

A seed of Lepidium was glued on top of a thin pipe and subjected to the scan at the dedicated setup. For the sample of approximately 500 µm in diameter to remain entirely in the FOV offered by the detector, an effective pixel size of 1.35 µm was reached. Here again, an acceleration voltage of 40 kV and a power of 3 W was assigned to the scan. The MBA and the SM were applied assuming the sample to be made of Triticin (saccharose–$C_{12}H_{22}O_{11}$ of a density 1.59 g/cm^3), though it might contain multiple ingredients. The respective phase retrieval parameters for a 13.15 keV energy of the beam were α = 1.35e-06, and $\frac{\delta}{\beta}$ = 550. It is intentionally intended to observe the outcome of these common algorithms, with the aim of deducing pleasing results on a biological heterogeneous sample measured in our device. The samples prepared for SEM were scanned on the scanning electron microscope JEOL JSM-6060LV.

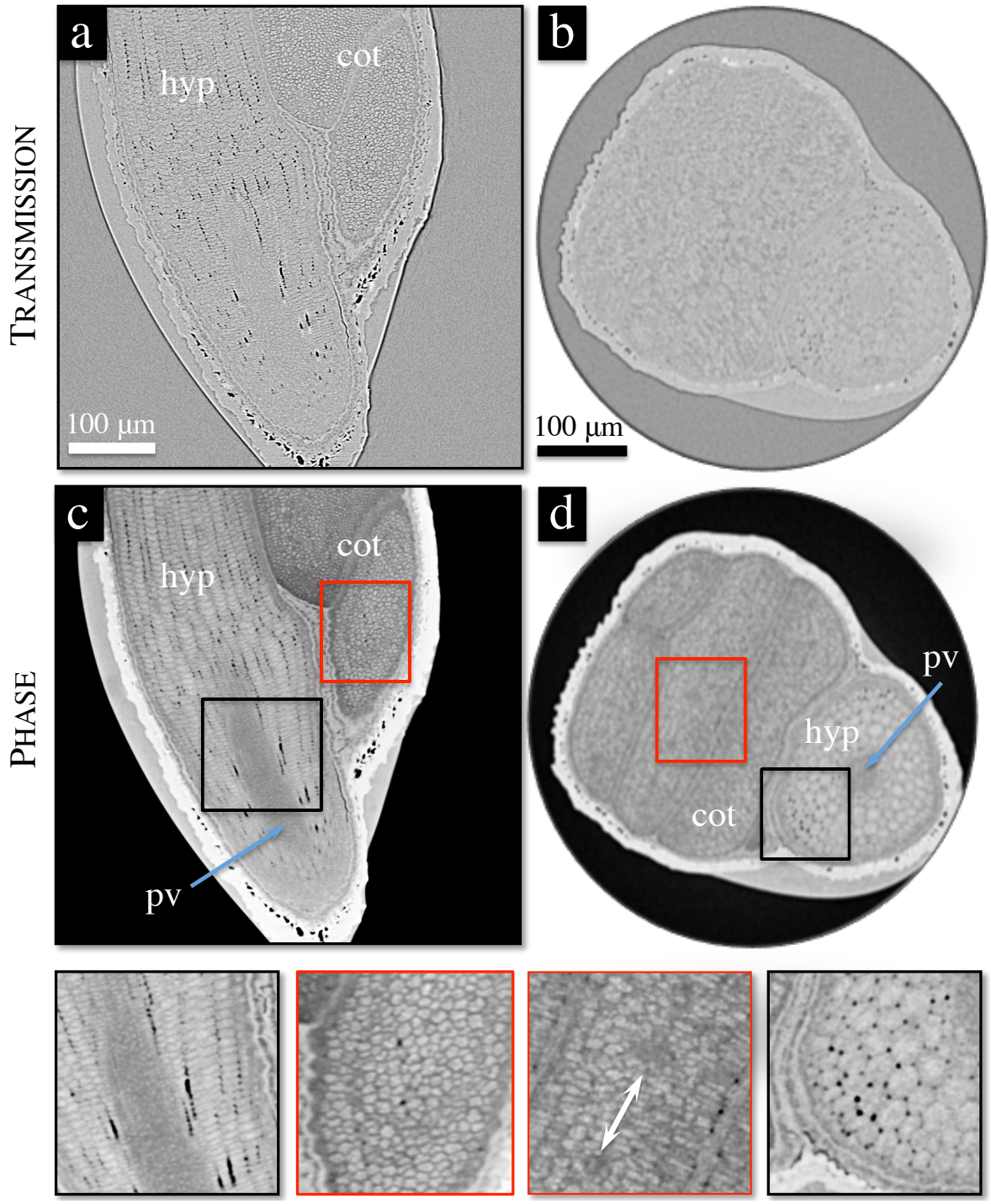

Figure 7.4: 2D slices across a lepidium seed assessed by µCT. (a) Sagittal and (b) axial slices of the reconstructed µCT data. (c) and (d) correspond to the reconstruction of (a) and (b) using the single material algorithm. Colored frames are zoomed to the row below. All-important units are abbreviated as follows: hyp, hypocotyl, cot, cotyledon, pv, provasculature. The zoom in the red frame of (d) indicates grey areas, which will be later demonstrated as vascularization.

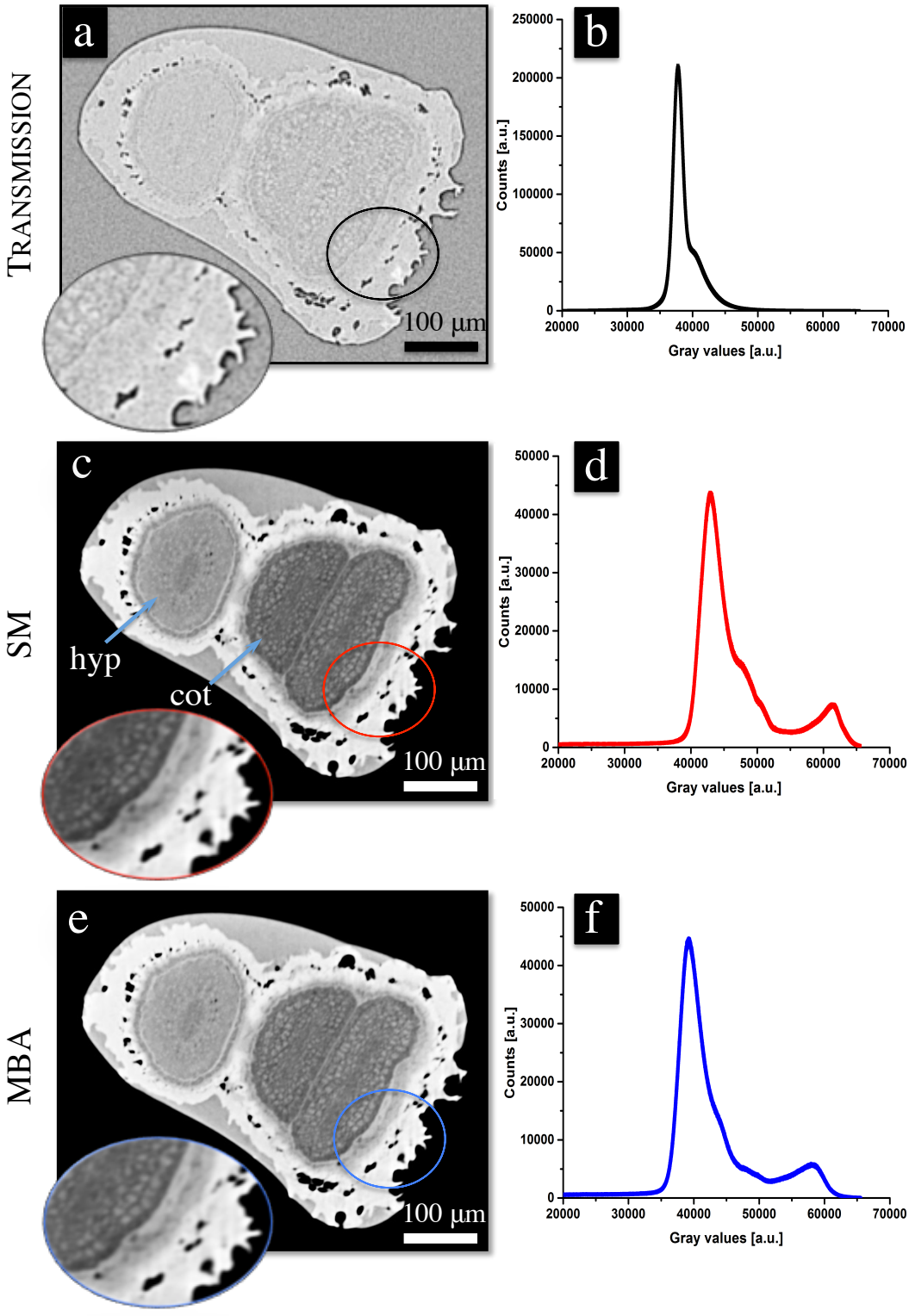

Figure 7.5: Display of the performance of different algorithms applied on the seed of lepidium. Cross section through (a) the transmission data, (c) the data reconstructed using the SM, (e) the data reconstructed using the MBA. Their corresponding histograms are plotted on the right in (b), (d) and (f), respectively.

Results and discussion

Figures 7.4(a) and (b) show sagittal and transverse tomograms of the Lepidium seed. These tomograms were selected from the mixed phase and amplitude data, which is impacted by the effect of edge enhancement. In their corresponding phase tomograms shown in Fig 7.4(c) and (d), various details in the internal morphology of the seed have been highlighted by the fact that

- in Fig. 7.4(c) the individual layers of the epiderm are revealed,
- the endodermis is pronounced with a provasculature (pv) in its middle, compared to Fig. 7.4(a)
- in Fig. 7.4(d) the cotyledons as well as the hypocol (hyp) are demarcated perfectly as they could be observed in bright field microscopy [Müller et al., 2006].

The magnification of the regions framed in Figs. 7.4(c) and (d) gives prominence to the interpretations made above. Moreover, the system has enabled with a ps_{eff} = 1.35 µm a clear outline of the air voids supplied to the hypocol and the cotyledons as demonstrated only by studies at synchrotron facilities [Cloetens et al., 2006]. The arrows indicated in the last row of Fig. 7.4 indicate light dark areas in a cotyledon, which could be considered artifacts but will be demonstrated later as determining features of the seed's morphology at this stage. Three main messages are conveyed in the following. At first, the interpretations mentioned above bear the advantage of phase retrieval on data from specimens measured in phase contrast mode in this X-ray microscope.

With the transverse slice displayed in Fig. 7.5, the MBA and SM still show clearly, even by visual appreciation, a similar performance of both phase retrieval algorithms. Here the contrast is drastically superior to transmission tomogram (Fig. 7.5(a), (c), (e)). This assertion is supported by separate peaks in the histograms of the data obtained after phase retrieval (Fig. 7.5(d) and (f)) compared to the transmission data (Fig. 7.5(b)). The second aspect conveyed is, therefore, the accomplishment of various phase-retrieval procedures.

As a third communication, the outcome of the sample investigated by scanning electron microscopy (SEM) in Fig. 7.6 provides sustenance for the methodology of phase-contrast imaging performed in this work. The morphology of the epiderm and the regular alignment of the cells in the cotyledon are well depicted by SEM in Fig. 7.6(a). However, additional items have been observed in a phase tomogram, where a better contrast and more features have been unveiled (Fig. 7.6(b)). A SEM slice into the hypocotyl of the specimen exhibit the known trapezoidal shape of its cells arranged concentrically around the endodermis (Fig. 7.6(c)). In a similar phase tomogram (Fig. 7.6(d)), the contrast between the endodermis and the cells has been substantially extended and the architecture of the air voids that border each cell could be noticed.

Figure 7.7 shows a 3D rendering of the seed of Lepidium reconstructed by using a phase map calculation performed on the recorded projections before to the FBP. Individual cotyledons as well as the hypocotyl are shown as separate components in the internal morphology of the seed (Fig. 7.7(a)). The aforementioned light dark areas in the bottom row of Fig. 7.4 are revealed here as regular patterns organized as a chain along the middle line of each cotyledon (see xy-planes in Fig. 7.7(a)). Cotyledons of *Arabidopsis* are most influential in

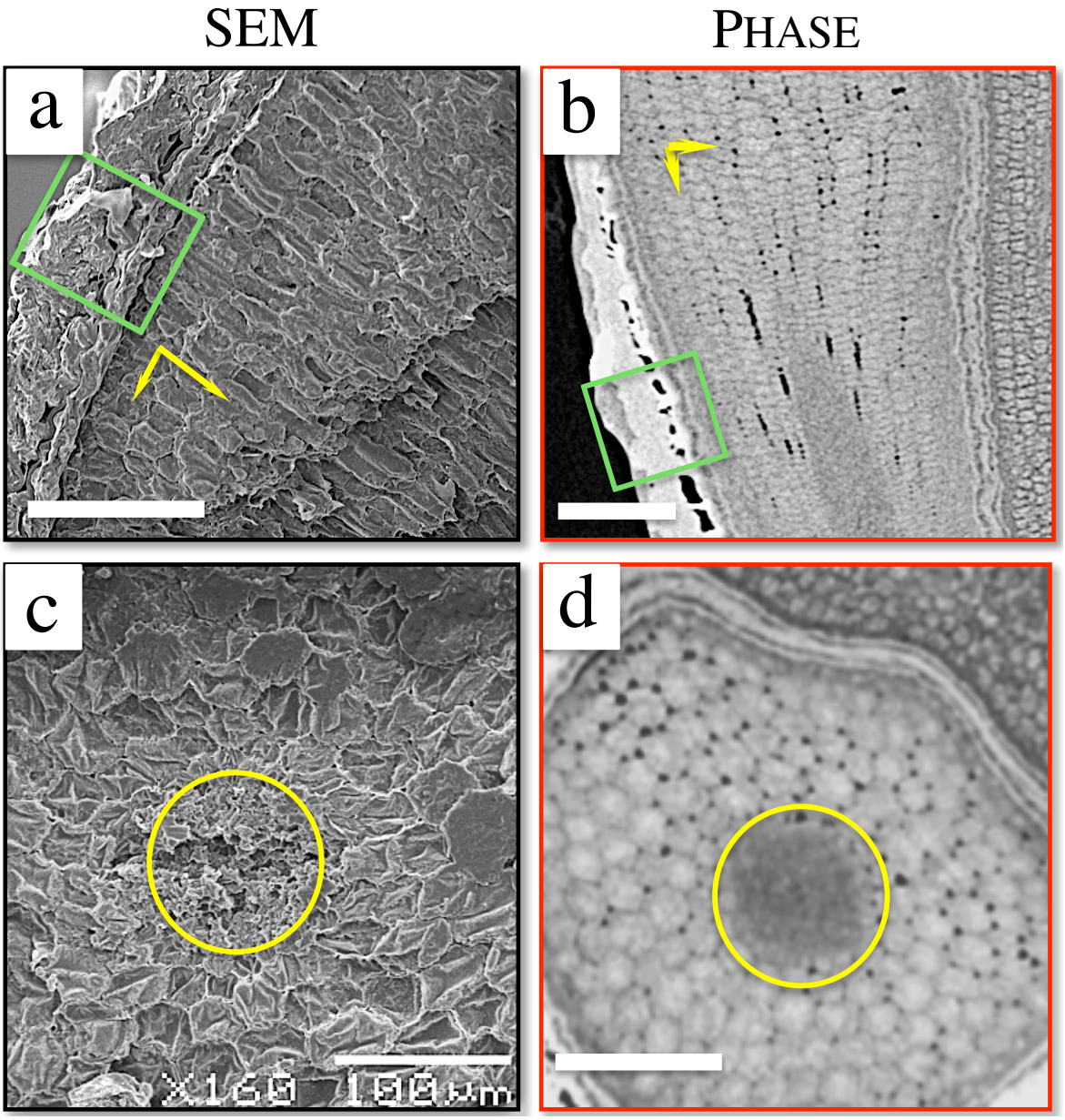

Figure 7.6: Comparison between a Lepidium samples inspected by scanning electron microscopy (SEM) and the sample reconstructed by SM. (a) Lepidium as imaged by SEM showing the arrangement of the radicle in columns (see arrows). This is compared to the phase image (b), where the testa and the endosperm are better detected than in SEM (see green frames). (c) and (d) represent axial views into the radicle of lepidium seeds issued from SEM and SM phase reconstruction, respectively. The circles include the provasculature of the endodermis. The trapezoidal cells of the hypocotyl and the endodermis are clearly distinguished in the phase tomogram. Scale bar: 100 µm.

the investigation of the developmental anatomy of the seed's embryo. With the use of dissecting microscopy, distinct arrangements of the vascular patterns were shown in the leafy

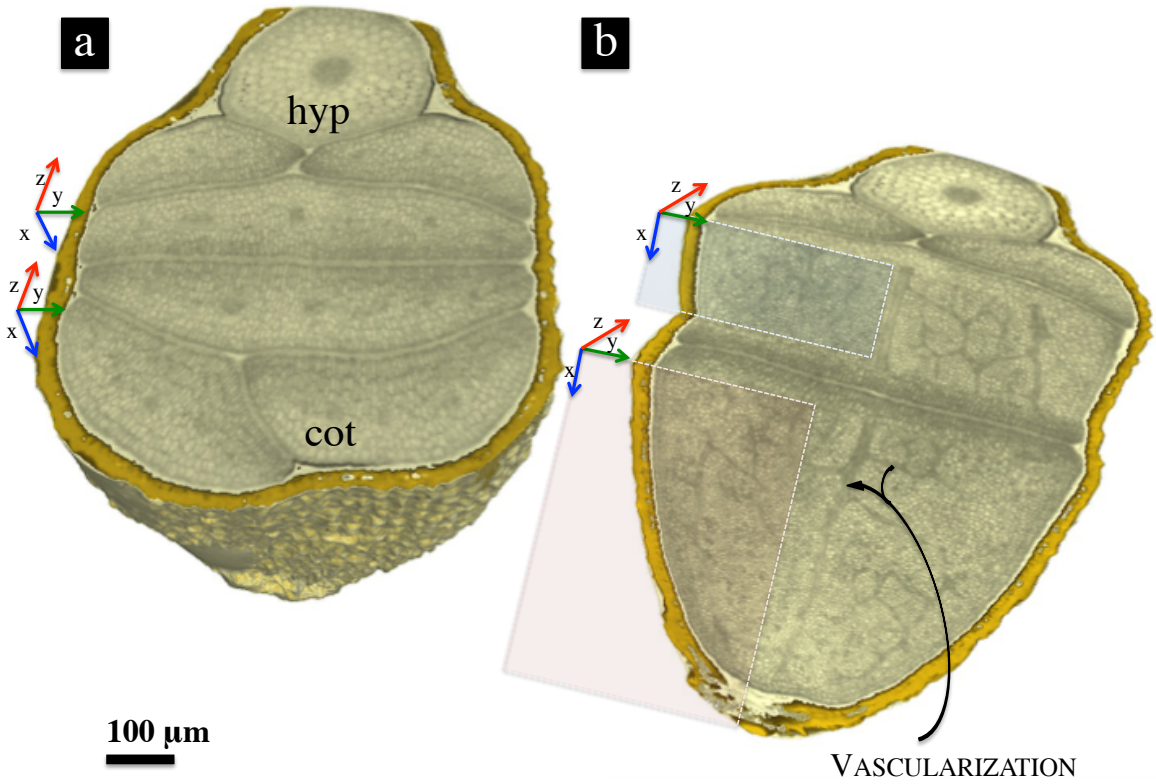

Figure 7.7: 3D rendering of the lepidium seed showing in the cross section the hypocotyl and the cotyledons (a). The xy-planes illustrated in (a) cut mainly cross light dark areas, which are revealed in (b) to be vascularization in cotyledons. (b) A step cutting crosses different cotyledons and shows vein patterns in each of the xy-planes.

cotyledons of various species of *Arabidopsis* [Meinke, 1992, Janošević et al., 2007]. These vascular differentiations were asserted to begin at the appearance of an elongated tissue made of cytoplasmically dense cells [Esau et al., 1965, Carland et al., 1999]. This early stage was already observed in the cotyledon of a dissected seed of Arabidopsis [Meinke et al., 1994]. Based on the data processing that has been undertaken in this work, the visualization of the vascularization in the cotyledons of *Lepidium sativum* is warranted. A step cutting along the xy-planes illustrated in Fig. 7.7(b) displays vein patterns identifiable as vascular bundles in leafy cotyledons.

7.2.3 Conclusion

It has been shown in this section that for a complex biological object such as a seed of Lepidium, the edge enhancement produced by phase contrast is insufficient to detect all the details contained in the specimen. Phase-retrieval methods have been demonstrated to improve the contrast in these object. In fact, the choice of this specimen relied on its extent of interest in plant physiology, especially in the examination of seeds germination. Phase-retrieval methods are known to perform efficiently in the presence of noise, but here, they were demonstrated to improve the contrast on the mixed biological sample. This finding es-

tablishes the usability of the phase-retrieval procedure in multiple purposes, and suggests the implementation of this methodology aiming at practical use in advanced laboratory systems.

7.3 Tomography of composite materials

In this section, persuasive employment of X-ray microscopic imaging in the investigation of composite materials is discussed. The benefit of phase contrast and phase retrieval for the characterization of these materials is highlighted.

7.3.1 Motivation

An accurate knowledge of the orientations of fibrous rigid materials included in polymer matrixes is important in material science, in order to improve their physical and mechanical properties. These matrixes include multiple additives like resins and fillers aiming to reduce the weight (non functional fillers) or to fulfil a specific task (functional fillers) [Kia, 1993]. As an example, sheet molding compounds (SMC) have gained importance mainly in lightweight construction due to their flexibility and cost efficiency [Orgéas and Dumont, 2012, Palmer et al., 2010]. Besides mechanical testing, which can predict some material properties, three-dimensional imaging of samples is required to determine the relative distribution and local orientation of fibers [Czabaj et al., 2014, Whitacre and Czabaj, 2015]. Hence, a net contrast between the fibers and components of the investigated sub-volume is indispensable.

With a non-commercial device, single-distance phase-contrast imaging was demonstrated to be promising for the evaluation of structural materials with the aid of epoxy and aluminium alloys [Zoofan et al., 2006]. In this perspective, several material composites such as carbon fibers, aluminium composite materials were also characterized by using commercial machines [Kastner et al., 2012a, Kastner et al., 2012b], and the edge enhancement resulting from phase shift was proven to emphasize the contrast for effective segmentation. Beyond its use in the characterization of materials, this effect is also applied for testing segmentation algorithms through comparisons between computational results and those that are experimentally observed [Czabaj et al., 2014]. Nevertheless, using SMC as an example of a composite sample containing fibers and granular fillers, the contrast could remain low despite the edge enhancement. The phase-retrieval method is demonstrated here to considerably increase the contrast in composite material specimens.

7.3.2 Sheet molding compound

Description of the sample and experiment

The sheet molding compound is the best example of reinforced and filled polymers and finds frequent usage in transportation, construction and appliances [Kia, 1993]. The sample investigated in this work has a dimension of ≈ 1 cm in diameter and is built of resin, glass fibers and alumina trihydrate also designated as aluminium hydroxide–$\mathrm{Al(OH)_3}$. The latter is a filler that aims to reduce the weight of the compound but has a functional property as a flame retardant.

Experiment and data analysis

The scan was performed at a tube voltage of 60 kV, and with a ps_{eff} = 0.96 µm. The sample dimension is obviously large above the FOV of almost 1 mm (1024 × 0.96 µm). Accordingly, the sample was scanned in a zoomed modality, commonly known as local tomography. The phase retrieval procedures presented in the following are restrained to the SM and the MBA, which have been performed respectively with a $\frac{\delta}{\beta}$-ratio = 199 and the regularization term α = 8.e-03.

Results and discussion

The transverse slice of the transmission data (Fig. 7.8(a)) shows a low contrast. The results obtained by applying the SM and MBA phase-retrieval operation display visually in Figs. 7.8(b) and (c) an improvement in the contrast, which is concretely witnessed to the well-structured histograms in Figs. 7.8(e) and (f) compared to Fig. 7.8(d).

The sagittal layer, exposed in Fig. 7.9(a), gives a little overview of the positioning of fibers in the composite material. In comparison, the corresponding slice derived from the reconstruction through phase retrieval in Fig. 7.9(b) raised the discrimination between the fibers and the additives, particularly in the selected region. These regions selected from Fig. 7.9(a) and (b) are enlarged in Fig. 7.9(c) and (d), and are used to express in an explicit manner the role played here by the phase retrieval. The horizontal line profiles (left to right) and the vertical (up to down) in the latter figures in the graphs of Figs. 7.9(e) and (f) indicate that the granular fillers and the fibrous structures are clearly defined in a less noisy environment, when the data is processed via a phase retrieval algorithm.

The production process of SMC requires several characteristics of each component to be procured. Fillers may then have a certain size and distribution [Kia, 1993]. The fibers may rather need to form a strand or bundle and keep this orientation after compounding, in order to ensure a dimensional stability. This state is however complicated to maintain, so that the 3D rendering shown in Fig. 7.10(a) represents a satisfactory achievement with the processing performed in this work. The directions as well as the bonding of the filaments have been ideally detected by simple thresholding (Figs. 7.10(b)–(d)).

Though the choice of this kind of specimen is only based on its mixed composition, the type of its constituents matters with regard to the contrast achieved in order to track the orientation of the fibers. Considering chalk–$CaCO_3$ of density 2.71 g.cm^{-3} as a prevalent filler in SMC, its contrast to glass fibers i.e., SiO_2 of density 2.65 g.cm^{-3} is low in X-ray attenuation imaging. With reference to the index of refraction from [Henke et al., 1993], this outcome is quite conceivable, and an advisable solution is phase-contrast microtomography [Le et al., 2008]. While still referring to the index of refraction of the fillers, $Al(OH)_3$ of density 2.42 g.cm^{-3} might reveal better contrast to SiO_2 with increasing photon beam energy in attenuation imaging. Consequently, the contrast formation based on attenuation imaging may not be optimal for the specimen studied in this section, which has been scanned with an average energy of E_{av}= 13.15 keV. Hence, a low contrast is issued in the transverse slice of the transmission data (Fig. 7.8(a))

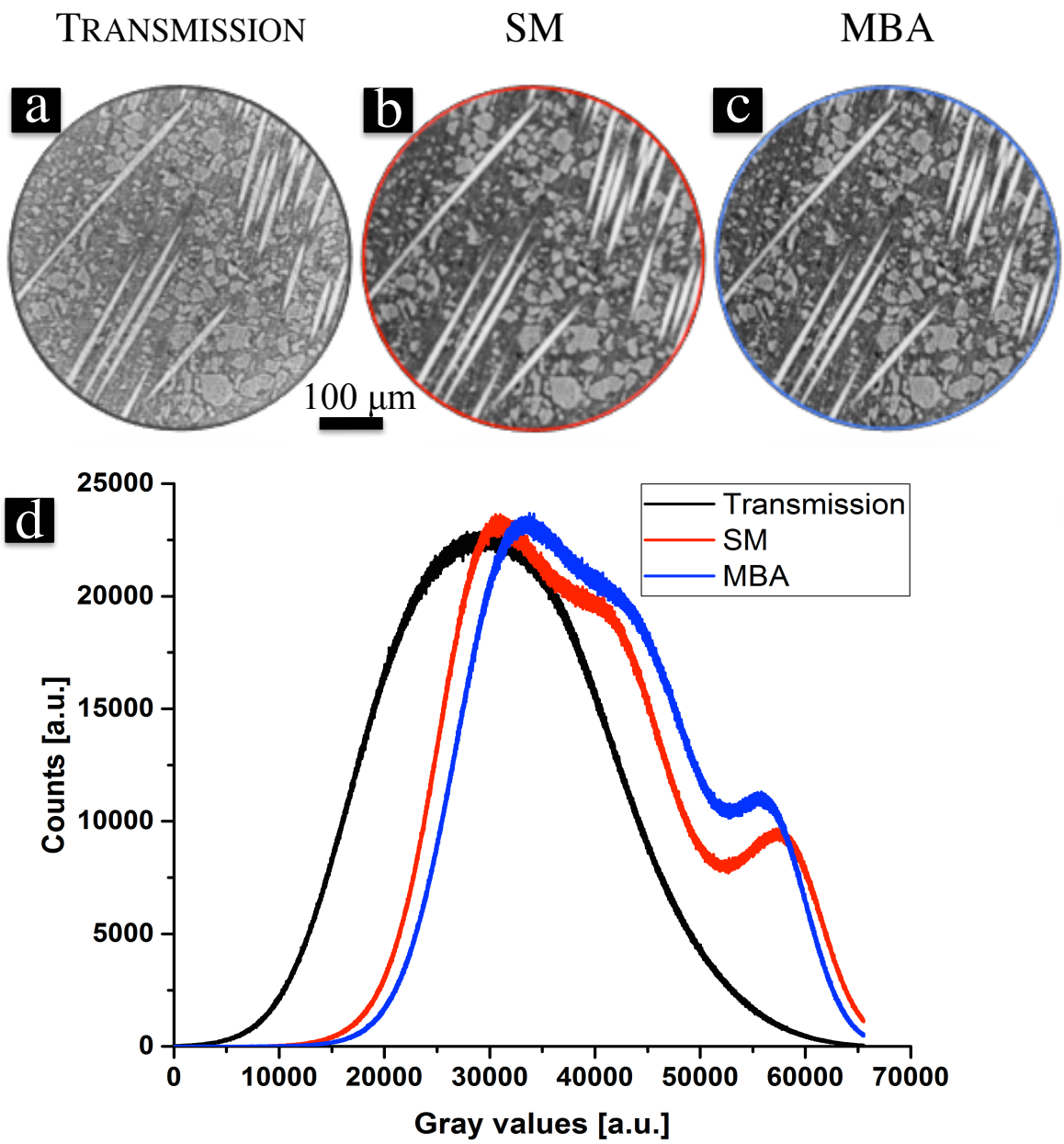

Figure 7.8: 3D reconstructed slices from transmission and phase of the sheet molding compound (SMC). (a) Transverse slice from a simple reconstruction with the FBP. (b) and (c) Corresponding slices reconstructed using a phase map calculation with the SM and MBA, respectively. (d) Histograms of the data shown in (a)–(c).

7.3.3 Conclusion

The use of phase-contrast imaging and tomography at research laboratory systems in order to produce solely edge-enhanced images has procured benefits in the study of a variety of materials [Mayo et al., 2012, Kastner et al., 2006, Zoofan et al., 2004]. Phase retrieval has increasingly gained importance by improving the results of tomographic reconstructions and

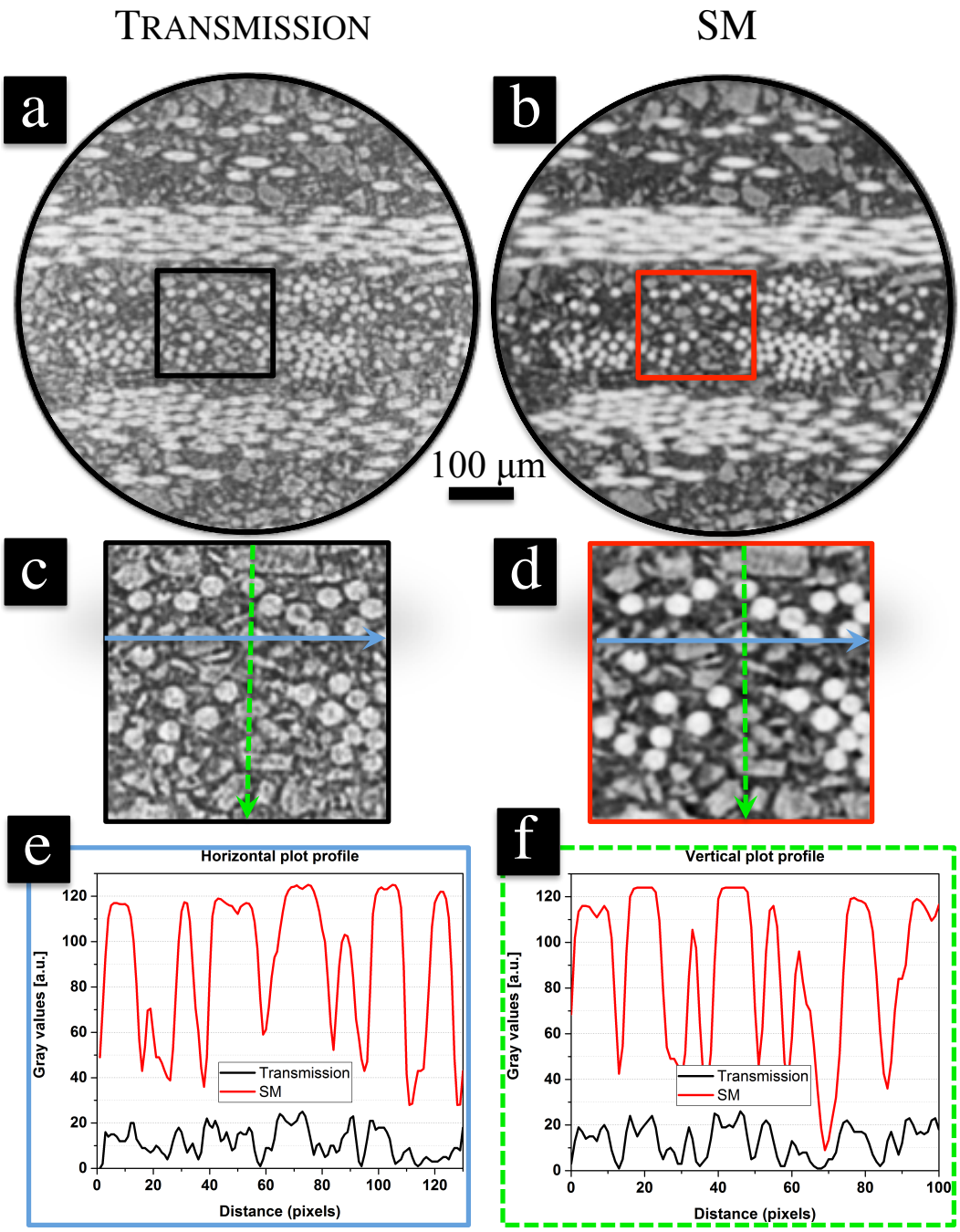

Figure 7.9: Explicit comparison between the transmission data (a) and the data derived from phase retrieval (b). The regions selected in previous images are highlighted in (c) and (d). Focus is set on the horizontal and vertical lines in both images. The horizontal plot profiles are displayed in (e), while the vertical profiles are shown in (f). In the latter graphs the contrast is shown as emphasized in the phase-retrieved data, where the fibers are clearly higher than the additives.

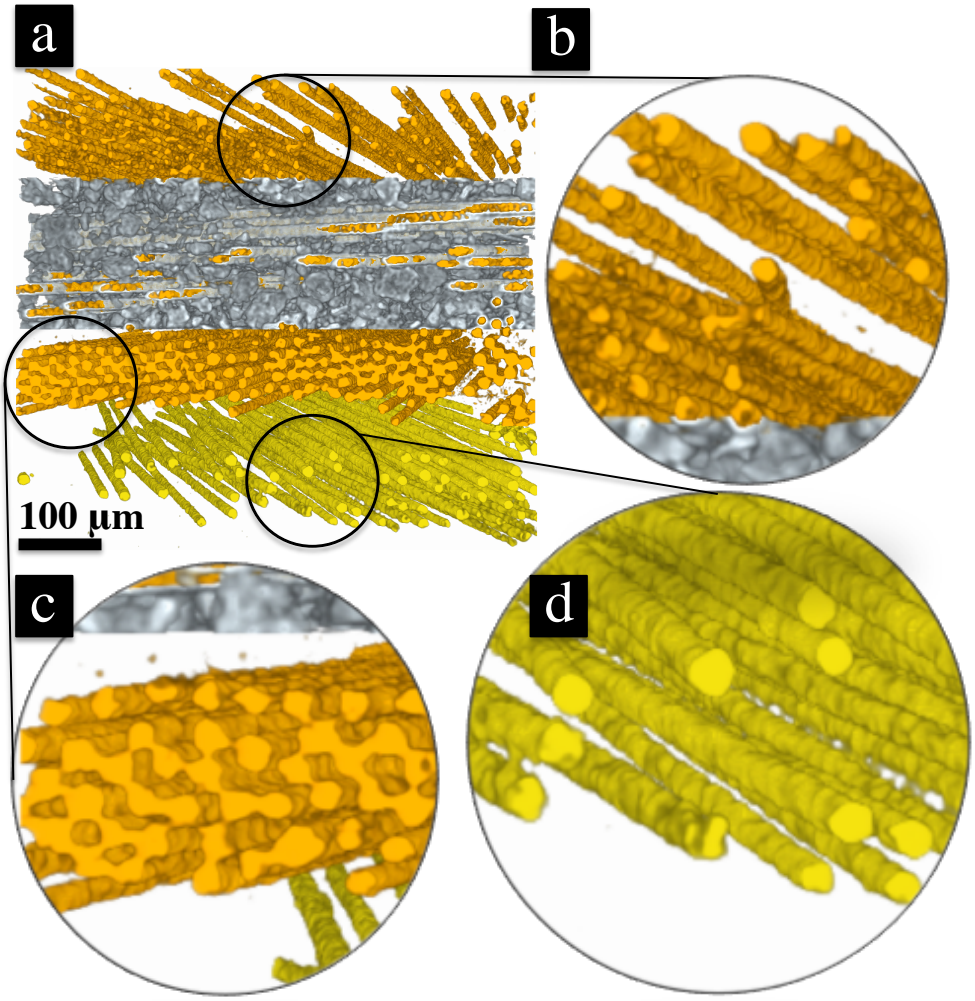

Figure 7.10: 3D rendering of the data processed using the phase retrieval. (a) A segmentation by simple thresholding has permitted the visualization of the orientation of the fibers (orange and yellow) included in the granular mass of fillers (grey). (b)–(d) show the state of the fibers basically meant to form a bound.

procuring extensive contrast [Mayo et al., 2003]. It has been proven in this section with the case study of a sheet molding compound, that this procedure is effectively an asset. Although these results have been reproduced on several samples such as carbon fibers composites and aluminium compounds ($AlSi_{12}$, Al_2O_4), this SMC sample is shown here as an example. Hence in our opinion, this methodology is worth being incorporated in the development of future laboratory systems optimized for phase-contrast imaging.

7.4 Imaging of a muscle fascicle in inverse geometry

7.4.1 Motivation

Skeletal muscles of mammals are hierarchically composed of numerous fascicles of heterogeneous muscle fibers [Schiaffino and Reggiani, 2011] (see Fig. 7.11). The number of muscle fibers per fascicle determines the size and the shape of the muscle that, in turn, reflect the diversity of its function [MacIntosh et al., 2006]. Some muscles, including the jaw muscles possess atypical fibers. The structural and functional arrangements of these muscle fibers differ among species, and imply a direct relationship with their lifestyle and diet [Schiaffino and Reggiani, 2011]. In this context, it was expected to elucidate the substructural anatomy of the sample presented in this section.

7.4.2 Muscle fascicle of a mammal

Sample description

A muscle fascicle from the jaw of a mammal was used as an exemplary sample to demonstrate the task in this section. It is made of several muscle fibers, which have a dimension of about a few tenths of a micrometer. For conservation purposes, it has been air-dried, but in so doing, it reached a stable state that should also benefit to a μCT scan. The specimen was provided for the purposes of a research collaboration with the "Max-Planck-Institut für evolutionäre Anthropologie (Leipzig)".

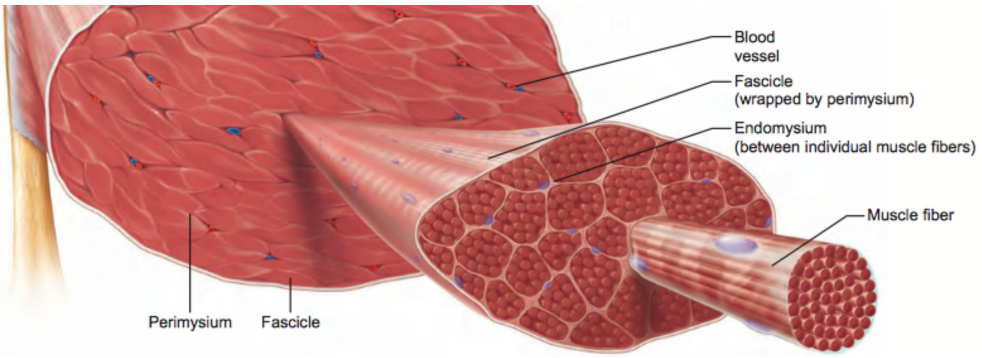

Figure 7.11: Structural architecture of a skeletal muscle. The muscle fascicles are of variable size, but within a range of few tenths of a micrometer. Image adapted according to [Hutchinson, 2007].

Experimental

For the sake of reliability of the comparison of images taken in high geometric magnification and in the inverse geometry setting, the exposure time for each acquisition was set at an arbitrary value of 5000 counts/pixel. This resulted in an acquisition times of 7 s and 29 s, respectively.

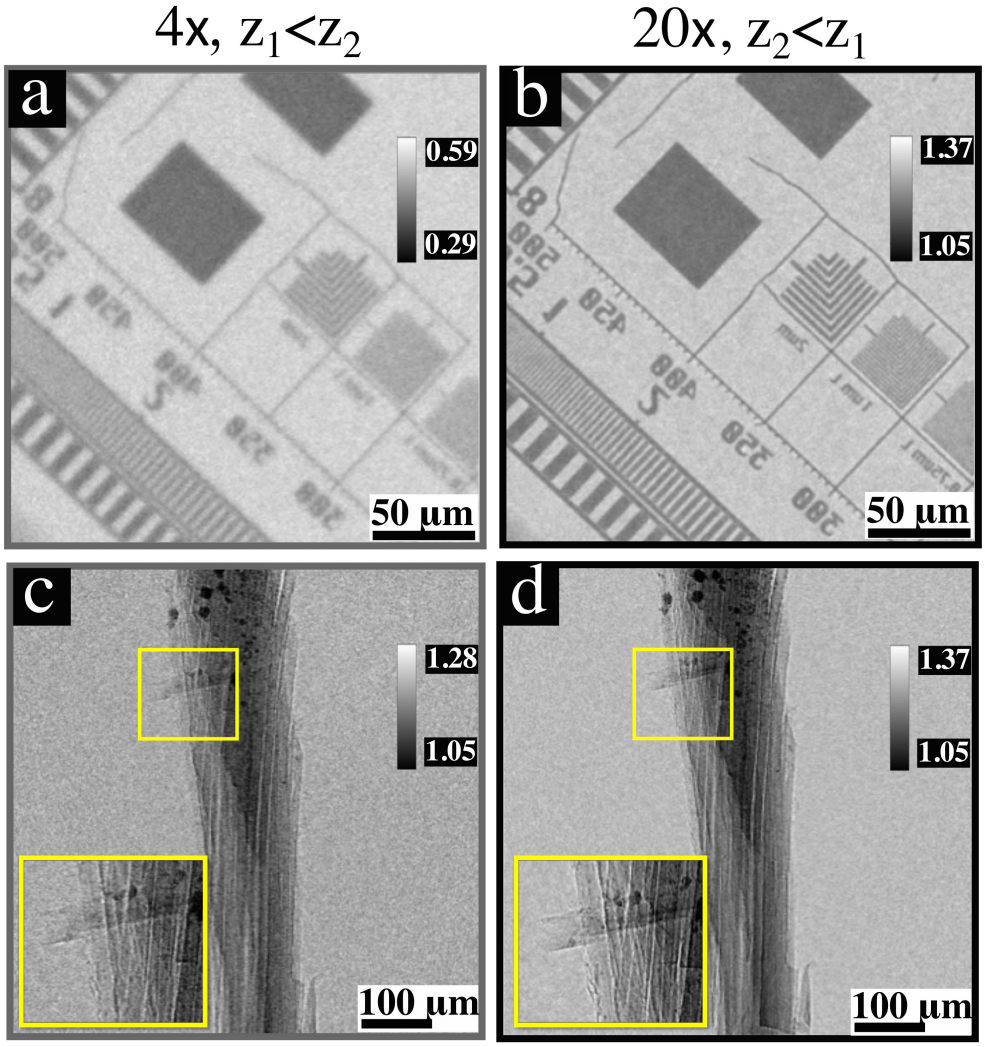

Figure 7.12: Effect of the lateral source dimension and the detector PSF on the spatial resolution. (a) Influence of the source extension while using a high geometric magnification ($M_{\text{geom}} = 7$). (b) The effect of the detector PSF shows an improvement of the spatial resolution in a setting using low geometric magnification ($M_{\text{geom}} = 1.41$). The Xradia calibration pattern is used in both images. (c) and (d) are projections of a mammal muscle in the respective settings of (a) and (b). The stronger edge-enhancement is clearly observed in the zoomed region.

Results and Discussion

By applying 40 kV and 3 W, projections of an Xradia calibration pattern were accordingly recorded as displayed in Figs. 7.12(a) and (b). Projections of the muscle sample recorded with the parameters of Figs. 7.12(a) and (b) are respectively given in Figs. 7.12(c) and (d). Compared to Fig. 7.12(c), the optimization of the spatial resolution is expressed by a more pronounced edge-enhancement in Fig. 7.12(d), (zooms).

The optimization of the spatial resolution through geometrical mounting allowed to re-

solve some structures of $\approx$ 1.5 µm in the inverse geometry. We may reconsider here the relation between the system point spread function and the geometric magnification formulated in Eq. 2.1. From this equation, it is obvious that for low magnifications ($M_{\text{geom}} \rightarrow 1$), the system's resolution is importantly influenced by the detector PSF ($\sigma_{\text{sys}} \approx \sigma_{\text{det}}$). This relation states as $\sigma_{\text{sys}} = (0.074 + 0.5\sigma_{\text{det}})^{1/2}$ according to the inverse geometry configuration with M_{geom} = 1.41, and a $\text{FWHM}_{\text{src}} = 2\sqrt{2\ln 2} \cdot \sigma_{\text{src}}$ = 1.8 µm. Consequently, the spatial resolution is enhanced through a small detector point spread function and there might be a specific geometric setting where the spatial resolution of the imaging system is optimized for a given σ_{src} and σ_{det} of the source and detector, respectively. This is achieved when the first derivative of the system standard deviation expressed as function of the geometric magnification equals zero, i.e., $\sigma'_{\text{sys}}(M_{\text{geom}}) = 0$ (see Eq. 8.8, Appendix A.2). It follows the relation

$$M_{\text{min}} = 1 + \left(\frac{\sigma_{\text{det}}}{M_{\text{opt}} \cdot \sigma_{\text{src}}}\right)^2 = 1 + \left(\frac{\text{FWHM}_{\text{det}}}{M_{\text{opt}} \cdot \text{FWHM}_{\text{src}}}\right)^2, \tag{7.1}$$

where M_{min} denotes the optimal magnification to achieve the best spatial resolution. Considering the image resolution measurements proceeded in section 5.2.1, it is reminded that the detector PSF was measured at a source-to-object distance of 191.7 mm and an object-to-detector distance of 4.56 mm, resulting in a geometric magnification $M_{\text{geom}} \approx 1$. Using a 20$\times$ objective, an effective pixel size ps_{eff} = 1.35 µm was reached and the measured FWHM_{det} yielded a value of 2.9 µm. Analogously, the FWHM_{src} measured for M_{geom} = 7 was 1.8 µm under the tube conditions of the experiments performed in section 5.3.4. Based on these parameters and using Eq. 7.1, the optimal geometric magnification is obtained as $M_{\text{min}} = 3.5$. Thus, an explanation of a better spatial resolution in the inverse geometry where $M_{\text{geom}} = 1.41$ is given in comparison to the setting that involves a high geometric magnification $M_{\text{geom}} = 7$.

In parallel, it has been shown here that phase-retrieval algorithms derived from the contrast transfer function also work perfectly on data produced in this laboratory system. Therefore, two phase-retrieval algorithms designated as Fourier methods by Rytov and Born (see section 3.3.2) have been used in addition to the modified Bronnikov algorithm. With a regularization parameter α = 2.5e-03 for the MBA and α = 1.5e-02 for the Fourier methods, the phases were retrieved on an identical projection, which was acquired in a high geometric magnification $M_{\text{geom}} = 7$ (see Figs. 7.13(a), (c) and (e)), and in a low one i.e., the inverse geometry setting (see Figs. 7.13(b), (d) and (f)). It is demonstrated for each applied algorithm that the inverse geometry setting in this system improves both the phase-contrast imaging and the sharpness of the phase-retrieved images.

Influence of the geometry on the tomographic reconstruction

Several issues during CT acquisition can lead to artifacts in the resulting reconstruction, such as mechanical instabilities that can cause sample drifts or the stability of the X-ray source. For CT-acquisition in ZEISS Xradia 500 Versa, the most probable cause of artifacts in tomographic reconstruction is a sample drift caused by thermal fluctuations within the device [xra, 2011]. It manifests itself as overall observed unsharpness or streaks at tomograms' edges. Moreover, the occurrence of these artifacts increases with higher resolution and long scan

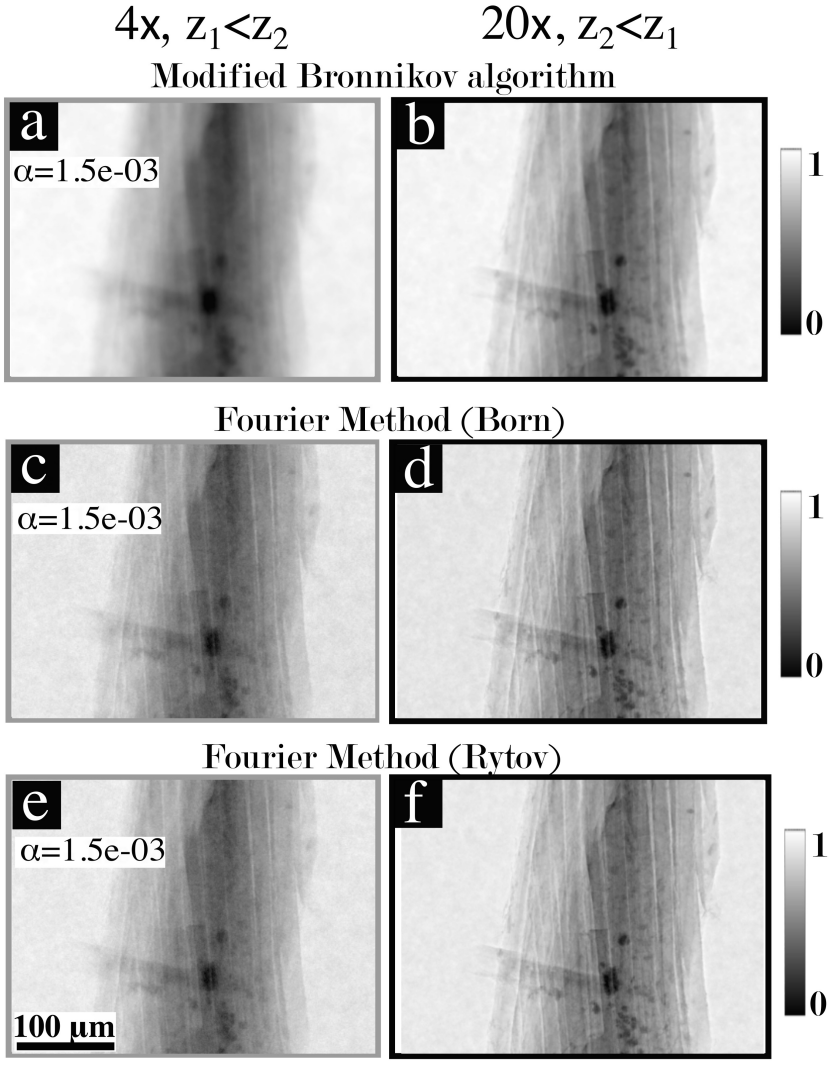

Figure 7.13: Effect of the optimization of the spatial resolution on the phase retrieval. (a), (c) and (e): Three phase-retrieval algorithms, namely the modified Bronnikov algorithm, the Fourier method by Born and Rytov have been applied on a projection acquired with a geometrical magnification of $M_{\text{geom}} = 7$, compared to the projection acquired with the inverse optimized geometry (b), (d) and (f). The latter phase-retrieved images show an improvement in sharpness. For each of the methods, α denotes the regularization parameter.

periods, where the temperature changes about 1–2°C.

Considering the fact that these drifts become severe with high resolution and during long tomographic acquisition scans, the attempt of phase-contrast imaging with this device is imminently subject to reconstruction artifacts for the following reasons:

- In this system, it is desired to perform the imaging modality at high resolution.
- Large propagation distances Z_{eff} may be required to observe pronounced edge enhancement and therefore, long acquisition periods would be required to achieve reasonable signal-to-noise ratio.

Although a **Thermal Drift Correction** algorithm is applicable during the reconstruction process with the customary reconstruction software "XMReconstructor" of the device [xra, 2011], it is frequent to observe some remains of these artifacts in high resolution imaging. As the phase retrieval on data collected with the apparatus is proceeded offline, it is of concern to establish a reliable workflow for tomographic reconstruction of phase-contrast and phase-retrieved images.

The graph of Fig. 7.14(a) demonstrates the temperature fluctuations measured in the imaging system during both scans of the muscle sample performed by acquiring 1601 projections in the low- (dark plot) and high-magnification geometries (red plot). The latter scan suffered less from thermal fluctuation as the measurement was conducted in a time period 4-fold shorter than the first scan. Accordingly, the FBP reconstruction of the long period scan using an in-house implemented library[1] displays a selected tomogram importantly corrupted with artifacts (see Fig. 7.14(b)). Despite the low thermal fluctuation recorded during the shorter scan period, some minor artifacts were still observed (see Fig. 7.14(c)).

Solving tomographic reconstruction artifacts

A post-processing of output data from commercial devices is usually critical. However, the ".txrm" and ".txm" files of ZEISS Xradia 500 Versa were made exploitable through a python implementation[1], and the data were aligned using an algorithm[2] based on the tomographic consistency communicated by [Guizar-Sicairos et al., 2015]. Fundamentally, the tomographic consistency denotes the fact that:

"the inverse Radon transform by FBP followed by a Radon transform only retrieves the original sinograms if they are consistent with a 3D representation"

— [Guizar-Sicairos et al., 2015].

Therefore, a synthetic sinogram is used to iteratively correct the proper sinogram and thus the positions of the misaligned projections. This process was repeated in 5 iterative steps in the case of the muscle sample and resulted in a better reconstruction in Figs. 7.14(d)–(i). The transmission tomograms obtained from the FBP after alignment are displayed in Figs. 7.14(d) and (g), and show clear edge enhancement, although the reconstruction of the high magnification data still shows minor streaks. These are remedied by applying the phase retrieval as shown in the phase tomograms of Figs. 7.14(e) and (f), where the MBA and the Fourier method by Born were considered with the same parameters specified in Fig. 7.13 (α = 2.5e-03 and 1.5e-03, respectively). If combined with the phase reconstructed slice of the high magnification data (Figs. 7.14(h) and (i)), it is conclusive that the phase retrieval improved the contrast in the anatomy of the muscle fibers examined in this work.

7.4.3 Conclusion

In this section, the geometric optimization of the phase-contrast imaging by involving the detector PSF has been demonstrated with ZEISS Xradia 500 Versa. The different available

[1] The algorithm was implemented by Andreas Fehringer, E17 (TUM).
[2] This algorithm was implemented and put at disposal by Sebastian Allner, E17 (TUM).

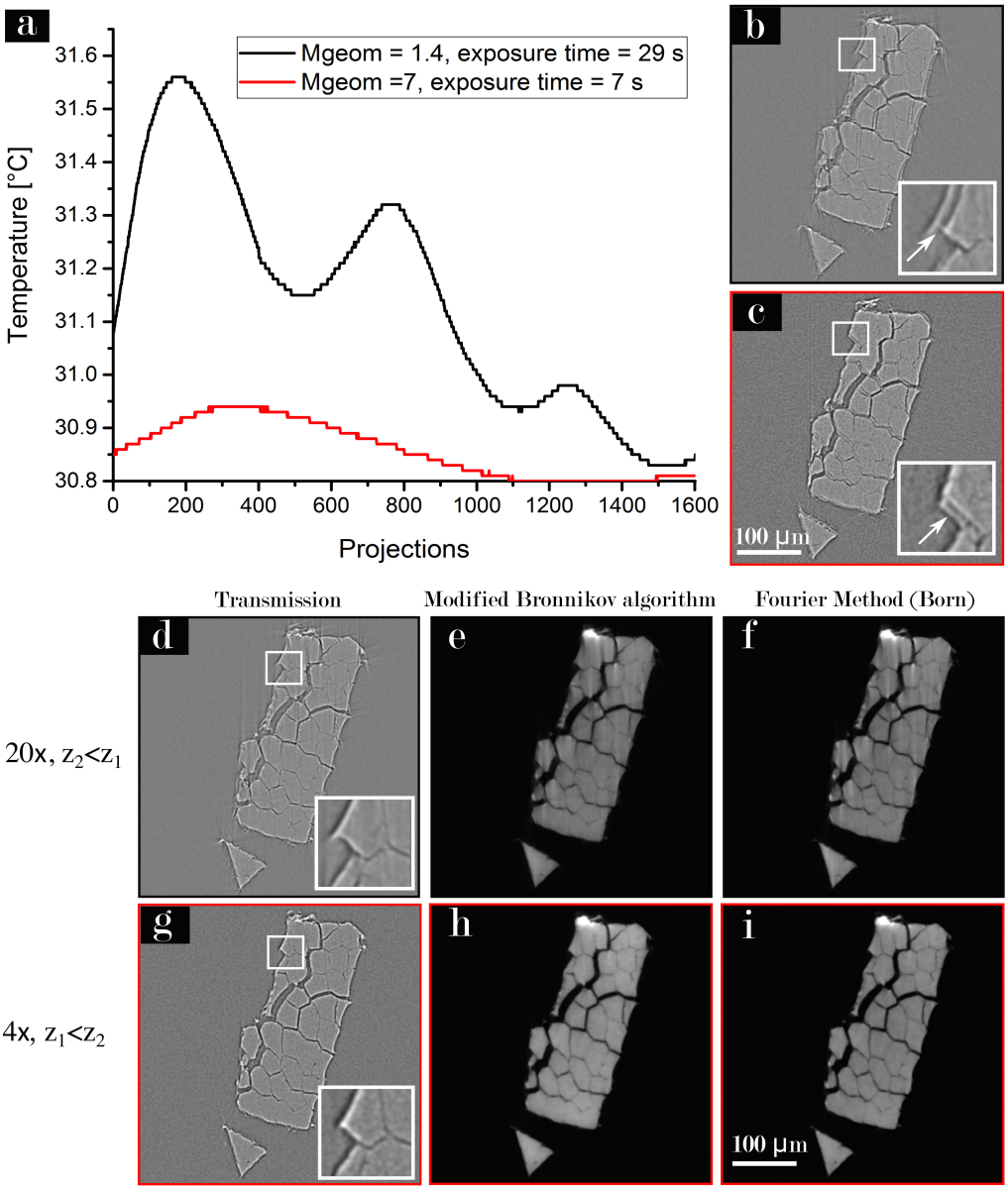

Figure 7.14: Influence of the thermal drift on the 3D reconstruction and phase-contrast imaging. (a) Illustration of temperature fluctuations during high-resolution scans performed in long-(dark plot) and short periods (red plot), corresponding respectively to the low magnification (M_{geom} = 1.41) and high magnification settings (M_{geom} = 7), where the first is also denoted as inverse geometry setting. Equivalent slices of the 3D reconstruction by FBP of each of these scans show artifacts in (b) and (c). The alignment of the projections by means of tomographic consistency gives a significant improvement of the reconstruction in (d) and (g), resulting in edge enhancement in the phase-contrast tomograms. Additionally, the phase-retrieval operation on both images using the MBA ((e) and (h)) and the Fourier method by Born ((f) and (i)) present an accessible structural anatomy of the mammal jaw muscle.

objectives of the device (4× and 20×), enabled a comparison between high geometric magnification (M_{geom} = 7) and low geometric magnification (M_{geom} = 1.41), both with the same effective pixel size. Henceforth, the minimization of the source blurring and the optimization of the spatial resolution through the detector PSF have been clearly demonstrated on the phase-contrast images as well as the phase-retrieved images. It has been shown that the pre-alignment of the projection images with the tomographic consistency approach compensates for reconstruction artifacts arising from the misalignment of the sample, which appear with a high probability during long phase-contrast acquisitions. At our knowledge, the work performed in this section shows for the first time the concrete application of phase-contrast imaging together with phase retrieval in an optimized spatial resolution mode (inverse geometry) in a commercial µCT system. However, if priority is attributed to the scan time, a possibility to intensify the effect of edge enhancement is to apply a deconvolution algorithm on the projections, which is presented in Appendix A.1.

Chapter 8

Conclusions and perspectives

This chapter reviews the outcome of the goals set in the motivation of this PhD thesis, and an evaluation of the scientific contribution is presented.

The work reported in this dissertation has been motivated by the necessity to inspect the properties of two advanced laboratory devices dedicated for X-ray imaging in order to understand their performance and examine their capabilities to accomplish new imaging techniques. We are aware that these equipments are specifically designed to assist the scientific or industrial community to carry out experiments on opaque samples, whether soft (biological) or strongly absorbing. Therefore, some pertinent case studies using the standard capabilities of the advanced laboratory devices: v|tome|x s 240 and ZEISS Xradia 500 Versa, were presented in sections 6.2 and 6.3.1. These sections demonstrate the combination of microscopic X-ray imaging with other techniques such as contrast enhancement protocols for soft tissues and neutron powder diffraction – to answer distinct inquiries.

Contributions of this thesis

X-ray imaging and staining procedures In section 6.2, experimental mice lungs were imaged with superior contrast, which would not have been possible without staining procedures [Metscher, 2009b, Metscher, 2009b]. By providing contrast as good as in histology, the three dimensionality of the X-ray µCT supported the investigation of tumor-burden lungs in carcinogenesis studies. The combination of staining protocols with X-ray attenuation-based imaging enabled, on one hand, the depiction of burdens from the tissues in the diseased lungs and, on the other hand, the quantification of these burdens by segmentation. However, undesired effects such as inflammations could not be clearly discerned from the tumors. Nevertheless, it is believed that progressive advances in the establishment of staining protocols that enable better diffusion of contrast agents (e.g., [Vasilescu et al., 2012, e Silva et al., 2015]) or binding of the agents to specific type of tissues would overcome this drawback, and thus allow very precise quantification of the burdens. These results have been submitted for publication in Nature Scientific Report ([Bidola et al., 2016a]).

X-ray imaging and neutrons diffraction imaging An essential contribution of µCT at medium resolution carried out on v|tome|x s 240 to help elucidate, in combination

with neutron powder diffraction, the current distribution in Li-ion cells [Senyshyn et al., 2015] has been reported in section 6.3.1. This work is part of a list of studies conducted to understand the running and safety disorders of the batteries, which have gained importance in energy storage recently. The short review in this section is dedicated to a simple usage of commercial advanced laboratory systems, but is of great importance.

Dual-energy μCT The dual-energy CT is routinely used in clinical applications but has been explored with ZEISS Xradia 500 Versa (section 6.3.2), to demonstrate its functionality on composite material samples, especially at higher resolution. Therefore, it is known here as dual-energy μCT. At the present device, this imaging technique was used to study a particularly complex sample with the intent to resolve relatively small compounds contained in the specimen: a gold ore sample. Consequently, the analysis of the X-ray beam spectra at various energies was required. It should be mentioned that the procedure used in this study can also be performed on any other laboratory system provided with a large range of tube voltages.

Characterization of the devices One of the most important goals of this thesis concerns the investigation of the capabilities of the aforementioned systems to enable the use of imaging techniques within a laboratory setting which have, until recently, only been possible at large synchrotron facilities. Emphasis has been placed on the single-distance propagation-based phase-contrast imaging, which obviously requires a (partial-) coherent beam and a range of resolution depending on the sample size. Therefore, determining the source size of the laboratory devices is a prerequisite, especially for cone-beam geometries.

Smaller beam spot sizes are required for achieving a coherent X-ray beam (Eq. 3.39), however, the transmission tube in v|tome|x s 240 was found to have an abnormally wide spot size (section 4.3) which is detrimental for the application of PCI. Deconvolution techniques are suggested as a solution (Appendix A.1) but they are ineffective for excessive blurring (section 5.3.2, Eq. 5.6).

Investigation of the single-distance phase-contrast imaging The investigation of the single-distance propagation-based phase-contrast imaging was performed in chapter 5 in ZEISS Xradia 500 Versa using the 4× and 20× magnifications built in the detector assembly. Here, the source sizes for various parameters of the transmission tube were thoroughly investigated and reported (section 5.2.1). The methodical scheme to understand phase-contrast imaging in this system with reliable applications was covered in section 5.3. These results have been published in [Bidola et al., 2015b]. This chapter concludes with the limitation of the present imaging technique with this device, i.e., the inspection of relatively small objects due to the restrained geometry of the apparatus.

Deconvolution is often used to reduce the blurring induced by a finite spot size in standard lab systems equipped with motionless source and detector. However, the device ZEISS Xradia 500 Versa incorporates a movable source and detector which allow the so-called inverse geometry setting presented in section 5.3.3. Besides optimization

of the spatial resolution, this geometry provides enhanced phase contrast without the need of the aforementioned deconvolution. This setting benefits from a long source-to-object distance compared to the object-to-detector in order to minimize the blurring of the finite source size on the recorded image. To compensate for the low geometric magnification, which may imply a low imaging pixel size, a high-resolution detector is required. Hence, the 20× objective of the detector assembly provided in the device (ZEISS Xradia 500 Versa) allowed us to demonstrate this advantage.

Demonstration of practical applications of the single-distance phase-contrast imaging Beyond the demonstration of the feasibility of the single-distance phase-contrast imaging, its usefulness for a commercial system is shown with effective experiments that have been conducted on representative samples. In chapter 7, a few applications of phase-contrast tomography and phase retrieval are reported on biological samples: an arthropod (section 7.1), a seed (section 7.2); and on composite material samples (section 7.3). Presented results are accepted for publication in the Journal of Microscopy ([Bidola et al., 2016b]). In section 7.4, a skeletal muscle fascicle of a mammal has been studied with superior phase contrast by applying the inverse geometry setting.

Although this represents a first achievement using a compact commercial system, the long scan time required gives rise to severe thermal drifts which subsequently lead to corrupted tomographic reconstruction. With regards to this drawback, a solution has been suggested, namely the tomographic consistency (section 7.4.2).

Perspectives

Propagation-based phase contrast imaging The motion provided to each of the components in the system ZEISS Xradia 500 Versa could allow the acquisition of phase-contrast images with the same effective pixel size at several distances. In section 3.3, the phase-retrieval algorithms adapted for single-distance phase-contrast images, due to the usual stationary source and detector in cone-beam geometry systems have been presented. It is believed that the degree of motion built in the present device could enable the retrieval of the phases directly using the transport-of-intensity equation (Eq. 3.33). Nonetheless, a correction for the misalignment shown schematically in Fig. 5.5 must be applied.

Phase retrieval Commercial systems such as the ZEISS Xradia 500 Versa that are able to provide phase contrast can benefit greatly, in terms of image quality, by the application of the phase retrieval algorithms presented in this dissertation. This would open up several application areas for these devices where absorption contrast is not sufficient to resolve the structures of interest such as in biology.

X-ray imaging of biological samples Interdisciplinarity is an absolute prerequisite to sustain advances in laboratory-based μCT. As an example, the results achieved in section 6.2 highlight the need for more accurate contrast agents, which would inherently improve the outcome of μCT.

Closing remarks

If the purpose of this work can be briefly thought of as the study of laboratory systems in order to expand their imaging capabilities before turning to high-brilliance sources, success can be granted to the techniques investigated in this thesis, especially the single-distance propagation-based phase-contrast imaging (chapters 5 and 7).

Staining-based imaging of mouse lungs using laboratory setups has been presented as a promising alternative to synchrotron radiation [Liu et al., 2010, Stahr et al., 2016, Dullin et al., 2015] for conducting preclinical studies on similar types of samples. This represents a significant step exceeding the usual abilities of laboratory equipments.

Bibliography

[xra, 2011] (January 2011). VersaXRM-500 User's Guide. Zeiss Xradia.

[Alanentalo et al., 2008] Alanentalo, T., Loren, C. E., Larefalk, Å., Sharpe, J., Holmberg, D., and Ahlgren, U. (2008). High-resolution three-dimensional imaging of islet-infiltrate interactions based on optical projection tomography assessments of the intact adult mouse pancreas. Journal of biomedical optics, 13(5):054070–054070.

[Alic et al., 2011] Alic, L., Haeck, J. C., Bol, K., Klein, S., van Tiel, S. T., Wielepolski, P. A., de Jong, M., Niessen, W. J., Bernsen, M., and Veenland, J. F. (2011). Facilitating tumor functional assessment by spatially relating 3d tumor histology and in vivo mri: image registration approach. PLoS One, 6(8):e22835.

[Als-Nielsen and McMorrow, 2011] Als-Nielsen, J. and McMorrow, D. (2011). Elements of modern X-ray physics. John Wiley & Sons.

[Alvarez and Macovski, 1976] Alvarez, R. E. and Macovski, A. (1976). Energy-selective reconstructions in x-ray computerised tomography. Physics in medicine and biology, 21(5):733.

[Amunts et al., 2013] Amunts, K., Lepage, C., Borgeat, L., Mohlberg, H., Dickscheid, T., Rousseau, M.-É., Bludau, S., Bazin, P.-L., Lewis, L. B., Oros-Peusquens, A.-M., et al. (2013). Bigbrain: an ultrahigh-resolution 3d human brain model. Science, 340(6139):1472–1475.

[Andor, nd] Andor, O. I. (n.d.). -100 degree deep-cooled ccd for large area imaging. http://www.andor.com/pdfs/specifications/Andor_iKon-L_936_Specifications.pdf. Accessed: 2017-01-18.

[Attwood, 2007] Attwood, D. (2007). Soft x-rays and extreme ultraviolet radiation: principles and applications. Cambridge university press.

[Banhart, 2008] Banhart, J. (2008). Advanced tomographic methods in materials research and engineering. Oxford University Press Oxford.

[Bartels, 2013] Bartels, M. (2013). Cone-beam x-ray phase contrast tomography of biological samples: Optimization of contrast, resolution and field of view, volume 13. Universitätsverlag Göttingen.

[Bartels et al., 2013] Bartels, M., Hernandez, V. H., Krenkel, M., Moser, T., and Salditt, T. (2013). Phase contrast tomography of the mouse cochlea at microfocus x-ray sources. Applied Physics Letters, 103(8):083703.

[Bech, 2009] Bech, M. (2009). X-ray imaging with a grating interferometer. PhD thesis, University of Copenhaguen.

[Bech et al., 2010] Bech, M., Jensen, T. H., Bunk, O., Donath, T., David, C., Weitkamp, T., Le Duc, G., Bravin, A., Cloetens, P., and Pfeiffer, F. (2010). Advanced contrast modalities for x-ray radiology: Phase-contrast and dark-field imaging using a grating interferometer. Zeitschrift fuer medizinische Physik, 20(1):7–16.

[Behling, 2015] Behling, R. (2015). Modern Diagnostic X-Ray Sources: Technology, Manufacturing, Reliability. CRC Press.

[Betz et al., 2007] Betz, O., Wegst, U., Weide, D., Heethoff, M., Helfen, L., LEE, W.-K., and Cloetens, P. (2007). Imaging applications of synchrotron x-ray phase-contrast microtomography in biological morphology and biomaterials science. i. general aspects of the technique and its advantages in the analysis of millimetre-sized arthropod structure. Journal of Microscopy, 227(1):51–71.

[Bidola et al., 2016a] Bidola, P., e Silva, J., Achterhold, K., Munkhbaatar, E., Jost, P., Meinhardt, A.-L., Taphorn, K., Zdora, M.-C., Pfeiffer, F., and Herzen, J. (2016a). A step towards valid detection and quantification of lung cancer volume in experimental mice with contrast agent-based x-ray microtomography. Nature Scientific Report, submitted.

[Bidola et al., 2016b] Bidola, P., Morgan, K., Willner, M., Fehringer, A., Allner, S., Prade, F., Pfeiffer, F., and Achterhold, K. (2016b). Application of sensitive, high-resolution imaging at a commercial lab-based x-ray micro-ct system using propagation-based phase retrieval. Journal of Micrsocopy, accepted.

[Bidola et al., 2015a] Bidola, P., Stockmar, M., Achterhold, K., Pfeiffer, F., Pacheco, M. L., Soriano, C., Beckmann, F., and Herzen, J. (2015a). Absorption and phase contrast x-ray imaging in paleontology using laboratory and synchrotron sources. Microscopy and Microanalysis, 21(05):1288–1295.

[Bidola et al., 2015b] Bidola, P. M., Zanette, I., Achterhold, K., Holzner, C., and Pfeiffer, F. (2015b). Optimization of propagation-based phase-contrast imaging at a laboratory setup. Optics express, 23(23):30000–30013.

[Bonse and Hart, 1965] Bonse, U. and Hart, M. (1965). An x-ray interferometer. Applied Physics Letters, 6(8):155–156.

[Boone, 2013] Boone, M. (2013). New imaging modalities in high resolution X-ray tomography. PhD thesis, Universiteit Gent.

[Boone et al., 2009] Boone, M., De Witte, Y., Dierick, M., Van den Bulcke, J., Vlassenbroeck, J., and Van Hoorebeke, L. (2009). Practical use of the modified bronnikov algorithm in micro-ct. Nuclear Instruments and Methods in Physics Research Section B: Beam Interactions with Materials and Atoms, 267(7):1182–1186.

[Born and Wolf, 2000] Born, M. and Wolf, E. (2000). Principles of optics: electromagnetic theory of propagation, interference and diffraction of light. CUP Archive.

[Bronnikov, 2002] Bronnikov, A. V. (2002). Theory of quantitative phase-contrast computed tomography. JOSA A, 19(3):472–480.

[Burvall et al., 2011] Burvall, A., Lundström, U., Takman, P. A., Larsson, D. H., and Hertz, H. M. (2011). Phase retrieval in x-ray phase-contrast imaging suitable for tomography. Optics express, 19(11):10359–10376.

[Bushberg and Boone, 2011] Bushberg, J. T. and Boone, J. M. (2011). The essential physics of medical imaging. Lippincott Williams & Wilkins.

[Carland et al., 1999] Carland, F. M., Berg, B. L., FitzGerald, J. N., Jinamornphongs, S., Nelson, T., and Keith, B. (1999). Genetic regulation of vascular tissue patterning in arabidopsis. The Plant Cell, 11(11):2123–2137.

[CDC, nd] CDC (n.d.). Centers for disease control wonder on-line database, compiled from compressed mortality file 1999-2012. http://www.cdc.gov/nchs/data_access/cmf.htm. Accessed: 2017-01-18.

[Chapman et al., 1997] Chapman, D., Thomlinson, W., Johnston, R., Washburn, D., Pisano, E., Gmür, N., Zhong, Z., Menk, R., Arfelli, F., and Sayers, D. (1997). Diffraction enhanced x-ray imaging. Physics in medicine and biology, 42(11):2015.

[Cheon and Orsulic, 2011] Cheon, D.-J. and Orsulic, S. (2011). Mouse models of cancer.

[Cloetens, 1999] Cloetens, P. (1999). Contribution to phase contrast imaging, reconstruction and tomography with hard synchrotron radiation: principles, implementation and applications. PhD thesis, Vrije Universiteit Brussels.

[Cloetens et al., 1999] Cloetens, P., Ludwig, W., Baruchel, J., Van Dyck, D., Van Landuyt, J., Guigay, J., and Schlenker, M. (1999). Holotomography: Quantitative phase tomography with micrometer resolution using hard synchrotron radiation x rays. Applied physics letters, 75(19):2912–2914.

[Cloetens et al., 2006] Cloetens, P., Mache, R., Schlenker, M., and Lerbs-Mache, S. (2006). Quantitative phase tomography of arabidopsis seeds reveals intercellular void network. Proceedings of the National Academy of Sciences, 103(39):14626–14630.

[Cormack, 1963] Cormack, A. M. (1963). Representation of a function by its line integrals, with some radiological applications. Journal of applied physics, 34(9):2722–2727.

[Cormack and Hounsfield, 2011] Cormack, A. M. and Hounsfield, G. N. (2011). The nobel prize in physiology or medicine 1979. Nobelprize. org, 9.

[Craig, 1936] Craig, J. (1936). "tomography" report on a method of x-raying sections of the body. British Journal of Tuberculosis, 30(3):152–154.

[Czabaj et al., 2014] Czabaj, M., Riccio, M., and Whitacre, W. (2014). Three-dimensional imaging and numerical reconstruction of graphite/epoxy composite microstructure based on ultra-high resolution x-ray computed tomography. American Institute of Aeronautics and Astronautics SciTech.

[Dauguet et al., 2007] Dauguet, J., Delzescaux, T., Condé, F., Mangin, J.-F., Ayache, N., Hantraye, P., and Frouin, V. (2007). Three-dimensional reconstruction of stained histological slices and 3d non-linear registration with in-vivo mri for whole baboon brain. Journal of neuroscience methods, 164(1):191–204.

[De Chiffre et al., 2014] De Chiffre, L., Carmignato, S., Kruth, J.-P., Schmitt, R., and Weckenmann, A. (2014). Industrial applications of computed tomography. CIRP Annals-Manufacturing Technology, 63(2):655–677.

[de Crespigny et al., 2008] de Crespigny, A., Bou-Reslan, H., Nishimura, M. C., Phillips, H., Carano, R. A., and D' Arceuil, H. E. (2008). 3d micro-ct imaging of the postmortem brain. Journal of neuroscience methods, 171(2):207–213.

[De Marco, 2015] De Marco, F. (2015). Optimizing data processing for grating-based x-ray phase-contrast computed tomography. Master's thesis, Technische Universität München.

[De Witte et al., 2009] De Witte, Y., Boone, M., Vlassenbroeck, J., Dierick, M., and Van Hoorebeke, L. (2009). Bronnikov-aided correction for x-ray computed tomography. JOSA A, 26(4):890–894.

[Diemoz et al., 2012] Diemoz, P., Bravin, A., and Coan, P. (2012). Theoretical comparison of three x-ray phase-contrast imaging techniques: propagation-based imaging, analyzer-based imaging and grating interferometry. Optics express, 20(3):2789–2805.

[Doughty and Roth, 2012] Doughty, D. and Roth, E. P. (2012). A general discussion of li ion battery safety. Electrochemical Society Interface, 21(2):37–44.

[Dullin et al., 2015] Dullin, C., Larsson, E., Tromba, G., Markus, A. M., and Alves, F. (2015). Phase-contrast computed tomography for quantification of structural changes in lungs of asthma mouse models of different severity. Journal of synchrotron radiation, 22(4):1106–1111.

[Dunlop et al., 2011] Dunlop, J. A., Penney, D., Dalüge, N., Jäger, P., McNeil, A., Bradley, R. S., Withers, P. J., and Preziosi, R. F. (2011). Computed tomography recovers data from historical amber: an example from huntsman spiders. Naturwissenschaften, 98(6):519–527.

[e Silva et al., 2015] e Silva, J. M. d. S., Zanette, I., Noël, P. B., Cardoso, M. B., Kimm, M. A., and Pfeiffer, F. (2015). Three-dimensional non-destructive soft-tissue visualization with x-ray staining micro-tomography. Scientific reports, 5.

[Eastwood et al., 2014] Eastwood, D., Bradley, R., Tariq, F., Cooper, S., Taiwo, O., Gelb, J., Merkle, A., Brett, D., Brandon, N., Withers, P., et al. (2014). The application of phase contrast x-ray techniques for imaging li-ion battery electrodes. Nuclear Instruments and

Methods in Physics Research Section B: Beam Interactions with Materials and Atoms, 324:118–123.

[Elliott et al., 1981] Elliott, J., Dowker, S., and Knight, R. (1981). Scanning x-ray microradiography of a section of a carious lesion in dental enamel. Journal of microscopy, 123(1):89–92.

[Esau et al., 1965] Esau, K. et al. (1965). Vascular differentiation in plants.

[Fernández et al., 2014] Fernández, R., Kvist, S., Lenihan, J., Giribet, G., and Ziegler, A. (2014). Sine systemate chaos? a versatile tool for earthworm taxonomy: non-destructive imaging of freshly fixed and museum specimens using micro-computed tomography. PloS one, 9(5):e96617.

[Feser et al., 2008] Feser, M., Gelb, J., Chang, H., Cui, H., Duewer, F., Lau, S., Tkachuk, A., and Yun, W. (2008). Sub-micron resolution ct for failure analysis and process development. Measurement science and technology, 19(9):094001.

[Finch-Savage and Leubner-Metzger, 2006] Finch-Savage, W. E. and Leubner-Metzger, G. (2006). Seed dormancy and the control of germination. New Phytologist, 171(3):501–523.

[Finegan et al., 2015a] Finegan, D. P., Scheel, M., Robinson, J. B., Tjaden, B., Hunt, I., Mason, T. J., Millichamp, J., Di Michiel, M., Offer, G. J., Hinds, G., et al. (2015a). In-operando high-speed tomography of lithium-ion batteries during thermal runaway. Nature communications, 6.

[Finegan et al., 2015b] Finegan, D. P., Tudisco, E., Scheel, M., Robinson, J. B., Taiwo, O. O., Eastwood, D. S., Lee, P. D., Di Michiel, M., Bay, B., Hall, S. A., et al. (2015b). Quantifying bulk electrode strain and material displacement within lithium batteries via high-speed operando tomography and digital volume correlation. Advanced Science.

[Fitzgerald, 2000] Fitzgerald, R. (2000). Phase-sensitive x-ray imaging. Phys. Today, 53(7):23–26.

[Fushiki et al., 2009] Fushiki, H., Kanoh-Azuma, T., Katoh, M., Kawabata, K., Jiang, J., Tsuchiya, N., Satow, A., Tamai, Y., and Hayakawa, Y. (2009). Quantification of mouse pulmonary cancer models by microcomputed tomography imaging. Cancer science, 100(8):1544–1549.

[Goetz et al., 1979] Goetz, K., Kalashnikov, M., Mikhaĭlov, Y. A., Sklizkov, G. V., Fedotov, S., Foerster, E., and Zaumseil, P. (1979). Measurements of the parameters of shell targets for laser thermonuclear fusion using an x-ray schlieren method. Quantum Electronics, 9(5):607–610.

[Grewar and Bryant, nd] Grewar, I. and Bryant, K. (n.d.). Advances in x-ray tube technology. http://www.nordson.com/-/media/Files/Nordson/dage/Products/X-ray-Technical-Papers-and-Articles/X-ray-

Technology/advances-in-xray-tube-technology.pdf?la=en. Accessed: 2017-01-18.

[Groso et al., 2006a] Groso, A., Abela, R., and Stampanoni, M. (2006a). Implementation of a fast method for high resolution phase contrast tomography. Optics express, 14(18):8103–8110.

[Groso et al., 2006b] Groso, A., Stampanoni, M., Abela, R., Schneider, P., Linga, S., and Müller, R. (2006b). Phase contrast tomography: an alternative approach. Applied physics letters, 88(21):214104.

[Guizar-Sicairos et al., 2015] Guizar-Sicairos, M., Boon, J. J., Mader, K., Diaz, A., Menzel, A., and Bunk, O. (2015). Quantitative interior x-ray nanotomography by a hybrid imaging technique. Optica, 2(3):259–266.

[Gureyev and Wilkins, 1998] Gureyev, T. and Wilkins, S. (1998). On x-ray phase imaging with a point source. JOSA A, 15(3):579–585.

[Gureyev et al., 2004] Gureyev, T. E., Davis, T. J., Pogany, A., Mayo, S. C., and Wilkins, S. W. (2004). Optical phase retrieval by use of first born-and rytov-type approximations. Applied optics, 43(12):2418–2430.

[Gureyev et al., 2008] Gureyev, T. E., Nesterets, Y. I., Stevenson, A. W., Miller, P. R., Pogany, A., and Wilkins, S. W. (2008). Some simple rules for contrast, signal-to-noise and resolution in in-line x-ray phase-contrast imaging. Optics express, 16(5):3223–3241.

[Hahn, 2014] Hahn, D. (2014). Statistical Iterative Reconstruction for X-ray Phase-Contrast Computed Tomography. PhD thesis, Technische Universität München.

[Haines et al., 2009] Haines, B. B., Bettano, K. A., Chenard, M., Sevilla, R. S., Ware, C., Angagaw, M. H., Winkelmann, C. T., Tong, C., Reilly, J. F., Sur, C., et al. (2009). A quantitative volumetric micro-computed tomography method to analyze lung tumors in genetically engineered mouse models. Neoplasia, 11(1):39–47.

[Hallbauer and Joughin, 1972] Hallbauer, D. and Joughin, N. (1972). Investigation Into the Distribution, Size and Shape of Gold Particles in Some Witwatersrand Reefs and Their Effects on Sampling Procedures. Chamber of Mines of South Africa.

[Halmshaw, 2012] Halmshaw, R. (2012). Industrial radiology: theory and practice, volume 1. Springer Science & Business Media.

[Henke et al., 1993] Henke, B. L., Gullikson, E. M., and Davis, J. C. (1993). X-ray interactions: photoabsorption, scattering, transmission, and reflection at e= 50-30,000 ev, z= 1-92. Atomic data and nuclear data tables, 54(2):181–342.

[Hounsfield, 1973] Hounsfield, G. N. (1973). Computerized transverse axial scanning (tomography): Part 1. description of system. The British journal of radiology, 46(552):1016–1022.

[Hsia et al., 2010] Hsia, C. C., Hyde, D. M., Ochs, M., and Weibel, E. R. (2010). An official research policy statement of the american thoracic society/european respiratory society: standards for quantitative assessment of lung structure. American journal of respiratory and critical care medicine, 181(4):394–418.

[Hsieh, 2009] Hsieh, J. (2009). Computed tomography: principles, design, artifacts, and recent advances. SPIE Bellingham, WA.

[Hutchinson, 2007] Hutchinson, M. (2007). A brief atlas of the human body. Pearson Education.

[Ishisaka et al., 2000] Ishisaka, A., Ohara, H., and Honda, C. (2000). A new method of analyzing edge effect in phase contrast imaging with incoherent x-rays. Optical Review, 7(6):566–572.

[Jacks et al., 1994] Jacks, T., Remington, L., Williams, B. O., Schmitt, E. M., Halachmi, S., Bronson, R. T., and Weinberg, R. A. (1994). Tumor spectrum analysis in p53-mutant mice. Current biology, 4(1):1–7.

[Jackson et al., 2001] Jackson, E. L., Willis, N., Mercer, K., Bronson, R. T., Crowley, D., Montoya, R., Jacks, T., and Tuveson, D. A. (2001). Analysis of lung tumor initiation and progression using conditional expression of oncogenic k-ras. Genes & development, 15(24):3243–3248.

[Jacoby, 2013] Jacoby, M. (2013). Assessing the safety of lithium-ion batteries. Chem. Eng. News, 91:33–37.

[Janošević et al., 2007] Janošević, D., Uzelac, B., Stojičić, D., and Budimir, S. (2007). Developmental anatomy of cotyledons and leaves in has mutant of arabidopsis thaliana. Protoplasma, 231(1-2):7–13.

[Jemal et al., 2011] Jemal, A., Bray, F., Center, M. M., Ferlay, J., Ward, E., and Forman, D. (2011). Global cancer statistics. CA: a cancer journal for clinicians, 61(2):69–90.

[Johnson et al., 2007] Johnson, T. R., Krauss, B., Sedlmair, M., Grasruck, M., Bruder, H., Morhard, D., Fink, C., Weckbach, S., Lenhard, M., Schmidt, B., et al. (2007). Material differentiation by dual energy ct: initial experience. European radiology, 17(6):1510–1517.

[Kak and Slaney, 1988] Kak, A. C. and Slaney, M. (1988). Principles of computerized tomographic imaging. IEEE press.

[Karçaaltincaba and Aktas, 2011] Karçaaltincaba, M. and Aktas, A. (2011). Dual-energy ct revisited with multidetector ct: review of principles and clinical applications. Diagnostic and Interventional Radiology, 17(3):181.

[Kardjilov, 2003] Kardjilov, N. (2003). Further developments and applications of radiography and tomography with thermal and cold neutrons. PhD thesis, Technische Universität München.

[Kasinski and Slack, 2012] Kasinski, A. L. and Slack, F. J. (2012). mirna-34 prevents cancer initiation and progression in a therapeutically resistant k-ras and p53-induced mouse model of lung adenocarcinoma. Cancer research, 72(21):5576–5587.

[Kastner et al., 2006] Kastner, J., Heim, D., Salaberger, D., Sauerwein, C., and Simon, M. (2006). Advanced applications of computed tomography by combination of different methods. In Proceedings of the European conference on nondestructive testing, Berlin, Germany.

[Kastner et al., 2012a] Kastner, J., Plank, B., Kottler, C., and Revol, V. (2012a). Comparison of phase contrast x-ray computed tomography methods for non-destructive testing of materials. In Conference Proceedings of the world conference on non-destructive testing.

[Kastner et al., 2012b] Kastner, J., Plank, B., and Salaberger, D. (2012b). High resolution x-ray computed tomography of fibre-and particle-filled polymers. In 18th World Conference on Nondestructive Testing, Durban, South Africa, pages 16–20.

[Kelly-Spratt et al., 2008] Kelly-Spratt, K. S., Kasarda, A. E., Igra, M., and Kemp, C. J. (2008). A mouse model repository for cancer biomarker discovery. J. Proteome Res, 7(8):3613–3618.

[Kia, 1993] Kia, H. G. (1993). Sheet molding compounds: science and technology. Hanser Verlag.

[Kirsch et al., 2010] Kirsch, D. G., Grimm, J., Guimaraes, A. R., Wojtkiewicz, G. R., Perez, B. A., Santiago, P. M., Anthony, N. K., Forbes, T., Doppke, K., Weissleder, R., et al. (2010). Imaging primary lung cancers in mice to study radiation biology. International Journal of Radiation Oncology* Biology* Physics, 76(4):973–977.

[Koch et al., 1998] Koch, A., Raven, C., Spanne, P., and Snigirev, A. (1998). X-ray imaging with submicrometer resolution employing transparent luminescent screens. JOSA A, 15(7):1940–1951.

[Koglin et al., 2010] Koglin, N., Frimmel, H. E., Minter, W. L., and Brätz, H. (2010). Trace-element characteristics of different pyrite types in mesoarchaean to palaeoproterozoic placer deposits. Mineralium Deposita, 45(3):259–280.

[Krieger, 2013] Krieger, H. (2013). Strahlungsquellen für Technik und Medizin, volume 2. Springer.

[Krissak et al., 2013] Krissak, R., Elgert, M., et al. (2013). Gold as a potential contrast agent for dual-energy ct. Advances in Molecular Imaging, 2013.

[Krüger, 2011] Krüger, S. (2011). Optimization of waveguide optics for lensless x-ray imaging, volume 2. Universitätsverlag Göttingen.

[Kruth et al., 2011] Kruth, J. P., Bartscher, M., Carmignato, S., Schmitt, R., De Chiffre, L., and Weckenmann, A. (2011). Computed tomography for dimensional metrology. CIRP Annals-Manufacturing Technology, 60(2):821–842.

[Kutsuzawa, 2002] Kutsuzawa, H. (2002). Penetrating type x-ray tube and manufacturing method thereof. US Patent 6,487,272.

[Langer et al., 2008] Langer, M., Cloetens, P., Guigay, J.-P., and Peyrin, F. (2008). Quantitative comparison of direct phase retrieval algorithms in in-line phase tomography. Medical physics, 35(10):4556–4566.

[Le et al., 2008] Le, T.-H., Dumont, P., Orgéas, L., Favier, D., Salvo, L., and Boller, E. (2008). X-ray phase contrast microtomography for the analysis of the fibrous microstructure of smc composites. Composites Part A: Applied Science and Manufacturing, 39(1):91–103.

[Lee et al., 2012] Lee, K. J., Dekkers, B. J., Steinbrecher, T., Walsh, C. T., Bacic, A., Bentsink, L., Leubner-Metzger, G., and Knox, J. P. (2012). Distinct cell wall architectures in seed endosperms in representatives of the brassicaceae and solanaceae. Plant physiology, 160(3):1551–1566.

[Liu et al., 2010] Liu, X., Zhao, J., Sun, J., Gu, X., Xiao, T., Liu, P., and Xu, L. X. (2010). Lung cancer and angiogenesis imaging using synchrotron radiation. Physics in medicine and biology, 55(8):2399.

[Lucy, 1974] Lucy, L. B. (1974). An iterative technique for the rectification of observed distributions. The astronomical journal, 79:745.

[MacIntosh et al., 2006] MacIntosh, B. R., Gardiner, P. F., and McComas, A. J. (2006). Skeletal muscle: form and function. Human Kinetics.

[Mayo et al., 2003] Mayo, S., Davis, T., Gureyev, T., Miller, P., Paganin, D., Pogany, A., Stevenson, A., and Wilkins, S. (2003). X-ray phase-contrast microscopy and microtomography. Optics Express, 11(19):2289–2302.

[Mayo et al., 2012] Mayo, S. C., Stevenson, A. W., and Wilkins, S. W. (2012). In-line phase-contrast x-ray imaging and tomography for materials science. Materials, 5(5):937–965.

[Meinke, 1992] Meinke, D. W. (1992). A homoeotic mutant of arabidopsis thaliana with leafy cotyledons. Science, 258(5088):1647–1650.

[Meinke et al., 1994] Meinke, D. W., Franzmann, L. H., Nickle, T. C., and Yeung, E. C. (1994). Leafy cotyledon mutants of arabidopsis. The Plant Cell, 6(8):1049–1064.

[Mertens et al., 2014] Mertens, J., Williams, J., and Chawla, N. (2014). Development of a lab-scale, high-resolution, tube-generated x-ray computed-tomography system for three-dimensional (3d) materials characterization. Materials Characterization, 92:36–48.

[Metscher, 2009a] Metscher, B. D. (2009a). Microct for comparative morphology: simple staining methods allow high-contrast 3d imaging of diverse non-mineralized animal tissues. BMC physiology, 9(1):1.

[Metscher, 2009b] Metscher, B. D. (2009b). Microct for developmental biology: A versatile tool for high-contrast 3d imaging at histological resolutions. Developmental Dynamics, 238(3):632–640.

[Momose, 2005] Momose, A. (2005). Recent advances in x-ray phase imaging. Japanese Journal of Applied Physics, 44(9R):6355.

[Momose et al., 2003] Momose, A., Kawamoto, S., Koyama, I., Hamaishi, Y., Takai, K., and Suzuki, Y. (2003). Demonstration of x-ray talbot interferometry. Japanese journal of applied physics, 42(7B):L866.

[Moosmann et al., 2013] Moosmann, J., Ershov, A., Altapova, V., Baumbach, T., Prasad, M. S., LaBonne, C., Xiao, X., Kashef, J., and Hofmann, R. (2013). X-ray phase-contrast in vivo microtomography probes new aspects of xenopus gastrulation. Nature, 497(7449):374–377.

[Müller et al., 2006] Müller, K., Tintelnot, S., and Leubner-Metzger, G. (2006). Endosperm-limited brassicaceae seed germination: abscisic acid inhibits embryo-induced endosperm weakening of lepidium sativum (cress) and endosperm rupture of cress and arabidopsis thaliana. Plant and Cell Physiology, 47(7):864–877.

[Muller et al., 1994] Muller, R., Hildebrand, T., and Ruegsegger, P. (1994). Non-invasive bone biopsy: a new method to analyse and display the three-dimensional structure of trabecular bone. Physics in medicine and biology, 39(1):145.

[Nesterets et al., 2005] Nesterets, Y. I., Wilkins, S., Gureyev, T., Pogany, A., and Stevenson, A. (2005). On the optimization of experimental parameters for x-ray in-line phase-contrast imaging. Review of scientific instruments, 76(9):093706.

[Norton, 1896] Norton, C. L. (1896). The x-rays in medicine and surgery. Science, 3(72):730–731.

[Nugent et al., 1996] Nugent, K., Gureyev, T., Cookson, D., Paganin, D., and Barnea, Z. (1996). Quantitative phase imaging using hard x rays. Physical review letters, 77(14):2961.

[Nwaila et al., 2013] Nwaila, G., Becker, M., Ghorbani, Y., Petersen, J., Reid, D., Bam, L., de Beer, F., and Franzidis, J. (2013). A geometallurgical study of the witwatersrand gold ore at carletonville, south africa. In The Second AusIMM International Geometallurgy Conference. AusIMM, Brisbane, Australia, pages 75–84.

[Opferman et al., 2003] Opferman, J. T., Letai, A., Beard, C., Sorcinelli, M. D., Ong, C. C., and Korsmeyer, S. J. (2003). Development and maintenance of b and t lymphocytes requires antiapoptotic mcl-1. Nature, 426(6967):671–676.

[Orgéas and Dumont, 2012] Orgéas, L. and Dumont, P. J. (2012). Sheet molding compounds. Wiley Encyclopedia of Composites.

[Pacheco et al., 2015] Pacheco, M. L. F., Galante, D., Rodrigues, F., Leme, J. d. M., Bidola, P., Hagadorn, W., Stockmar, M., Herzen, J., Rudnitzki, I. D., Pfeiffer, F., et al. (2015). Insights into the skeletonization, lifestyle, and affinity of the unusual ediacaran fossil corumbella. PloS one, 10(3):e0114219.

[Paganin, 2006] Paganin, D. (2006). Coherent X-ray optics. Oxford University Press.

[Paganin et al., 2002] Paganin, D., Mayo, S., Gureyev, T. E., Miller, P. R., and Wilkins, S. W. (2002). Simultaneous phase and amplitude extraction from a single defocused image of a homogeneous object. Journal of microscopy, 206(1):33–40.

[Palmer et al., 2010] Palmer, J., Savage, L., Ghita, O., and Evans, K. (2010). Sheet moulding compound (smc) from carbon fibre recyclate. Composites Part A: Applied Science and Manufacturing, 41(9):1232–1237.

[Pavlov et al., 2004] Pavlov, K., Gureyev, T., Paganin, D., Nesterets, Y. I., Morgan, M., and Lewis, R. (2004). Linear systems with slowly varying transfer functions and their application to x-ray phase-contrast imaging. Journal of Physics D: Applied Physics, 37(19):2746.

[Penney et al., 2012] Penney, D., McNeil, A., Green, D. I., Bradley, R. S., Jepson, J. E., Withers, P. J., and Preziosi, R. F. (2012). Ancient ephemeroptera–collembola symbiosis fossilized in amber predicts contemporary phoretic associations. PloS one, 7(10):e47651.

[Peterzol et al., 2005] Peterzol, A., Olivo, A., Rigon, L., Pani, S., and Dreossi, D. (2005). The effects of the imaging system on the validity limits of the ray-optical approach to phase contrast imaging. Medical physics, 32(12):3617–3627.

[Pfeiffer et al., 2009] Pfeiffer, F., Bech, M., Bunk, O., Donath, T., Henrich, B., Kraft, P., and David, C. (2009). X-ray dark-field and phase-contrast imaging using a grating interferometer. Journal of Applied Physics, 105(10):102006.

[Pfeiffer et al., 2007] Pfeiffer, F., Bunk, O., David, C., Bech, M., Le Duc, G., Bravin, A., and Cloetens, P. (2007). High-resolution brain tumor visualization using three-dimensional x-ray phase contrast tomography. Physics in medicine and biology, 52(23):6923.

[Pfeiffer et al., 2006] Pfeiffer, F., Weitkamp, T., Bunk, O., and David, C. (2006). Phase retrieval and differential phase-contrast imaging with low-brilliance x-ray sources. Nature physics, 2(4):258–261.

[Pinard et al., 2010] Pinard, P. T., Demers, H., Salvat, F., and Gauvin, R. (2010). An api/gui for monte carlo simulation of epma spectra using penelope. Microscopy and Microanalysis, 16(S2):280–281.

[Pogany et al., 1997] Pogany, A., Gao, D., and Wilkins, S. (1997). Contrast and resolution in imaging with a microfocus x-ray source. Review of Scientific Instruments, 68(7):2774–2782.

[Primak et al., 2007] Primak, A. N., Fletcher, J. G., Vrtiska, T. J., Dzyubak, O. P., Lieske, J. C., Jackson, M. E., Williams, J. C., and McCollough, C. H. (2007). Noninvasive differentiation of uric acid versus non–uric acid kidney stones using dual-energy ct. Academic radiology, 14(12):1441–1447.

[Purschke, 2005] Purschke, M. (2005). Eine neue Generation röntgenempfindlicher Flächendetektoren. http://www.ndt.net/article/dgzfp05/v06.pdf. Accessed: 2017-01-18.

[Rasch et al., 2016] Rasch, L. J., Martin, K. J., Cooper, R. L., Metscher, B. D., Underwood, C. J., and Fraser, G. J. (2016). An ancient dental gene set governs development and continuous regeneration of teeth in sharks. Developmental biology.

[Ribi et al., 2008] Ribi, W., Senden, T. J., Sakellariou, A., Limaye, A., and Zhang, S. (2008). Imaging honey bee brain anatomy with micro-x-ray-computed tomography. Journal of neuroscience methods, 171(1):93–97.

[Richardson, 1972] Richardson, W. H. (1972). Bayesian-based iterative method of image restoration. JOSA, 62(1):55–59.

[Ritman, 2004] Ritman, E. L. (2004). Micro-computed tomography–current status and developments. Annual review of biomedical engineering, 6:185–208.

[Ritman, 2011] Ritman, E. L. (2011). Current status of developments and applications of micro-ct. Annual review of biomedical engineering, 13:531–552.

[Röntgen, 1895] Röntgen, C. (1895). Über eine neue art von strahlen. Sitzung, 30:132–141.

[Rueckel et al., 2014] Rueckel, J., Stockmar, M., Pfeiffer, F., and Herzen, J. (2014). Spatial resolution characterization of a x-ray microct system. Applied Radiation and Isotopes, 94:230–234.

[Rügsegger et al., 1996] Rügsegger, P., Koller, B., and Müller, R. (1996). A microtomographic system for the nondestructive evaluation of bone architecture. Calcified tissue international, 58(1):24–29.

[Saleh, 1991] Saleh, B. (1991). Mc teich fundamentals of photonics.

[Samei et al., 1998] Samei, E., Flynn, M. J., and Reimann, D. A. (1998). A method for measuring the presampled mtf of digital radiographic systems using an edge test device. Medical physics, 25(1):102–113.

[Schiaffino and Reggiani, 2011] Schiaffino, S. and Reggiani, C. (2011). Fiber types in mammalian skeletal muscles. Physiological reviews, 91(4):1447–1531.

[Schwarz, 2014] Schwarz, J. (2014). Dual-energy micro-ct. Master's thesis, Technische Universität München.

[Senyshyn et al., 2015] Senyshyn, A., Mühlbauer, M., Dolotko, O., Hofmann, M., and Ehrenberg, H. (2015). Homogeneity of lithium distribution in cylinder-type li-ion batteries. Scientific reports, 5.

[Shearer et al., 2014] Shearer, T., Rawson, S., Castro, S. J., Balint, R., Bradley, R. S., Lowe, T., Vila-Comamala, J., Lee, P. D., and Cartmell, S. H. (2014). X-ray computed tomography of the anterior cruciate ligament and patellar tendon. Muscles, ligaments and tendons journal, 4(2):238.

[Siegel et al., 2013] Siegel, R., Naishadham, D., and Jemal, A. (2013). Cancer statistics, 2013. CA: a cancer journal for clinicians, 63(1):11–30.

[Singhal et al., 2013] Singhal, A., Grande, J. C., and Zhou, Y. (2013). Micro/nano-ct for visualization of internal structures. Microscopy Today, 21(02):16–22.

[Sotgia et al., 2011] Sotgia, F., Martinez-Outschoorn, U. E., and Lisanti, M. P. (2011). Mitochondrial oxidative stress drives tumor progression and metastasis: should we use antioxidants as a key component of cancer treatment and prevention? BMC medicine, 9(1):1.

[Stahr et al., 2016] Stahr, C. S., Samarage, C. R., Donnelley, M., Farrow, N., Morgan, K. S., Zosky, G., Boucher, R. C., Siu, K. K., Mall, M. A., Parsons, D. W., et al. (2016). Quantification of heterogeneity in lung disease with image-based pulmonary function testing. Scientific Reports, 6.

[Stampanoni et al., 2002] Stampanoni, M., Borchert, G., Wyss, P., Abela, R., Patterson, B., Hunt, S., Vermeulen, D., and Rüegsegger, P. (2002). High resolution x-ray detector for synchrotron-based microtomography. Nuclear Instruments and Methods in Physics Research Section A: Accelerators, Spectrometers, Detectors and Associated Equipment, 491(1):291–301.

[Stille et al., 2013] Stille, M., Smith, E. J., Crum, W. R., and Modo, M. (2013). 3d reconstruction of 2d fluorescence histology images and registration with in vivo mr images: Application in a rodent stroke model. Journal of neuroscience methods, 219(1):27–40.

[Tapfer et al., 2011] Tapfer, A., Bech, M., Pauwels, B., Liu, X., Bruyndonckx, P., Sasov, A., Kenntner, J., Mohr, J., Walter, M., Schulz, J., et al. (2011). Development of a prototype gantry system for preclinical x-ray phase-contrast computed tomography. Medical physics, 38(11):5910–5915.

[Tuohimaa et al., 2007] Tuohimaa, T., Otendal, M., and Hertz, H. M. (2007). Phase-contrast x-ray imaging with a liquid-metal-jet-anode microfocus source. Applied Physics Letters, 91(7):074104.

[Turner et al., 2004] Turner, L., Dhal, B., Hayes, J., Mancuso, A., Nugent, K., Paterson, D., Scholten, R., Tran, C., and Peele, A. (2004). X-ray phase imaging: Demonstration of extended conditions with homogeneous objects. Optics express, 12(13):2960–2965.

[Van Metter et al., 2000] Van Metter, R., Beutel, J., and Kundel, H. (2000). Handbook of medical imaging: Physics and psychophysics. SPIE.

[Vasilescu et al., 2012] Vasilescu, D. M., Knudsen, L., Ochs, M., Weibel, E. R., and Hoffman, E. A. (2012). Optimized murine lung preparation for detailed structural evaluation via micro-computed tomography. Journal of Applied Physiology, 112(1):159–166.

[Verboven et al., 2013] Verboven, P., Herremans, E., Borisjuk, L., Helfen, L., Ho, Q. T., Tschiersch, H., Fuchs, J., Nicolaï, B. M., and Rolletschek, H. (2013). Void space inside the developing seed of brassica napus and the modelling of its function. New Phytologist, 199(4):936–947.

[Weitkamp et al., 2005] Weitkamp, T., Diaz, A., David, C., Pfeiffer, F., Stampanoni, M., Cloetens, P., and Ziegler, E. (2005). X-ray phase imaging with a grating interferometer. Optics express, 13(16):6296–6304.

[Weitkamp et al., 2011] Weitkamp, T., Haas, D., Wegrzynek, D., and Rack, A. (2011). Ankaphase: software for single-distance phase retrieval from inline x-ray phase-contrast radiographs. Journal of synchrotron radiation, 18(4):617–629.

[Weninger et al., 2006] Weninger, W. J., Geyer, S. H., Mohun, T. J., Rasskin-Gutman, D., Matsui, T., Ribeiro, I., Costa, L. d. F., Izpisua-Belmonte, J. C., and Müller, G. B. (2006). High-resolution episcopic microscopy: a rapid technique for high detailed 3d analysis of gene activity in the context of tissue architecture and morphology. Anatomy and embryology, 211(3):213–221.

[Wernersson et al., 2013] Wernersson, E. L., Boone, M. N., Van den Bulcke, J., Van Hoorebeke, L., and Hendriks, C. L. L. (2013). Postprocessing method for reducing phase effects in reconstructed microcomputed-tomography data. JOSA A, 30(3):455–461.

[Westneat et al., 2003] Westneat, M. W., Betz, O., Blob, R. W., Fezzaa, K., Cooper, W. J., and Lee, W.-K. (2003). Tracheal respiration in insects visualized with synchrotron x-ray imaging. Science, 299(5606):558–560.

[Whitacre and Czabaj, 2015] Whitacre, W. W. and Czabaj, M. W. (2015). Automated 3d digital reconstruction of fiber reinforced polymer composites. American Institute of Aeronautics and Astronautics SciTech, pages 1–18.

[Wilkins et al., 1996] Wilkins, S., Gureyev, T., Gao, D., Pogany, A., Stevenson, A., et al. (1996). Phase-contrast imaging using polychromatic hard x-rays. Nature, 384(6607):335–338.

[Willmott, 2011] Willmott, P. (2011). An introduction to synchrotron radiation: Techniques and applications. John Wiley & Sons.

[Wu and Liu, 2003] Wu, X. and Liu, H. (2003). Clinical implementation of x-ray phase-contrast imaging: Theoretical foundations and design considerations. Medical physics, 30(8):2169–2179.

[Zabler et al., 2005] Zabler, S., Cloetens, P., Guigay, J.-P., Baruchel, J., and Schlenker, M. (2005). Optimization of phase contrast imaging using hard x rays. Review of Scientific Instruments, 76(7):073705.

[Zanette et al., 2014] Zanette, I., Zhou, T., Burvall, A., Lundström, U., Larsson, D. H., Zdora, M., Thibault, P., Pfeiffer, F., and Hertz, H. M. (2014). Speckle-based x-ray phase-contrast and dark-field imaging with a laboratory source. Physical review letters, 112(25):253903.

[Zhou et al., 2016] Zhou, R., Zhou, X., Li, X., Cai, Y., and Liu, F. (2016). Study of the microfocus x-ray tube based on a point-like target used for micro-computed tomography. PloS one, 11(6):e0156224.

[Zoofan et al., 2004] Zoofan, B., Kim, J.-Y., Rokhlin, S., and Frankel, G. (2004). Phase-contrast x-ray imaging for nondestructive evaluation of materials. In QUANTITATIVE NONDESTRUCTIVE EVALUATION, volume 700, pages 546–553. AIP Publishing.

[Zoofan et al., 2006] Zoofan, B., Kim, J.-Y., Rokhlin, S., and Frankel, G. (2006). Phase-contrast x-ray imaging for nondestructive evaluation of materials. Journal of applied physics, 100(1):014502.

Appendix

A.1 Optimization of the spatial resolution through deconvolution

The spatial resolution of any imaging system relies on the performance of each interacting instrument. At the setups presented in this work, it is influenced by the magnification of the source spot on the detector and also on the response of latter. These contributions of the imaging components are manifested by a "blurring" in the acquired images and are described by the point spread function of the system. A common approach of solution to this effect by optimizing the spatial resolution is the **deconvolution**. It aims to recover a true object *O* out of a blurred image

$$I = O * PSF + N. \tag{8.1}$$

The recorded image I represents a convolution $(*)$ of the object by the overall PSF of the imaging system, to which the noise N emanating from the detector is added. Use has been made of the Richardson-Lucy algorithm, which is based on the methods proposed by [Richardson, 1972, Lucy, 1974]. This algorithm was derived and implemented in previous works (e.g., [Hahn, 2014, De Marco, 2015]). Fundamentally, the true object is iteratively achieved as follows

$$O^{(i+1)} = O^{(i)} \cdot \left(\overline{PSF} * \frac{I}{PSF * O^{(i)}} \right). \tag{8.2}$$

The iteration number is indicated by (i) and $\overline{PSF}$ stands for a flipped PSF. In the present context of microscopy and phase-contrast imaging, an ideal point-like source could procure partial coherence and enable phase contrast. In section 4.3, the relatively large source size was shown to limit the occurrence of the phase contrast, which is observed as edge enhancement. Therefore, the deconvolution has been applied using Eq. 8.2 and starting with an initial object $O^{(0)} = I$. Note that the deconvolution is suggested to enhance the image quality due to the weak phase contrast that can provide the imaging system.

A.2 Geometric optimization of the spatial resolution

The variation of the spatial resolution as function of some parameters of a laboratory setup such as the source size, the geometric magnification and the optical magnification if available are demonstrated in this section.

Conventional cone-beam system (e.g., v|tome|x 240)

From the description of the spatial resolution of an imaging system in Eq. 2.1 using the standard deviation σ, i.e,

$$\sigma_{\text{sys}} = \sqrt{(M-1)^2 M^{-2} {\sigma_{\text{src}}}^2 + M^{-2} {\sigma_{\text{det}}}^2}, \tag{8.3}$$

where σ_{src} and detector σ_{det} represent the standard deviations of the source and the detector, respectively. Equation 8.3 can be reformulated as

$$\text{FWHM}_{\text{sys}} = ((M-1)^2 M^{-2} {\text{FWHM}_{\text{src}}}^2 + M^{-2} {\text{FWHM}_{\text{det}}}^2)^{\frac{1}{2}}, \tag{8.4}$$

by means of the full-width at half maximum of a Gaussian FWHM = $2\sqrt{2\ln 2}\sigma$. With consideration of the relations between the spatial resolution of the system r_{sys}, the source spot of the X-ray source S, the detector pixel size ps and the FWHM established as

$$\text{FWHM}_{\text{sys}} = r_{\text{sys}}, \qquad \text{FWHM}_{\text{src}} = S, \qquad \text{FWHM}_{\text{det}} = ps.$$

Eq. 8.4 is accordingly rewritten as follows [Feser et al., 2008]:

$$\begin{aligned} r_{\text{sys}} &= \frac{\sqrt{(M-1)^2 S^2 + ps^2}}{M} \\ &= \left(\left(1 - \frac{1}{M}\right)^2 S^2 + \frac{ps^2}{M^2}\right)^{\frac{1}{2}}. \end{aligned} \tag{8.5}$$

Provided that the detector pixel size and the source spot size of a system are known for a specific voltage and current of the X-ray tube, the spatial resolution would vary as function of the geometric magnification $r_{\text{sys}}(M)$. From Eq. 8.5, the following agreements fulfil:

$$\lim_{M \to 1} r_{\text{sys}}(M) = ps, \qquad \lim_{M \to \infty} r_{\text{sys}}(M) = S.$$

The function r_{sys} reaches its minimum when its first derivative equals zero ($r'_{\text{sys}} = 0$), which is satisfied at

$$M_{min} = \left(\frac{ps}{S}\right)^2 + 1. \tag{8.6}$$

As plotted in Fig. 8.1(a) for a cone-beam system such as v|tome|x, the spatial resolution decreases from a value equal to ps at a geometric magnification $M = 1$ to the size of the source spot S, where $M = \frac{ps^2 - S^2}{2S^2}$ and reaches the optimal spatial resolution available in the system

$$r_{sys} = \frac{\left(ps^2 + \frac{ps^4}{S^2}\right)^{\frac{1}{2}}}{\frac{ps^2}{S^2} + 1}, \tag{8.7}$$

at M_{min} also known as the optimal geometric magnification. Above this optimal magnification, the resolution increases towards the source spot size S at very high magnifications. The graph of this figure is plotted considering the 200 µm pixel size of the detector and an arbitrary source spot size of 15 µm.

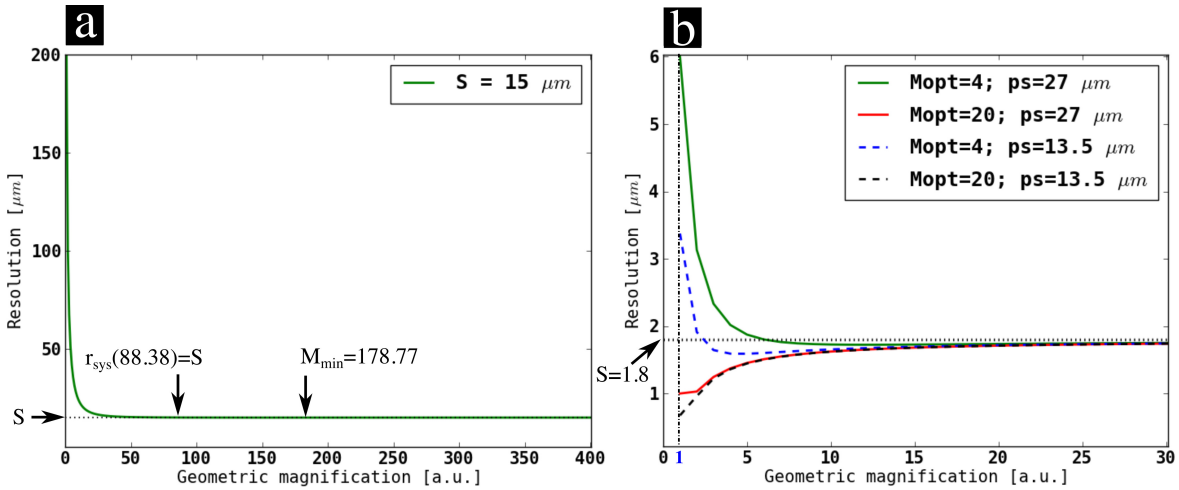

Figure 8.1: Analysis of the spatial resolution r_{sys} as function of the geometric magnification M. (a) Curve progression of this function using the example of v|tome|x, supplied with a detector pixel size of 200 µm and admitting a source size S =15 µm. (b) Shape of this function in a system equipped with a lens-coupled detector (ZEISS Xradia 500 Versa), according to the optical magnification M_{opt} and the pixel binning. The dashed curves represent an unbinned detector pixels and the solid lines a 2-fold binned pixels.

Cone-beam system with a lens-coupled detector (e.g., ZEISS Xradia 500 Versa)

Within a system furnished with a lens-coupled detector, the virtual detector pixel size on the scintillator is given by $\frac{ps}{M_{\text{opt}}}$, where M_{opt} is the optical magnification of the objective. Consequently, Eq. 8.5 is reformulated as

$$r_{\text{sys}} = \left(\left(1 - \frac{1}{M}\right)^2 S^2 + \frac{ps^2}{M_{\text{opt}}^2 M^2}\right)^{\frac{1}{2}}, \tag{8.8}$$

and the following relationships hold true:

$$\lim_{M\to 1} r_{\text{sys}}(M) = \frac{ps}{M_{\text{opt}}}, \qquad \lim_{M\to\infty} r_{\text{sys}}(M) = S, \qquad M_{min} = \left(\frac{ps}{M_{\text{opt}} S}\right)^2 + 1.$$

The function $r_{sys}(M)$ is plotted correspondingly in Fig. 8.1(b) for the 4× and 20× optical magnifications by considering a binned (solid curves) and an unbinned (dashed curves) detector pixels. A source spot size of 1.8 µm has been taken into account. From this illustration, the conditions for obtaining optimal spatial resolution in this system are determined. Compared to Fig. 8.1(a), it is demonstrated in Fig. 8.1(b) that a spatial resolution well below the source spot size can be attained in a cone-beam system using a lens-coupled detector assembly.

Publications and scientific presentations

First-authored publications (peer-reviewed)

[Bidola et al., 2015a] Bidola, P., Stockmar, M., Achterhold, K., Pfeiffer, F., Pacheco, M. L., Soriano, C., Beckmann, F., and Herzen, J. (2015a). Absorption and phase-contrast x-ray imaging in paleontology using laboratory and synchrotron sources. *Microscopy and Microanalysis*, 21(05):1288–1295.

[Bidola et al., 2015b] Bidola, P. M., Zanette, I., Achterhold, K., Holzner, C., and Pfeiffer, F. (2015b). Optimization of propagation-based phase-contrast imaging at a laboratory setup. *Optics express*, 23(23):30000–30013.

[Bidola et al., 2016] Bidola, P. M., Morgan, K., Willner, M., Fehringer, A., Allner, S., Prade, F., Pfeiffer, F., and Achterhold, K. (2016). Application of sensitive, high-resolution imaging at a commercial lab-based X-ray micro-CT system using propagation-based phase retrieval. *Journal of Microscopy*. Accepted.

[Bidola et al.] Bidola, P. M., e Silva, J., M., Achterhold, K., Munkhbaatar, E., Jost, P., Meinhardt, A.-L., Taphorn, K., Zdora, M.-C., Pfeiffer, F., and Herzen, J. A step towards valid detection and quantification of lung cancer volume in experimental mice with contrast agent-based X-ray microtomography. *Nature Scientific Report*. Resubmitted.

Co-authored publications (peer-reviewed)

[Pacheco et al., 2015] Pacheco, M. L. F., Galante, D., Rodrigues, F., Leme, J. d. M., Bidola, P., Hagadorn, W., Stockmar, M., Herzen, J., Rudnitzki, I. D., Pfeiffer, F., et al. (2015). Insights into the skeletonization, lifestyle, and affinity of the unusual ediacaran fossil corumbella. *PloS one*, 10(3):e0114219.

[Müller et al.] Müller, M., Oliveira, I., Allner, S., Ferstl, S., Bidola, P., Mechlem, K., Fehringer, A., Hehn, L., Dierolf, M., Achterhold, K., Gleich, B., Hammel, J., Jahn, H., Tuohima, T., Takman, P., Hansson, B., Mayer, G., and Pfeiffer, F. X-ray nanoCT for visualization of muscles in velvet worm legs. Submitted to Nature Photonics.

Conference proceedings

[Bidola et al., 2014] Bidola, P., Pacheco, M. L., Stockmar, M. K., Achterhold, K., Pfeiffer, F., Beckmann, F., Beckmann, F., Tafforeau, P. & Herzen, J. (2014, September). Applied x-ray

computed tomography with high resolution in paleontology using laboratory and synchrotron sources. In SPIE Optical Engineering+Applications (pp. 92120X-92120X). International Society for Optics and Photonics.

Oral presentations

Title: Applied x-ray computed tomography with high resolution in paleontology using laboratory and synchrotron sources. *SPIE Optical Engineering+Applications, San Diego, California, USA, August 2014.*

Title: Biomedical applications of X-ray phase-contrast imaging. *XXXVII Brazilian Meeting on Nuclear Physics, Maresias-Brasil, September 2014.*

Title: X-ray imaging applications in paleontology, *Workshop on advanced research in paleontology using modern non-destructive techniques (Paleometry), Sorocaba, Brazil, September 2014.*

Poster presentations

Title: Soil Material Investigation using High-Resolution Micro-CT setups, *Industrial CT scanning workshop, Garching, Germany, October 2013.*

Title: Optimization of In-line Phase-Contrast Imaging at an X-Ray Microscope, *International Conference on X-ray Microscopy (XRM), Melbourne, Australia, October 2014.*

Title: Phase-Contrast imaging applied on biological and material samples using a commercial X-Ray system, *International Conference on Tomography of Materials and Structures (ICTMS), Quebec, Canada, June-July 2015.*

Title: Propagation-based phase retrieval: Applications at a lab-based microCT system, *International Conference on X-ray Microscopy (XRM), Oxford, UK, August 2015.*

Acknowledgements

I am grateful for the support and help that have been provided to me in different forms by many persons. I would like to express great gratitude to

- my academic supervisors, Prof. Dr. Franz Pfeiffer and Dr. Klaus Achterhold. Franz, you have given me the opportunity to be part of a group, where I have grown scientifically and socially. In short, I have been procured an ideal scientific environment. I deeply appreciate your support without distinction, that enabled some close contact with scientists in the X-ray imaging community around the world. Without your expertise, finding special solution to special administrative issues, many things would not have been possible for me. Thank you sincerely for that. Thank you Klaus for supporting me throughout every aspect of this thesis work, being promptly available for discussion and help anytime I showed up unexpectedly at your office, in the lab or everywhere the opportunity for exchange was given.

- Dr. Julia Herzen. I benefited from your support since I joined the chair. Since then, you would always find time to answer my requests, support me in tense situations when I would not expect you. I would also like to thank you very much for your organisational role in managing few projects I was involved in.

- Dr. Irene Zanette for her support discussing a lot of topics at the beginning of this thesis. Irene, I really appreciated your quick reply and help on our publication. I would like to thank Dr. Juliana Martins e Silva, Dr. Kaye Morgan and Dr. Madleen Busse for being easily accessible and willing to work on some documents anytime I needed some help or advices. Many thanks to Jolanda Schwarz and Kirsten Taphorn. I would like to address my acknowledgements to Yash Sharma, Irina Petcu and Elisabeth Hamzi-Schmidt for the proofreading of this thesis.

- Mark Müller, Johannes Wolf, Sebastian Allner, Andreas Fehringer and Dr. Martin Dierolf, as I did not need any appointment to have your help and discuss a lot of experimental or programming issues. I thank all my colleagues without distinction who have rather become my friends through various socialisation activities: Lukas, Joni, [...]. I would express a great appreciation to my colleague, friend and brother Lorenz Birnbacher for being there for me as a special one since the first time we met on the campus of Garching.

- the examination committee of this thesis, the chairman Prof. Dr. Martin Zacharias and the second referee Prof. Dr. Jan Wilkins.

- Dr. DER Willner and Dr. Michael Epple for the fun and their suggestions that helped solve technical issues. I thank Ulrike and Dr. Dieter Renker for their kindness, and the pleasant events I could attend at their place.

- our collaborators at the “III. Medizinische Klinik, Klinikum rechts der Isar”, namely PD Dr. Philipp Jost, Dr. Enkhtsetseg Munkhbaatar, and Anna-Lena Meinhardt. I am thankful to Lunga Bam and Frikkie De Beer from the South African Nuclear Energy Corporation, NECSA. My appreciation goes also to Prof. Dr. Mirian Pacheco Forancelli, Dr. Christian Holzner, Dr. Martin Mühlbauer, Dr. Irina Heid and Hugo Jaillet.

- Nelly de Leiris for the professional management of all my requests. Merci pour ta patience et ta sérénité à résoudre les moindres soucis administratifs. J’en ai eu beaucoup, les doléances.

- Dr. Bughsin’ Djath (my mate) for her invaluable support, my family and friends who always encouraged me, especially Katrin and Maxime Chango. Many thanks to Gunther Hösl for his trust and assistance when I was the most in need of him. I thank my mother Afoua Dinikpirou for her all-time support during my entire curriculum.